Tectonophysics 760 (2019) 165–198

Contents lists available at ScienceDirect

Tectonophysics

journal homepage: www.elsevier.com/locate/tecto

Review

# Core formation, mantle differentiation and core-mantle interaction within Earth and the terrestrial planets

R.G. Trønnes[a,b,*], M.A. Baron[b,1], K.R. Eigenmann[b], M.G. Guren[b,2], B.H. Heyn[b], A. Løken[b,3], C.E. Mohn[b]

[a] Natural History Museum, University of Oslo, Norway
[b] Centre for Earth Evolution and Dynamics, University of Oslo, Norway

ARTICLE INFO

*Keywords:*
Planetary accretion
Core segregation
Basal magma ocean
Core-mantle exchange

ABSTRACT

The terrestrial planets accreted from a diverse suite of solar system materials ranging from strongly O-deficient materials similar to enstatite chondrites via ordinary chondrite materials to fully oxidised carbonaceous chondrite and cometary materials. Heliocentric zoning with increasingly oxidised planetesimals outwards through the protoplanetary disc is broadly reflected in core fraction and $FeO^{mantle}$ concentration, ranging from 68 wt% core and 0.5 wt% $FeO^{mantle}$ for Mercury to 18 wt% core and 24 wt% $FeO^{mantle}$ for Vesta. Mercury, Venus and Earth grew mostly from materials which were isotopically similar to enstatite chondrites, although Earth and Venus also received more oxidised material. The elevated (Mg + Fe)/Si ratio, compared to chondrites, in the bulk silicate fraction of the terrestrial planets, except for Mercury, may be related to a combination of nebular fractionation associated with forsterite condensation, concentration of olivine-rich chondrules near the mid-plane of the accretion disc and multi-cycle impact erosion of protocrusts. For the extremely reduced Mercury the silicate magma ocean (MO) and a core with 15 wt% Si might have equilibrated with a melt layer of FeS at the core-mantle boundary (CMB). Recent data from the MESSENGER mission combined with experimentally derived phase relations, support estimates of about 0.5 wt% FeO and 10 wt% S in the MO and the current mantle. Core segregation at very high temperatures for the largest planets, Venus and Earth, led to cores with high Si content, even at relatively high oxygen fugacities and $FeO^{mantle}$ contents, because increasing temperature shifts the equilibrium:

$$SiO_2^{MO} + 2Fe^{core} = 2FeO^{MO} + Si^{core}$$

towards the products (right side). The hot protocores of Venus and Earth might have started with about 5–7 wt% Si and 2–3 wt% O. Mars and Vesta segregated S-rich cores at high oxygen fugacity and low pressure.

Strong partitioning of Fe and Mg to melt and solids, respectively, caused neutrally buoyant bridgmanite (bm) to crystallise from the MO at 1700–1860 km depth (72–80 GPa), resulting in a separate basal magma ocean (BMO) within Earth, and probably also in Venus. Slow cooling of a thermally insulated BMO and core, accompanied by protracted crystallisation of bm and ferropericlase (fp), would facilitate core-BMO chemical exchange by reversing the equilibrium $SiO_2^{MO} + 2Fe^{core} = 2FeO^{MO} + Si^{core}$ towards the reactants. Transfer of silica crystals and a liquid $SiO_2$ component from the core to the BMO, and liquid FeO and $Fe_2O_3$ components from the BMO to the core, would increase the Si/Mg, Mg/Fe and bm/fp ratio of the resulting cumulates. Because the solidus temperature of peridotite is < 200–300 K above the present temperature of the outermost core, and the melting interval of late-stage BMO melt enriched in Al, Fe, Ca and Na would be lower than that of peridotite, the BMO might have persisted through the Hadean and possibly also the Archean. Low solid state diffusion rates, especially in bm, would have restricted the core-mantle interaction upon BMO solidification, but limited core-mantle interaction could possibly occur via partially molten ultra-low velocity zones. An outermost stagnant low-density and low-velocity core layer (E′-layer), with reduced Si and elevated O contents relative to the convecting core, appears to trace the core-BMO exchange. The E′-layer is compositionally gradational towards

* Corresponding author at: Centre for Earth Evolution and Dynamics and Natural History Museum, University of Oslo, Norway.
*E-mail address:* r.g.tronnes@nhm.uio.no (R.G. Trønnes).
[1] Now: Inst. Minéralogie, de Physique des Matériaux et de Cosmochimie, Sorbonne Université, Paris, France.
[2] Now: Njord Centre, Department of Geosciences, University of Oslo, Norway.
[3] Now: Jotun Performance Coatings, Jotun A/S, Sandefjord, Norway.

https://doi.org/10.1016/j.tecto.2018.10.021
Received 4 August 2017; Received in revised form 30 September 2018; Accepted 16 October 2018
Available online 22 November 2018

the convecting core at 445 km below the CMB. High thermal conductivity and minimal convective entrainment in the low-viscosity core fluid might have developed and stabilised such a gradational layer since the Hadean or early Archean.

The primordial bm-dominated cumulates with high Mg/Fe ratios and viscosities may have become convectively aggregated into large refractory domains, remaining neutrally buoyant in the middle to upper parts of the lower mantle and resistant to convective destruction. Late-stage dense BMO cumulates with elevated Fe/Mg ratios relative to the bulk mantle composition might represent a suitable material for 100–200 km thick thermochemical piles at the bottom of the large low S-wave velocity provinces (LLSVPs) under Africa and the Pacific. A degree-2 convection pattern, possibly initiated and stabilised during Earth's early rapid rotation, involving antipodally ascending columns in equatorial positions and an intermediary descending longitudinal belt, might have swept the late-stage, dense bridgmanitic cumulates with high Fe/Mg-ratios, viscosity and bulk modulus towards the root zones of the upwelling columns.

## 1. Introduction

### 1.1. Planetary accretion and core segregation

The internal structures and convective dynamics of the terrestrial planets were likely established during and immediately after their accretion, which was accompanied by pervasive melting, facilitating core-mantle separation and mantle differentiation. The main heat source, causing the earliest melting and magma oceans in small planetesimals, was short-lived radioactive heating, mainly from $^{26}$Al decay (half-life of 0.7 My). This was accompanied by extensive heating from the gravitational segregation of metallic Fe and FeS melts (Rubie et al., 2015a) to form planetesimal cores within the first 2–3 My. The episodic delivery of heat and associated melting and core segregation continued through the late collisional accretion stage. For the Earth, this extended to about 60–100 My after the initial solar nebula processes (Jacobsen et al., 2014; Barboni et al., 2017). The evaporation and condensation processes in the solar nebula are dated to 4567 Ma ($t_0$) by Pb-isotope analyses of Ca-Al-inclusions in chondrites (Connelly et al., 2012). During the protracted giant collision stage, the magma oceans might have crystallised and re-emerged several times.

The “Grand Tack” model for planetary accretion (Walsh et al., 2011; Morbidelli et al., 2012; DeMeo and Carry, 2014) prescribes a heliocentric zonation of O-deficient planetesimals with enstatite and ordinary (S-type) chondritic affinity in the inner disc via C-type planetesimals (carbonaceous chondritic affinity) to $H_2O$-dominated cometary bodies in the outer disc. Recent measurements of a range of isotopic ratios of O, Cr, Ti, Ni, W and Mo provide strong evidence for such a disc zonation with orbital separation of non-carbonaceous (NC, see list of abbreviations in Table 1) and carbonaceous chondrite (CC) materials inside and outside, respectively, of the proto-Jupiter orbit at 1–3 My after $t_0$ (Warren, 2011; Kruijer et al., 2017). The accretion of the large terrestrial planets, Venus and Earth in the inner part of the Solar nebula, over a period of up to 60–100 My, was heterogeneous. Isotopic fingerprints indicate that materials with enstatite chondritic affinity dominate in Mercury, Venus and Earth (e.g. Warren, 2011). A peridotitic bulk mantle composition with a superchondritic (Mg + Fe)/Si ratio can be explained by a combination of processes, including nebular fractionation associated with forsterite condensation (Dauphas et al., 2015), migration of olivine-dominated chondrules towards the accretion disc mid-plane (Hewins and Herzberg, 1996) and impact erosion of protocrusts (Caro et al., 2008). Whereas some studies have concluded that the most oxidised material was delivered during the latest stages (e.g. Rubie et al., 2015b), other results indicate that Earth received more oxidised (mainly carbonaceous) material during the initial 60% growth stage and then predominantly enstatite chondritic material during the last 40% growth (e.g. Badro et al., 2015; Dauphas, 2017). A large proportion of the cumulative core segregation is likely to have occurred in smaller planetesimals and planetary embryos that impacted on and amalgamated with the growing larger planets. Many of the inner solar system planetesimals were likely O-deficient and Mercury-like (e.g. Warren, 2011; Wohlers and Wood, 2015). The extent to which the liquid silicate and metal components were emulsified in each of the impacts, allowing re-equilibration at higher pressures and temperatures than for the original small-body core segregation, has been debated. In high-energy impacts, like those envisaged by Canup (2012) and Cuk and Stewart (2012), such re-equilibration might have been extensive, in contrast to a situation after less energetic impacts.

The presence of Fe-dominated metallic cores in terrestrial planets is a simple consequence of insufficient O/Fe abundance ratios for oxidation of all the elements in the inner parts of stellar accretion discs. Large fractions of iron and siderophile elements, including Si under low O-activity, will therefore segregate as metallic core alloys. The temperature (and pressure) during metal-silicate equilibration and core segregation will govern the widths of the metal-silicate miscibility gaps and thereby the concentration of elements like e.g. Si, Mg and Al in the metal (Wahl and Militzer, 2015; O'Rourke and Stevenson, 2016; Badro

**Table 1**
Summary of key abbreviations and definitions.

**Minerals**
**ol**, olivine; **cpx**, clinopyroxene; **opx**, orthopyroxene; **pl**, plagioclase; **ilm**, ilmenite; **ga**, garnet; **wd**, wadsleyite; **rw**, ringwoodite; **fp**, ferropericlase; **pc**, periclase; **cpv**, Ca-perovskite; **bm**, bridgmanite; **pbm**, post-bridgmanite; **stish**, stishovite, **β-stish**, β-stishovite ($CaCl_2$-structured silica), **seif**, seifertite; **cf**, Ca-ferrite structured Al-rich phase. Although several studies have continued to use the term post-perovskite (ppv) after the IMA-approval of the name bridgmanite for the perovskite-structured $MgSiO_3$-dominated phase (Tschauner et al., 2014), we prefer the term post-bridgmanite for pedagogical reasons. Because the perovskite-structured $CaSiO_3$-dominated phase is commonly referred to as Ca-perovskite, the term post-perovskite for the $MgSiO_3$-dominated high-pressure polymorph of bridgmanite (not strictly isochemical with bm) seems counter-intuitive.

**Mineral components**: **An**, anorthite; **Fo**, forsterite; **En**, enstatite; **Di**, diopside

**Mg-number**, **Mg#** = $100*Mg/(Mg + Fe^{total})$, atomic proportions
**Oxide abbreviations**: System **CMS** (or **MS**), CaO-MgO-$SiO_2$

**Lithological units**
**anorth**, anorthosite; **ROC**, recycled oceanic crust (basaltic composition); **MORB**, mid-ocean ridge basalt; **KREEP**, acronym for the solidified products of the late-stage enriched melts of the lunar magmaocean

**Chondritic groups and asteroid types** (see also Fig. 1)
**CC**, carbonaceous chondrite group; **NC**, non-carbonaceous chrondrite group, including enstatite chondrites, EC (EH and EL subgroup) and ordinary chondrites OC (H, L and LL subgroups). The common asteroidal types (based on reflective properties), which are mention in Section 2.1, are thought to comprise the following chondritic material: **S-type**, OC; **C-type**, CC; **E-type**, EC.

**Mantle and core domains, etc.**
**BEAMS**, bridgmanite-enriched ancient mantle structures, located in the 1100–2600 depth range; **CMB**, core-mantle boundary; **D″-zone**: the lowermost part of the mantle, approximately 300 km thickness, characterised by large radial and lateral heterogeneities; **LLSVPs**, large low shear-wave velocity provinces in the 2200–2900 km depth range; **ULVZs**: ultra-low velocity zones directly above the CMB; **E′-layer**, stagnant outermost core layer with lower seismic velocity and lower density than the underlying and convecting outer core; **MO**, (mantle) magma ocean; **BMO**, basal magma ocean; **EPOC**, seismic reference model for Elastic Parameters of the Outer Core; **PREM**, Preliminary Reference Earth Model.

et al., 2016). The incorporation of Si at high oxygen fugacity and magma ocean FeO content, is facilitated by very high temperatures (e.g. Malavergne et al., 2004; Frost et al., 2008; Tsuno et al., 2013; Fischer et al., 2016; Hernlund, 2016; Laneuville et al., 2018). Decreasing temperatures following the accretion will inevitably lead to protracted chemical exchange between the core and a partly solidified mantle in the large planets (Earth, Venus) with high initial core concentrations of Si. As inferred by e.g. Takafuji et al. (2005), Frost et al. (2010) and Hirose et al. (2017a), the main exchange involves the dissolution of Fe-oxides into the core, accompanied by transfer of silica crystals precipitated in the core to a basal magma ocean (BMO). Hernlund and Geissman (2016) and Brodholt and Badro (2017) reviewed the mineral physics and seismological constraints on a low-velocity and low density stagnant E′-layer of the outermost core, and found that depletion of Si and enrichment of O relative to the convecting outer core may explain its physical properties. Such an E′-layer may thus be a direct trace of core-BMO chemical exchange.

The magma ocean differentiation by crystal fractionation and density-driven segregation will produce early low-density cumulates and late-stage residual melts and cumulates with high density (e.g. Elkins-Tanton, 2012). Partially molten peridotitic and basaltic lithologies are characterised by relatively strong partitioning of Fe to the melt and Mg to the coexisting ferromagnesian minerals in the entire pressure range of the terrestrial planetary mantles. The thermal buoyancy of late-stage dense crystallisation products stored intermittently above the core-mantle boundaries may partly lead to erosion by and entrainment into convective mantle flow. Some of the dense products, however, might have sufficient density to be preserved as long-lasting structures in the thermal boundary layers in the lowermost parts of the mantles (e.g. Labrosse et al., 2007; Steinberger et al., 2010). Such structures are probably present and seismically observed in the D″-layer of the Earth and may be present in other terrestrial planets. To understand the origin of observed structures in the Earth's lower mantle, we first review deep planetary melting, core formation and early mantle differentiation in the terrestrial planets, with an emphasis on the Earth. Subsequently, we discuss core-mantle chemical exchange, mainly during the solidification of a BMO, and its potential role in generating bridgmanitic cumulates with elevated Fe/Mg ratios, which may have been convectively swept into two antipodal thermochemical piles with moderate density excess, high bulk modulus and high viscosity (e.g. Torsvik et al., 2016).

### 1.2. Present structure of the Earth's lower mantle

Recent progress in seismology, mineral physics, geochemistry and geodynamics points to important links between the structure of the lowermost mantle and the Earth's origin, evolution and ongoing dynamics. The seismic structure of the D″ zone is complex, with large radial and lateral variations, especially in shear wave velocity and seismic anisotropy (Romanowicz, 2003; Lay, 2015; Garnero and McNamara, 2008; Garnero et al., 2016). The amplitudes of the S-wave velocity variation of the D″ zone are considerably larger than those in the upper and middle part of the lower mantle (e.g. Romanowicz, 2003; Lay, 2015). The amplitudes (RMS $\delta V_S$) increases from 0.3–0.6% through the 700–2600 km depth range to 0.7–1.5% in the lowermost 300 km. The lateral $V_S$-variation defines two large low shear-velocity provinces (LLSVPs) under the Pacific and Africa, separated by a high-velocity longitudinal belt through the Arctic, Asia, Australia, Antarctica and the Americas, constituting a strong degree-2 spherical harmonic structure, coinciding with the residual geoid (e.g. Dziewonski et al., 2010). Although the low $V_S$ anomalies are strongest in the lowermost 300 km of the mantle, Hernlund and Houser (2008) identified them up to at least 700 km above the CMB. Additional ultra-low velocity zones (ULVZs) of 10–40 km thickness with P- and S-velocity reductions of 10–30% are present directly above the CMB (e.g. Lay, 2015). Although the distribution of the ULVZs might be irregular, they seem to be preferentially confined to the margins of the LLSVPs and especially to the roots of large plumes (McNamara et al., 2010; French and Romanowicz, 2015; Yuan and Romanowicz, 2017).

The LLSVP margins are locally steep and seismically sharp (Garnero and McNamara, 2008), making them favourable sites for the generation of mantle plumes. Mantle material sinking in the wide belt between the two LLSVPs is deflected laterally above the CMB, heated during transport along this thermal boundary layer and deflected upwards in the plume generation zones at the hot LLSVP margins (Torsvik et al., 2016). Paleogeographic reconstructions of large igneous provinces (LIPs) and kimberlites with ages covering the last 540 My indicate that the eruption sites were preferentially above the LLSVP margins (e.g. Burke and Torsvik, 2004; Torsvik et al., 2010; Torsvik et al., 2006; Torsvik et al., 2014). The degree-2 convection and the residual geoid, involving antipodal upwelling over the LLSVPs and downwelling in the longitudinal high-$V_S$ belt are geometrically linked to the rotation axis (e.g. Dziewonski et al., 2010; Torsvik et al., 2016), and were possibly initiated and stabilised during an early period of more rapid rotation. The large S-wave velocity amplitude of the lowermost mantle is related to the lateral temperature differences, but possibly also to 100–200 km thick thermochemical LLSVP-piles (layers) with high viscosity, high bulk modulus and slightly elevated density. Seismic discontinuities observed at heights of 250–320 km above the CMB in regions of the longitudinal high-velocity belt (e.g. Cobden et al., 2015; Lay, 2015) have been attributed to the transformation of the Earth's most abundant mineral bridgmanite (bm) to post-bridgmanite (pbm). The large positive dp/dT-slope of the bm-pbm transition will, for a given lithology, displace the bm-pbm transition to shallower depths in regions with low D″ temperatures. It will also promote a reverse transformation to the high-entropy phase, bm, near the hot CMB (Hernlund et al., 2005). Pbm has lower viscosity and bulk modulus, but higher shear modulus, than bm (Wookey et al., 2005; Amman et al., 2010; Cobden et al., 2015; Garnero et al., 2016; Koelemeijer et al., 2018), and ferropericlase has also considerably lower bulk modulus and viscosity than bm (Irifune and Tsuchiya, 2015; Marquardt and Miyagi, 2015). Cool peridotitic material with fp and pbm, which is dominant in the longitudinal high-velocity belt, will therefore have considerably lower viscosity and bulk modulus than bridgmanitic material with about 16 mol% of the $FeAlO_3$ component, which may form a 100–200 km thick base layer in the LLSVPs (Section 4.7; Deschamps et al., 2012; Ballmer et al., 2016; Mohn and Trønnes, 2018). The density excess of the LLSVPs relative to the longitudinal belt is inferred to be 1.0–1.5% at 2850 km depth from body wave travel times, normal-mode splitting functions, long-period waveforms and free-air gravity constraints (Ishii and Tromp, 1999; Moulik and Ekström, 2016). Solid Earth tide tomography indicates a similar density excess of 0.75% in the lowermost 340 km, and probably 1.5% in the lowermost 170 km (Lau et al., 2017). Based on Stoneley mode analysis, Koelemeijer et al. (2017) estimated a maximum thickness of about 100 km for thermochemical LLSVP layers with slightly elevated density. Based on mineral physics modelling using the SP12RTS tomography model, however, Koelemeijer et al. (2018) infer the presence of pbm in basaltic LLSVP material up to about 300 km above the CMB (see also Fig. 23). The stabilisation of pbm in basaltic rocks at high temperature and relatively low pressure is broadly consistent with the phase relations in the systems $MgSiO_3$-$FeAlO_3$, $MgSiO_3$-$FeAlO_3$ and $MgSiO_3$-$Al_2O_3$ (Mohn and Trønnes, 2018). The origin, positioning and subsequent stabilisation of two antipodal and equatorial thermochemical piles may be governed by a global degree-2 convection pattern (e.g. Wolf et al., 2015), which might conceivably have existed since the magma ocean stage in the early Hadean.

Suggested candidate material for dense thermochemical piles include recycled oceanic crust (basaltic composition, e.g. Hirose et al., 2005; Koelemeijer et al., 2018), cumulates and solidified melts formed in a melt accumulation zone at 400–500 km depth (Lee et al., 2010) or dense cumulates from the final crystallisation of a basal magma ocean above the CMB (Labrosse et al., 2007). From a seismic sensitivity analysis, Deschamps et al. (2012) concluded that Fe-rich bm is the most

suitable high-density LLSVP material. Ballmer et al. (2016) and Torsvik et al. (2016) suggested that the LLSVPs may include lower stable cumulate-based layers with overlying basaltic material, which may be neutrally buoyant near the CMB. Basaltic material with higher bulk modulus than ferropericlase-bearing peridotite may therefore show lava lamp behaviour (e.g. Torsvik et al., 2016) and be entrained in hot and rising mantle flow, before acquiring sufficient density to partially stagnate and sink from about 1000 km depth (Ballmer et al., 2015).

Seismologists have mostly explained the ULVZ properties by partially molten materials, although solid materials in the form of Fe-rich pbm, subducted banded iron formations or $FeO_2H_x$ have been suggested (Mao et al., 2006; Dobson and Brodholt, 2005; Liu et al., 2017). A commonly invoked partially molten material is basaltic recycled oceanic crust (e.g. Ohtani and Maeda, 2001; Andrault et al., 2014; Pradhan et al., 2015; Torsvik et al., 2016; Baron et al., 2017), but subducted slab-derived metallic melt (Liu et al., 2016) and surviving dense residual magma ocean liquid with high Fe/Mg-ratios and incompatible element concentrations (Trønnes, 2010) might be alternatives. In spite of their limited thickness, partially molten ULVZs must have a minimum of convective vigour in order to prevent melt-solid gravitational separation (e.g. Hernlund and Jellinek, 2010). This may promote ULVZ-core exchange and restrict the permissible ULVZ compositions to those that approach chemical equilibrium with the core.

Becker et al. (1999) and Ballmer et al. (2017) found that high-viscosity domains in the lower mantle would be convectively aggregated into large (500–2000 km diameter) blobs or BEAMS (bridgmanite-enriched ancient mantle structures). Such structures could be formed either as cumulates during early crystallisation in the magma ocean(s) or as melting residues from plume-associated and deep melting of hot, but solid, mantle shortly after the BMO solidification. In Section 4 we review how core-mantle chemical exchange during and after the solidification of a basal magma ocean can produce neutrally buoyant early bridgmanitic cumulates, as well as relatively bm-rich thermochemical piles with elevated Fe/Mg-ratio and density. These two types of bm-rich domains would have high viscosity and bulk modulus compared to the ambient lower mantle.

### *1.3. The outermost core - a record of Hadean and Archean metal-silicate interaction?*

Chemical core-BMO exchange might be recorded by the seismic structure of the outer core (e.g. Hernlund and Geissman, 2016; Brodholt and Badro, 2017). Analysis of differential SmKS wave arrivals indicate a pronounced velocity gradient ($V_P = V_\Phi$) in the outermost 300–450 km of the core (Lay and Young, 1990; Garnero et al., 1993; Helffrich and Kaneshima, 2010; Kaneshima and Helffrich, 2013; Kaneshima and Matsuzawa, 2015; Kaneshima, 2018) compared to that of the PREM model (Dziewonski and Anderson, 1981). The strong velocity decrease towards the CMB has been ascribed to a stratified and stagnant low-velocity layer of the outermost core (ref. above; Buffett, 2010; Buffett and Seagle, 2010; Gubbins and Davies, 2013; Hernlund and McNamara, 2015). Brodholt and Badro (2017) introduced the term E′-layer for the presumed stagnant and gradational zone, which must have lower density than the underlying convecting core. As an example, the KHOMC model of Kaneshima and Helffrich (2013) involves a velocity contrast ($\Delta V_P$) relative to PREM, varying from −0.43% at the CMB to zero about 445 km below the CMB (e.g. Kaneshima, 2018). The mineral physics model of Brodholt and Badro (2017), combined with the $\Delta V_P$ (KHOMC-PREM), yields a corresponding density contrast ($\Delta\rho$) of −0.98% at the CMB, assuming that the low velocity and low density in the uppermost core are caused by Si-depletion and O-enrichment. This is discussed further in Section 4.

Irving et al. (2018) have recently developed the new Elastic Parameters of the Outer Core (EPOC) seismic model, incorporating the observed velocity and density gradients in the outermost core. Although the EPOC model has higher density throughout the entire core, the $\Delta V_P$ relative to PREM is −0.87% at the CMB. If the PREM density-versus-depth curve is displaced upwards to coincide with the corresponding EPOC curve in the deeper part of the outer core, the CMB density deficit of EPOC relative to the PREM-gradient would be −0.62%. Irving et al. (2018) argue that the EPOC model is consistent with a fully mixed and adiabatic outer core. This would require a compressible outer core alloy with a lower bulk modulus than that of PREM. The EPOC model, however, might not exclude the presence of a stagnant, non-convecting E′-layer.

The very low viscosity and high thermal diffusivity of the core fluid reduces the tendency for viscous entrainment, and Hernlund and McNamara (2015) advocate long-term stability for a low-density stagnant E′-layer above the convecting core. With reference to Sreenivasan and Gubbins (2008), they also argue that such a layer may have a stabilising effect on the dynamo. The requirement of reduced density in such a stagnant layer above the convecting core has been difficult to reconcile with the fact that each of the outer core light element candidates, Si, O, S and C, increases the $V_P$ of the core alloy (Badro et al., 2014; Brodholt and Badro, 2017). Si and O, however, yield the largest and the smallest velocity increases, respectively. For the fluid outer core, the bulk modulus is directly proportional to $V_P^2$. An EPOC model requirement of high compressibility for the outer core alloy (Irving et al., 2018) would therefore favour high proportion of O relative to the other light element candidates, especially in the outermost layer. Here we explore the consequences of chemical interactions between the core and a basal magma ocean, assuming the presence of a stagnant outer core layer as delineated by Brodholt and Badro (2017) and Kaneshima (2018).

## 2. Mantle and core composition in terrestrial planets

Following a review of the meteoritic (asteroidal) building materials of the terrestrial planets, we develop estimates for their present core and mantle compositions. In a wide sense, we also include the Moon and the second largest and differentiated asteroid, Vesta, as terrestrial planets. A pronounced heliocentric zonation in oxygen fugacity and composition is rooted in the original protoplanetary disc structure. In addition, the contributions of different materials during the progressive growth of the planetary embryos and planets were affected by disc disruption caused by an inward, followed by an outward, migration of the giant planets (the “Grand Tack” model). The planetary sizes and pressure regimes also governed the average and maximum internal temperatures of accretion and core segregation, which in turn influenced the core-mantle chemical equilibrium (or approach to equilibrium). In the largest planets, especially in Earth and Venus, the core and mantle compositions established during the earliest Hadean maximum temperature stage, would therefore tend to change during the subsequent cooling as described in Section 4. We assume that the current CMB temperature of the Earth is 4000 K, in general agreement with outer core temperature estimates of Anzellini et al. (2013), Hirose et al. (2013) and Olson et al. (2015), as well as the solidus of basaltic material determined by Pradhan et al. (2015). In comparison, Nimmo (2015) presented a temperature estimate of 4190 K for the outermost core.

### *2.1. From chondritic building materials to peridotitic mantles*

Differentiated planetesimals and planetary embryos, and ultimately the fully grown terrestrial planets, accreted initially from primitive chondritic materials, spanning a wide range of Fe/O contents (Fig. 1). Whereas the CI and CM carbonaceous chondrites have their entire iron inventory oxidised, the enstatite chondrites have nearly Fe-free ferromagnesian minerals like olivine and pyroxenes, with iron as separate Fe-Ni-metal alloy and sulfide. The ordinary chondrites, grouped as H (highest Fe content), L (low Fe) and LL (lowest Fe), represent an intermediate range of Fe/O ratios. Recent models for planetary accretion

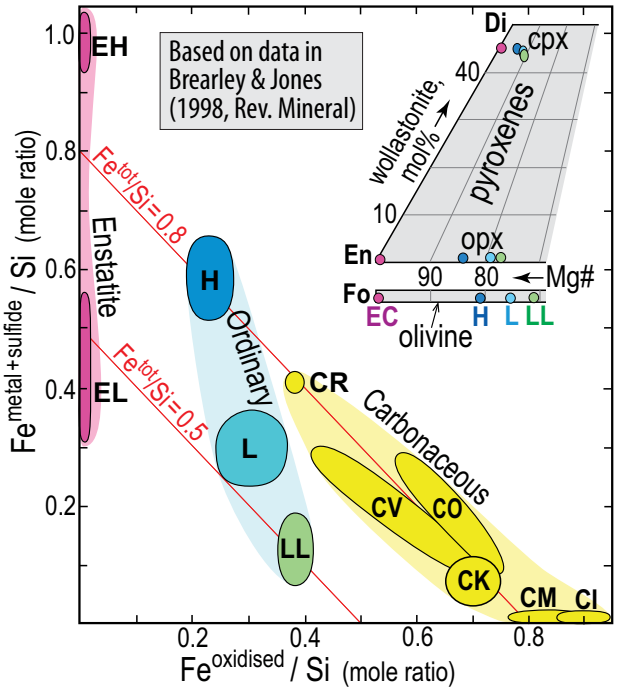


**Fig. 1.** The composition of chondrites. The inset figure shows the average pyroxene and olivine compositions of enstatite and ordinary chondrites (Brearley and Jones, 1998). The three main chondrite groups are abbreviated EC (comprising the EH and EL subgroup), OC (comprising H, L and LL) and CC (carbonaceous chondrites). In the text, references are also made to the non-carbonaceous, NC group (comprising EC and OC). The aubrite meteorites (not on the figure) are enstatite achondrites (melted and differentiated EC-material). The Theia planetary embryo (10–20% of Earth's mass), causing the late Moon-forming impact, might have had Mercury-like composition (Wade and Wood, 2016) and the O-isotope composition is aubrite-like (Greenwood et al., 2018). Mg# = 100 Mg / (Mg + Fe).

predict a zonation from the most reduced enstatite chondritic material near the Sun with progressively more oxidised material outwards (e.g. Walsh et al., 2011; Morbidelli et al., 2012; Rubie et al., 2015b). $H_2O$-rich cometary material dominates in the outermost reaches of the Solar system, where it could condense and aggregate beyond the "frost line". Although this initial zonation was largely disturbed by the inward and outward migration of the outer giant planets (Walsh et al., 2011) and the following accretion of the innermost planets, it is still roughly reflected in the distribution of asteroids (DeMeo and Carry, 2014) and the icy Kuiper belt objects. The Hungaria asteroids at about 1.9 AU have the largest proportion of E-type asteroids (enstatite-type), which are the probable sources of enstatite chondrites and aubrites. The proportion of the S-type asteroids, which are likely sources of ordinary chondrites, peaks in the inner part of the main belt (2.1–3.3 AU). The relative proportion of the C-type (carbonaceous) asteroids increases outwards through the main belt. The increase in the proportion of carbonaceous-like materials continues further out via the Cybele (3.3–3.7 AU) and Hilda (3.7–4.0 AU) zones to the Jupiter Trojans (5.1–5.3 AU).

Recently acquired and compiled O-Cr-Ti-Ni-W-Mo-isotopic data show a very distinct separation between carbonaceous and non-carbonaceous chondritic material (the CC and NC groups; Warren, 2011; Dauphas, 2017). Age estimates based on the iron meteorites, which are also divided between these two well-separated groups, indicate that the orbital separation and establishment of the CC and NC groups occurred 1–2 My after $t_0$ during the early growth of Jupiter, before its inward migration caused disc perturbation at 4–5 My (Kruijer et al., 2017). In terms of the O-Cr-Ti-Ni-isotopes, the Earth and Mars compositions fall within the NC group space but in the area closest to the CC group space. Warren (2011) used the geometrical relations in diagrams with $\varepsilon^{50}$Ti versus $\varepsilon^{54}$Cr and $\Delta^{17}$O versus $\varepsilon^{54}$Cr, with wide separation of the NC and CC groups, to estimate that Earth and Mars contain CC-fractions of about 25 and 5%, respectively. The early termination of Mars accretion at the planetary embryo stage might be the main reason for its lower CC-proportion. The geochemical modelling by Dauphas and Pourmand (2011) indicates that 80% and 90% of Mars accreted within the first 2.9 and 3.6 My after $t_0$, respectively. The O-Cr-Ti-Ni-isotopic relations also serve to emphasise the similar compositions for Earth and Moon and their resemblance to enstatite chondrites, and specifically to the EH subgroup, supporting the inference of an enstatite chondrite Earth model by e.g. Javoy (1995), Javoy et al. (2010) and Dauphas (2017). A recent Mo-Nd-isotopic study of Render et al. (2017) shows that the Earth's mantle has larger proportions of s-process nuclides of these elements than the commonly sampled EC and OC material derived from the asteroid belt. The Earth, and presumably Mercury and Venus to an even larger extent, may therefore comprise EC-type material which originated closer to the Sun and is not directly represented by samples in our meteorite collections. A high-resolution O-isotope investigation by Greenwood et al. (2018) shows that Earth and the Moon have also strong affinities with the aubrite meteorites (enstatite achondrites). Wade and Wood (2016) suggested that the late Earth-impactor, Theia, was a highly reduced Mercury-like planet or planetary embryo. As discussed below, the incorporation of EC- or aubrite-like material into the Earth, Moon and possibly Venus was probably accompanied by processes that increased the Mg/Si ratio.

The isotopic data for the Vesta samples (the HED meteorites) compiled and presented by Dauphas (2017), indicate that Vesta has even lower $\varepsilon^{54}$Cr, $\varepsilon^{50}$Ti and $\varepsilon^{48}$Ca than Mars and the ordinary chondrites (OC), and is therefore even further away from the CC compositional group. Only the ureilite achondrites are compositionally further removed from the CC group than the HED meteorites, indicating that Vesta may have accreted from mixtures of ordinary chondritic and ureilitic material. Vesta's composition is therefore consistent with geochronology, indicating that its accretion and core segregation was terminated at the planetesimal stage, within about 1 My after $t_0$ (Touboul et al., 2015), well before disc disruption (Kruijer et al., 2017).

The accretion and processing of chondritic material via planetesimals and planetary embryos to form planets are complex processes, involving impact erosion, partial volatilisation, partial melting and silicate-metal separation (e.g. Jacobsen et al., 2014; Rubie et al., 2015b). Several processes might have increased the Mg/Si ratio of the planetary bulk silicate fractions, moving the composition from "chondritic" or "pyroxenitic" to peridotitic. Nebular fractionation stemming from forsterite condensation (Dauphas et al., 2015) would increase the Mg/Si ratio of the condensate before the aggregation of dust to form pebbles and planetesimals. At the same time, the interaction of turbulent solar nebula gas and dust with fluctuating magnetic fields produced Ca-Al-inclusions and chondrules. The chondrules, which have elevated Mg/Si ratios compared to the chondrite matrix, may have partially segregated to the disc midplane where planetesimal growth was more efficient (e.g. Hewins and Herzberg, 1996; Caro et al., 2008). Preferential incorporation of Si into planetary cores under reducing conditions or at very high temperatures, as well as repeated episodes of impact erosion and partial volatilisation of protocrust on planetesimals and planetary embryos, would also increase the Mg/Si ratio of the remaining mantle silicate. Chondrule concentration and protocrustal impact erosion would also deplete the bulk silicate planetary compositions in the most incompatible trace elements, causing superchondritic Sm/Nd ratios and elevated $^{142}$Nd/$^{144}$Nd and $^{143}$Nd/$^{144}$Nd ratios (e.g. Caro et al., 2008).

Whereas the Earth's upper mantle is peridotitic, various studies based on mineral elasticity and seismic wave speeds have diverged in their inferences of whether the lower mantle composition is peridotitic or pyroxenitic (e.g. Murakami et al., 2012). Based on recent elasticity measurements of a bm composition with 10% $FeAlO_3$ component and elasticity modelling of alternative mineral assemblages, Kurnosov et al. (2017) concluded that the lower mantle is broadly peridotitic

(pyrolitic), at least in the 800–1200 km depth range. With increasing pressure, their model results yield increasingly negative and positive deviations from PREM for the P- and S-wave velocities, respectively. The iron spin-pairing transition of fp might increase the deviations further, but a reduction of the $Fe^{3+}/Fe^{total}$ ratio (and $FeAlO_3/FeSiO_3$ ratio) of bm, observed by Prescher et al. (2014) at 100–130 GPa, might reduce the deviations. Table 2 presents our estimated major element compositions of the cores and primitive (bulk) mantles of the terrestrial

**Table 2**
Planetary core and mantle compositions.

Core composition, wt%

| | Fe + Ni adjusted to yield 100% | | | | | Core composition, atom% | | | | | Bulk planetary |
|---|---|---|---|---|---|---|---|---|---|---|---|
| | Fe | Ni | Si | O | S | Fe | Ni | Si | O | S | log $f_{O2}$ (ΔIW) |
| Mercury | 77.7 | 4.3 | 15.0 | – | 1.2 | 68.7 | 3.62 | 25.8 | – | 1.81 | −4.56 |
| Venus | 86.2 | 5.3 | 6.2 | 2.3 | – | 77.2 | 4.52 | 11.0 | 7.19 | – | −2.41 |
| Earth | 87.9 | 5.5 | 3.6 | 3.0 | – | 79.4 | 4.72 | 6.46 | 9.45 | – | −2.21 |
| Moon | 87.9 | 6.75 | – | – | 5.35 | 84.8 | 6.20 | – | – | 8.99 | −1.87 |
| Mars | 77.1 | 8.6 | – | 0.2 | 14.1 | 69.8 | 7.40 | – | 0.63 | 22.2 | −1.36 |
| Vesta | 77.0 | 10.2 | – | – | 12.8 | 70.6 | 8.90 | – | – | 20.5 | −1.10 |

Primitive mantle composition, wt%

| | $SiO_2$ | $TiO_2$ | $Al_2O_3$ | $Cr_2O_3$ | NiO | MnO | FeO | MgO | CaO | $Na_2O$ | $K_2O$ | S | Sum |
|---|---|---|---|---|---|---|---|---|---|---|---|---|---|
| Mercury | 57.7 | – | 3.34 | – | – | 0.11 | 0.47 | 30.1 | 2.64 | 0.24 | – | 10 | 99.6* |
| Venus | 45.0 | 0.20 | 4.45 | 0.38 | 0.25 | 0.14 | 6.30 | 39.6 | 3.55 | 0.36 | 0.03 | – | 100.3 |
| Earth | 45.0 | 0.20 | 4.45 | 0.38 | 0.25 | 0.14 | 8.05 | 37.8 | 3.55 | 0.36 | 0.03 | – | 100.2 |
| Moon | 44.6 | 0.17 | 3.9 | 0.47 | – | 0.17 | 12.4 | 35.1 | 3.30 | – | – | – | 100.1 |
| Mars | 44.4 | 0.14 | 3.02 | 0.76 | 0.23 | 0.46 | 17.9 | 30.2 | 2.45 | 0.50 | – | – | 100.1 |
| Vesta | 43.4 | 0.10 | 2.56 | – | – | – | 23.9 | 27.9 | 2.10 | 0.06 | – | – | 100.0 |

*The Mercury sum includes a subtracted amount of O, corresponding to 10 wt% S

Primitive mantle composition, normalised to cation%

| | Si | Ti | Al | Cr | Ni | Mn | Fe | Mg | Ca | Na | K | Mg# | Mg/Si | *M/S | *CM/S |
|---|---|---|---|---|---|---|---|---|---|---|---|---|---|---|---|
| Mercury | 52.3 | – | 3.56 | – | – | 0.08 | 0.36 | 40.7 | 2.56 | 0.42 | – | 99 | 0.78 | 0.74 | 0.79 |
| Venus | 37.5 | 0.13 | 4.38 | 0.25 | 0.17 | 0.10 | 4.40 | 49.3 | 3.17 | 0.58 | 0.03 | 92 | 1.31 | 1.30 | 1.39 |
| Earth | 37.9 | 0.13 | 4.42 | 0.25 | 0.17 | 0.10 | 5.67 | 47.5 | 3.21 | 0.59 | 0.03 | 89 | 1.25 | 1.27 | 1.36 |
| Moon | 38.4 | 0.11 | 3.96 | 0.32 | – | 0.12 | 8.93 | 45.1 | 3.05 | – | – | 83 | 1.17 | 1.29 | 1.36 |
| Mars | 39.4 | 0.09 | 3.15 | 0.53 | 0.16 | 0.35 | 13.3 | 39.9 | 2.33 | 0.86 | – | 75 | 1.01 | 1.28 | 1.35 |
| Vesta | 39.3 | 0.07 | 2.73 | – | – | – | 18.1 | 37.7 | 2.04 | 0.11 | – | 68 | 0.96 | 1.33 | 1.38 |

*M = Mg+Fe+Mn+Mi+Cr+Ti, C = Ca+Na+K, S = Si+Al

**References and procedures**. Elements with possible core concentrations below 0.5 wt% are not included. ***Mercury***: The core and mantle compositions were developed from core and mantle density and size constraints (Hauck et al., 2013; Knibbe and van Westrenen, 2018) and phase relations (Morard and Katsura, 2010; Malavergne et al., 2004, 2014; Wood and Kiseeva, 2015). ***Venus***. Core: Si and O are chosen to lie on a vector from the Mercury (15 wt% Si, 0 wt% O) to the Earth core composition, with the distance along the vector scaled to the $FeO^{mantle}$ concentrations (Mercury, Venus and Earth: 0.47, 6.30 and 8.05 wt%, respectively). Mantle: compositions identical to Earth, except for an FeO content of 6.3 wt% (1.8 wt% lower than in Earth's mantle) from Mittlefehldt et al. (2008). By keeping the same FeO + MgO total in Venus and Earth, the Venus MgO content was increased from 37.8 wt% (in Earth) to 39.6 wt%. ***Earth***. Core: a composition within the Badro et al. (2015) range, but near the low-O and high-Si end of the range (see further explanation in Table 3, caption). Because the inner core is only 4 vol% of the core and a suggested outermost E′-layer (e.g. Brodholt and Badro, 2017) is less constrained, we assume for simplicity that the given bulk core composition is also representative for the outer convecting core. Mantle: McDonough and Sun (1995, Pyrolite1). ***Moon***. Core: Weber et al. (2011) used seismological data to resolve a partially molten lowermost mantle, a liquid outer core (62 vol%) and an inner solid core. Based on their Fig. 4, with S as the dominating light element in the outer core, an inferred CMB temperature of 1700 K (partially molten lowermost mantle), the outer core and bulk core would have 11.0 and 5.35 wt% S, respectively. This is consistent with the mineral physics based estimate of Antonangeli et al. (2015) and recent evidence that Theia was a strongly reduced Mercury-like object (Wade and Wood, 2016; Dauphas, 2017; Greenwood et al., 2018). Mantle: O'Neill (1991a). ***Mars***. Core: the estimates of Khan and Connolly (2008) and Khan et al. (2018) with 22–25 wt% S and 15–19 wt% S, respectively, are higher than the 11–16 wt% range of Dreibus and Wänke (1985), Lodders and Fegley (1997), Sanloup et al. (1999) and Stewart et al. (2007). Our chosen composition with 14.1 wt% S and 0.2 wt% O, within the 11–16 wt% S range, is a linear extrapolation of the eutectic compositions in the FeNi-FeS-FeO ternary system with Fe/Ni = 9 via 6 and 16 GPa (Fig. 8) to the Mars CMB pressure of 20 GPa. Mantle: Tuff et al. (2013), based on Dreibus and Wänke (1985). This composition has Mg# of 75, in agreement with Khan et al. (2018). ***Vesta***, core and mantle: Toplis et al. (2013), model based on ordinary chondrites (H-chondrite model).

**Fe/Ni ratio**. ***Mercury***: 18, average ratio for kamacite in the EH chondrite group (Brearley and Jones, 1998, Table A3.32). ***Venus*** and ***Earth***: about 16, the ratio Badro et al. (2015) used for Earth. ***Moon***: 13, intermediate between Mars and Earth. ***Mars***: 9, corresponding to the FeNi-FeS-FeO ternary system in Fig. 8. **Vesta**: 7.6, resulting from the model of Toplis et al. (2013).

**Bulk planetary** log $\mathbf{f_{O2}}$ (ΔIW): concept and calculations are described in the text. The $f_{O2}$ is most sensitive to the $FeO^{mantle}$ concentration. The core and mantle composition of Venus and Earth, in particular, probably evolved considerably by core-mantle chemical exchange during the Hadean (see text). The tabulated core and mantle compositional estimates refer to the presumed present compositions.

The two right-hand columns for the cation-normalised mantle compositions indicate that the Mercury mantle composition is more silica-rich than a pyroxenite, whereas the other mantle compositions are peridotitic. The lower parts of the mantles of Earth (lower 1100 km, about 25% of the mantle), and possibly Venus, may contain significant proportions of large bridgmanite-enriched domains, in the form of (1) refractory blobs and/or BEAMS and (2) thin thermochemical layers with moderately high Fe/Mg-ratio in the two antipodal LLSVPs (see text). Such domains are not accounted for in the tabulated peridotitic model compositions for the Earth and Venus mantles.

planets. The mantle compositions are peridotitic, except for the Mercury mantle, which has very low (Mg + Fe)/(Si + Al) ratio (and "M/S" and "CM/S" ratios in Table 2; e.g. Malavergne et al., 2010; Nitter et al., 2011). That peculiar aspect of the Mercury mantle is likely related to the effects of enstatite chondritic precursor materials and extremely reducing conditions with strong partitioning of Fe into the core and with an additional FeS-dominated CMB layer. The high Si content of the Mercury core is insufficient to compensate for the extreme FeO-depletion in the mantle.

### 2.2. Mantle and core compositions, Fe/O and core/mantle ratios

With some exceptions, the core/mantle mass ratios of the terrestrial planetary bodies are closely related to the bulk Fe/O ratio. These relations with rough estimates of the core and mantle (bulk silicate) compositions are shown schematically in Fig. 2 and Table 2. Recent spacecraft-based observations and analysis of Mercury and Vesta (e.g. Smith et al., 2012; Russell et al., 2012), combined with steady growth of meteorite collections and characterisation of meteorites from Mars, Vesta and the Moon, have contributed to our insights into the structure, composition and formation of these planetary bodies. Whereas Fig. 2 is based on information from a range of sources, the main constrains for Mercury, Venus, Mars and Vesta are the surface compositions from meteorites (Mars and Vesta), infrared, X-ray, γ-ray and neutron spectroscopy and the moment of inertia factors (e.g. Nitter et al., 2011; Peplowski et al., 2011; Russell et al., 2012; Smith et al., 2012). The Moon and especially the Earth have been more extensively investigated by sampling and geophysics. The construction of Fig. 2 and Table 2 was aided by cosmochemical models, mineralogical and mineral physical relations and metal-sulfide-silicate partitioning of key elements under variable pressure, temperature and oxygen fugacity conditions. Apart from cosmochemical models, an additional principle is that the FeO-contents are roughly equal in the planetary mantles and their associated surface basalts, which are generally formed by melting at 0–3 GPa. The exchange partition coefficients $K_D^{min/melt}(Fe/Mg) = (Fe/Mg)^{min}/(Fe/Mg)^{melt}$ (Roeder and Emslie, 1970; Trønnes et al., 1992) for olivine, pyroxene and garnet are mostly constant at 0.3–0.5 in this pressure range. Common basalts on Earth have about 8 wt% FeO, which is also found in variably melt-depleted mantle peridotites with MgO-contents covering the 35–45 wt% range (e.g. Palme and O'Neill, 2003). The data sources and procedures for estimating core and mantle compositions are given in Table 2 and discussed further in the text.

The mantle FeO contents appear to be negatively correlated with the core fractions (Fig. 2, inset panel, modified from Mittlefehldt et al., 2008), reflecting an increasing availability of oxygen with increasing heliocentric distance. The tiny core fraction of the Moon, and possibly a slightly elevated core fraction of the Earth, is readily explained by Earth-Theia collisional effects (see below). The accumulated core and mantle pairs are generally removed from chemical equilibrium. This is partly due to the heterogeneous accretion during time periods of up to 60–100 Ma for Earth and Venus, combined with a high density contrast between mantle and core materials. High temperature during the segregation of core metal from silicate magma oceans did also contribute to the presently observed chemical disequilibrium. Based on geochemical comparisons of Earth, Mars, iron meteorites and other achondrites with the non-carbonaceous and carbonaceous chondrite groups (Warren, 2011; Kruijer et al., 2017), it is expected that the accreting material for the two largest planets, Venus and Earth, inside the 1 AU heliocentric distance, changed considerably through time (e.g. Rubie et al., 2015b).

The lunar outlier in terms of a tiny core fraction (Fig. 2) is readily explained by accretion from a vapour- and melt-dominated disc of ejected and largely evaporated mantle (silicate) material surrounding the Earth after the Theia collision (e.g. Pahlevan and Stevenson, 2007; Wang and Jacobsen, 2016). The higher $FeO^{mantle}$ content of about 12 wt % in the Moon compared to 8 wt% in the Earth may be related to metal-silicate separation in a more oxidised lunar magma ocean, 60–100 My after the initial planetesimal accretion in an early H-dominated solar nebula. An alternative or complementary mechanism is the transfer Fe-oxides from the Earth's basal magma ocean to an O-undersaturated protocore (Section 4). Although the Earth's mantle has higher FeO than that of Venus, the core fraction is also slightly larger (Fig. 2). This is consistent with more impact erosional loss of the Earth's mantle associated with the Theia-collision.

Although the use of bulk planetary oxygen fugacity, assuming core-mantle equilibrium, may seem unwarranted, the concept of relating the FeO and Fe concentrations of the mantle and core, respectively, to the iron-wüstite (IW) buffer reaction is a simple and useful measure of the accretionary Fe/O ratio and the planetary O-content. The $f_{O2}$ relative to the IW buffer reaction: $O_2 + 2\ Fe = 2\ FeO$, can be expressed as:

$$\log f_{O2}(\Delta IW) = 2 \log (a_{FeO}^{mantle}/a_{Fe}^{core}),$$

where $a_{FeO}^{mantle}$ is the activity of FeO in the mantle, i.e. in the silicate magma ocean.

A rough $f_{O2}$ calculation for the bulk terrestrial planets (Table 2) is based on the estimated oxide and element concentrations, by converting wt% to mol-fractions. In accordance with Malavergne et al. (2014), we assume ideal mixing of Fe in the core alloy, as well as for FeO in the silicate when $FeO^{mantle} < 0.5$ wt%. An activity coefficient of 1.1 for $FeO^{silicate}$ is used for higher concentrations. Because the $a_{FeO}^{mantle}$ term covers a much wider range than $a_{Fe}^{core}$, the resulting log $f_{O2}$ for the bulk mantle-core pairs is determined mainly by the former.

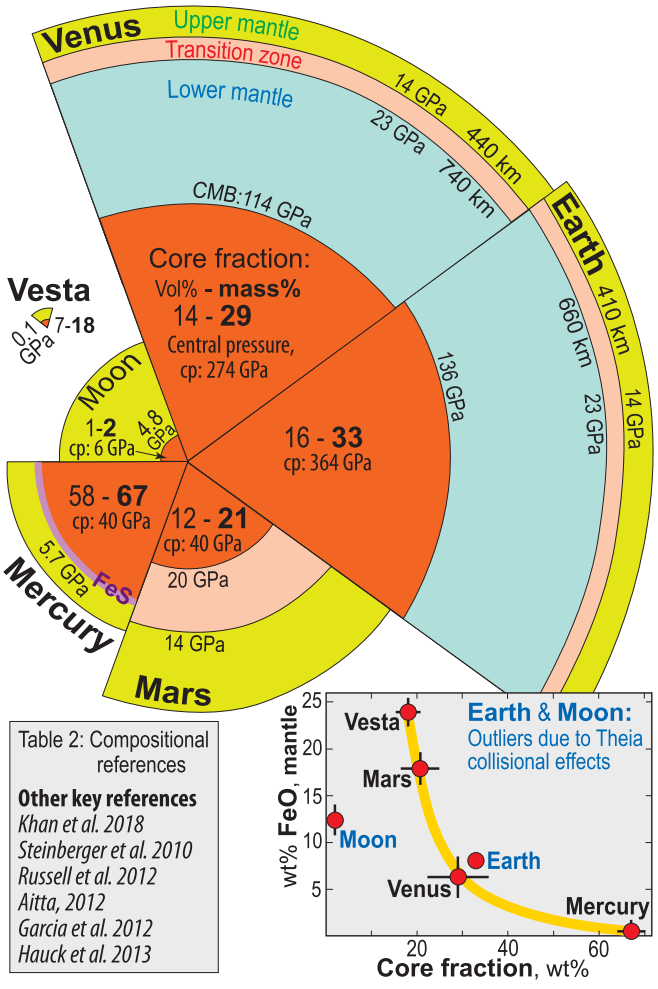


**Fig. 2.** Sizes, core fractions and mantle FeO contents of the terrestrial planetary bodies. The core and mantle compositions are given in Table 2.

The mantle FeO concentrations yield "bulk planetary oxygen fugacities" for Mercury, Venus, Earth, Moon, Mars and Vesta, expressed as log units below the IW buffer ($-\Delta$IW), of 4.6, 2.4, 2.2, 1.9, 1.4 and 1.1, respectively (Table 2), illustrating the increasing activity of oxygen outwards through the terrestrial planetary zone.

In the following, we review the main constraints on the core and mantle compositions of the terrestrial planets, summarized in Table 2. Although the light element contents of the cores are still uncertain, important insights are provided by (1) phase relations of some of the key Fe-alloy systems, (2) chemical and mineralogical data for Earth and meteorites (including those from Vesta, Mars and the Moon), (3) seismological data for the Earth and Moon and the mass distribution within the other planetary bodies. Whereas Si, S and O are probably the three dominant light elements (references in Table 2 and e.g. Hirose et al., 2013), C and H have been suggested as additional or even alternative light elements in the Earth's core (e.g. Wood, 1993; Okuchi, 1997; Ohtani et al., 2005; Iizuka-Oko et al., 2017). Iron isotopic fractionation, however, indicates that C and H are probably not important core components (Shahar et al., 2016). For H, this conclusion is supported by a recent experimental study, finding very low metal-silicate partitioning coefficients (Clesi et al., 2018). Other studies based on cosmochemistry and phase relations also conclude that the Earth's core has negligible concentrations of C and H (e.g. Hirose et al., 2013; Badro et al., 2015; Fischer et al., 2015; Rubie et al., 2015b). Steenstra et al. (2017) have recently suggested that the Moon's small core may have a significant C content of 0.6–4.8 wt%. Our lunar core composition in Table 2, however, is based on recent evidence that the late Earth-impacting Theia was probably strongly reduced and Mercury-like (e.g. Dauphas, 2017; Greenwood et al., 2018), making S the most likely light element candidate (Wade and Wood, 2016). The lunar core segregation would have occurred at much higher $f_{O2}$ than that of the impacting body, leading to the scavenging of S as FeS from the mantle as a "Hadean matte" (O'Neill, 1991a,b) to be incorporated in the core (Wade and Wood, 2016).

In spite of the acquisition of extensive data sets of metal-silicate partitioning for a wide array of moderately to strongly siderophile elements, ranging from refractory to volatile, the modelling of the T-p-$f_{O2}$ evolutionary path of core segregation in large planets like Venus and Earth is still challenging (e.g. Walter and Cottrell, 2013). The estimated core and mantle compositions in Table 2 refer to the *current* core compositions, based on a combination of geochemical reasoning and constraints from mass distribution and density, as well as seismology for the Earth and Moon. Recent evidence presented in Section 4 indicates considerable core-mantle chemical exchange immediately after the magma ocean crystallisation, at least for the Earth (e.g. Torsvik et al., 2016; Badro et al., 2016; Hirose et al., 2017a).

### 2.3. The extreme Mercury composition

Before the acquisition of the MESSENGER spacecraft data, it was speculated that the large core fraction (67 wt%) and shallow mantle of Mercury could result from impact erosion or silicate volatilisation close to the young Sun. The high K/Th and K/U ratios measured by the gamma-ray spectrometer, however, demonstrate that Mercury is less devolatilised than Earth, Venus, and especially Vesta and the Moon (Peplowski et al., 2011; McCubbin et al., 2012). Large-scale vaporisation and loss of the outer silicate portion is therefore unlikely. The high S/Fe ratio of the crust indicates an extremely low $f_{O2}$, and Malavergne et al. (2010) and Zolotov et al. (2013) estimated ranges of 3–6 and 4.5–7.3 log units below the IW buffer, respectively. Based on the planetary mass distribution and geochemical data, Hauck et al. (2013) inferred the existence of an FeS-dominated layer at the CMB. As a consequence, three separate liquid phases: silicate, sulfide and metal, may have approached equilibrium at approximately 5.7 GPa, the estimated CMB pressure (Hauck et al., 2013), during late core segregation.

To estimate the core composition of Mercury, we utilised this information in combination with the sulfide-metal immiscibility fields in the 1 bar to 15 GPa range, shown in Fig. 3, based on Morard and Katsura (2010). The positions and orientations of the equilibrium tie lines at 4–6 GPa, reported in separate figures by Morard and Katsura (2010), agree with our estimated core composition with 15 wt% Si and 1.2 wt% S (Table 2) in equilibrium with an almost pure FeS liquid (e.g. Malavergne et al., 2014; slightly non-stoichiometric with 0.16 mol% Si and a Fe/S atomic ratio of 0.97; Fig. 3). A core composition with 15 wt % Si is also indicated by the core and mantle densities and core radius (Hauck et al., 2013; Knibbe and van Westrenen, 2018). The core and mantle compositions are also broadly consistent with 1 GPa, low-$f_{O2}$ experimental results of Malavergne et al. (2014), specifically the run products H150 and H161, which have coexisting FeS, silicate and metallic melts. To derive the Table 2 estimates, we used those run products as a starting point and put further constraints on $S^{mantle}$, $S^{core}$ and $FeO^{mantle}$ based on Fig. 4. The upper panel from Malavergne et al. (2004) is used to estimate the log $f_{O2}$ to $-4.55$ ($\Delta$IW) for 15 wt% Si in the core. The middle panel from Malavergne et al. (2014) shows the S-content in the silicate as a function of temperature at 1 GPa for two different $f_{O2}$ ranges and as a function of $f_{O2}$ at 1600–2300 K at 1 bar and 1 GPa. We estimated the S saturation level in the silicate to be about (possibly even higher than) 10 wt% at the CMB pressure of about 6 GPa and adopted that for the mantle. This gives 1.2 wt% S in the core (upper right-hand figure, middle panel). The lower panel from Wood and Kiseeva (2015) is used to estimate the $FeO^{mantle}$ concentration to 0.47 wt%. Such a value is in agreement with e.g. the Zolotov et al. (2013) estimate of 0.3–0.8 wt% FeO, based on MESSENGER spectrometry data and an inference that most of the Fe is bound in mantle and crustal sulfides. Whereas the inferred Mercury $S^{mantle}$ concentration is used to estimate the $FeO^{mantle}$ in the lower panel, we lack good constraints on the $S^{mantle}$ concentrations for the other terrestrial planets. The $FeO^{mantle}$ contents from Table 2 are marked as grey squares on the purple curve in the lower panel and would *tentatively* yield $S^{mantle}$ contents of 0.2 to 0.4 wt% for the other terrestrial planets. However, the

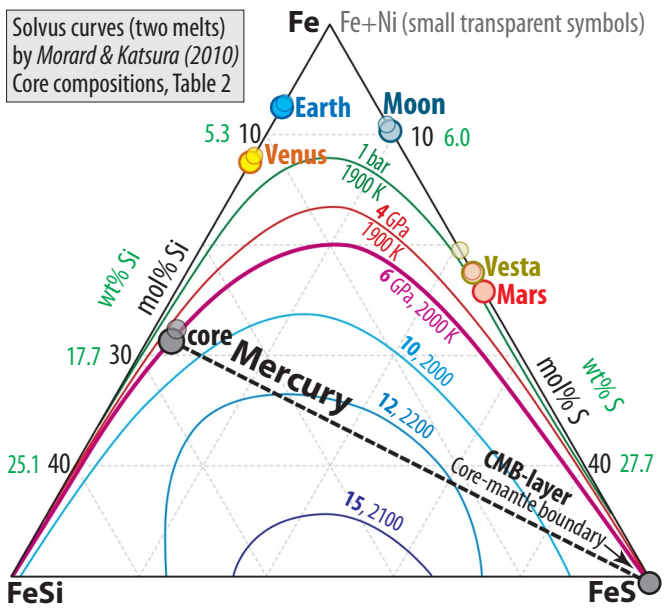


**Fig. 3.** Liquid immiscibility with solvus curves in the system Fe-Si-S at various **p** and T. The core compositions are from Table 2. The FeS-dominated CMB-layer in Mercury is an average of experiments H150 and H161 of Malavergne et al. (2014). Although it is slightly non-stoichiometric, the deviation from ideal FeS is within the quoted analytical uncertainty. The Mercury core composition is broadly constrained by the position and orientations of the 6 and 4 GPa tie lines between the metallic and FeS-dominated melts, shown in separate figures in Morard and Katsura (2010), as well as the core and mantle densities and core radius (Hauck et al., 2013; Knibbe and van Westrenen, 2018).

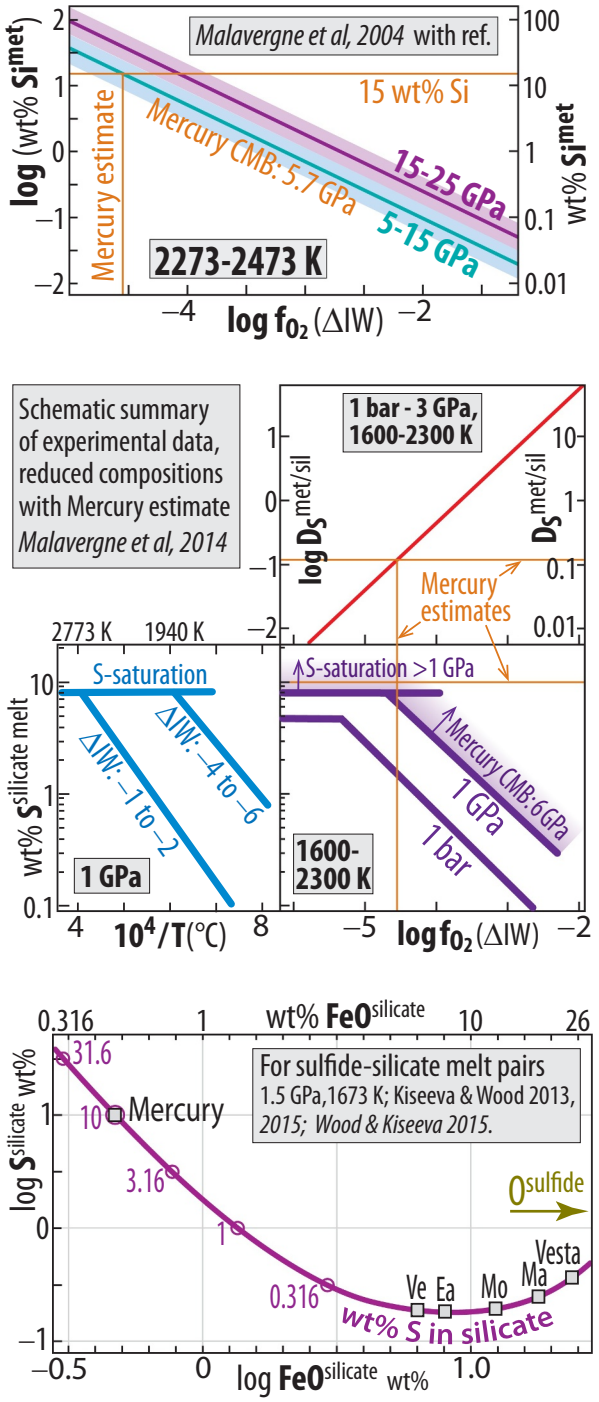


**Fig. 4.** Compositional relations applicable to the equilibrium between silicate, FeS-rich sulfide and Fe-rich metallic melts in Mercury. ΔIW: log-units relative to the iron-wüstite buffer reaction. Abbreviations: met, metal; sil, silicate; CMB: core-mantle boundary. References in the legends. The **upper panel** shows that 15 wt% $Si^{met}$ (largely from Fig. 3) corresponds to a reasonable Mercury log $f_{O2}$ of −4.6 (ΔIW). The **middle panel** shows that 8 wt% S represent silicate melt saturation at 1 GPa. From the lower right diagram (middle panel), we estimate a saturation level for $S^{silicate}$ of about 10 wt% at the Mercury CMB-conditions of 6 GPa (or slightly lower pressure). At the relevant $f_{O2}$ the partitioning coefficient $D_S^{metal/silicate}$ is 0.12, resulting in $S^{metal(core)}$ of 1.2 wt%. **Lower panel**: The estimated sulfide saturation level of $S^{silicate}$ = 10 wt% gives a $FeO^{silicate}$ concentration of 0.47 wt%, which is in agreement with inferences from spectrometric analyses by the MESSENGER spacecraft. Much of the mantle and crustal Fe is in sulfides like niningerite, and Zolotov et al. (2013) estimate that the actual FeO concentrations are within the 0.03–0.8 wt% range. The other terrestrial planets are marked in the diagram based on their $FeO^{mantle}$ contents, even if their magma oceans were not strictly S-saturated.

mantle magma oceans of those planets may not have been S-saturated, and Fig. 4 (lower panel) represents a restricted p-T range. The oxygen fugacity of −4.55 (ΔIW) estimated from the upper panel is nearly identical to the direct calculation from $FeO^{mantle}$ and $Fe^{core}$ concentrations (of −4.56, Table 2, Section 2.2).

The Mercury composition indicates accretion from very O-deficient materials, like enstatite chondrite (EC) or CB chondrites (e.g. Malavergne et al., 2014). Whereas EC materials do not have sufficiently high metallic iron content to account for the large core, the CB chondrites do. The Mg# of 96–99 for the CB pyroxenes and olivines are only slightly lower than those of the enstatite chondrites (e.g. Weisberg et al., 2001; Weisberg and Kimura, 2010). The high abundance (70–90 wt%) of Fe-dominated metal place the CB chondrites well above the $Fe^{metal+sulfide}$/Si range for enstatite chondrites and thereby outside the range of Fig. 1. Even so, the CB chondrites are unlikely building materials for Mercury because they are within the CC group in terms of the O-Cr-Ti-isotope ratios compiled by Warren (2011). A unique EC source type present only in the innermost part of the accretion disc seems a more likely alternative. Such source materials, orbiting close to the Sun in the early accretion disc, might have had higher Fe-contents than the EC parent bodies in the asteroid belt, which gives rise to the EC-material falling onto the modern Earth. The Mo- and Nd-isotopic compositions of the Earth's mantle, reported by Render et al. (2017), differ from that of the sampled chondrites and indicate that the Earth, and presumably also Mercury and Venus, have elevated proportions of S-process nuclides, reflecting distinct EC-like material close to the Sun (Section 2.1).

The partial replacement of O by S as a major anion in the "silicate" portion of Mercury must involve significant amounts of rare Mg- and Ca-dominated sulfides in the mantle and crust (e.g. Zolotov et al., 2013; Malavergne et al., 2014). Such minerals like niningerite, (Mg,Fe,Mn)S, and oldhamite, CaS, are also common in EC meteorites. The low (Mg + Fe)/(Si + Al) atomic ratio (0.73, Table 2) imply that the mantle has no olivine, but a considerable amount of quartz and coesite, in addition to the dominant orthopyroxene and minor amounts of clinopyroxene, and depending on depth: plagioclase, spinel or garnet. A primary crustal layer of magmatic graphite may be another exotic mineralogical feature. Based on the extremely low oxygen fugacity and the observation of low reflectance material covering at least 15% of the surface, Vander Kaaden and McCubbin (2015) suggested that graphite might have been a buoyant cumulate mineral during the magma ocean crystallisation. Under very reducing Mercury-like conditions with S as an additional silicate melt anion, elements which are normally lithophile, including U and Th, become more chalcophile and partition increasingly into the coexisting sulfide melt (e.g. Wood and Kiseeva, 2015; Wohlers and Wood, 2015, 2017). The FeS layer at the Mercury CMB might therefore represent a significant radioactive heat source.

### 2.4. High-T incorporation of Si, Mg and Al in planetary cores

As shown in Figs. 4 and 5, the solubility of Si in iron-dominated metal increases with decreasing oxygen fugacity and increasing temperature. The positions of the iron-wustite (IW) and silicon-silica (SS) reference reactions in a log $f_{O2}$ versus T diagram for a pressure of 20 GPa are shown in Fig. 5. The SS-reaction has a steeper slope (stronger $f_{O2}$ increase with increasing T) than the IW-reaction. A silicate melt with a Mg# of 90, corresponding to the Earth's mantle composition (green stippled line, parallel to and about 2 log-units below the IW-buffer), will be in equilibrium with an Fe-dominated alloy with 7 wt% Si (blue stippled line, parallel to the SS-reaction, about 5 log-units above the SS-buffer) at 2684 K and 20 GPa. An oxygen fugacity of about 2 log-units below the IW-reference corresponds roughly to the estimated value for Earth in Table 2. During the slow crystallisation of a basal magma ocean (BMO) in the Hadean and early Archean, the temperature of metal-silicate equilibrium near the CMB in planets like Earth and Venus is likely to have exceeded 5000 K (Labrosse et al.,

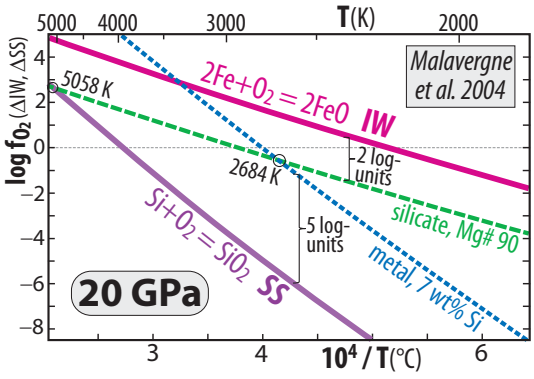


**Fig. 5.** The IW and especially the SS reference reactions rise to higher $f_{O2}$ with increasing temperature. The Earth's mantle with Mg# 90 is about 2 log-units below IW, and liquid metal with 7 wt% Si is in equilibrium with such a silicate composition at 2684 K, log $f_{O2}$ (ΔIW) of −2 and log $f_{O2}$ (ΔSS) of +5. At 5058 K the silicate with Mg# 90 has still a log $f_{O2}$ (ΔIW) of about −2, but at this high temperature it coincides with the SS buffer reaction. Combining the IW and SS reactions yields:

$SiO_2^{sil} + 2Fe^{met} = 2FeO^{sil} + Si^{met}$

This combined reaction proceeds towards the products with increasing temperature (e.g. Malavergne et al., 2004; Tsuno et al., 2013; Fischer et al., 2016; Hernlund, 2016; Laneuville et al., 2018), facilitating high Si-content at high $f_{O2}$ in in a hot protocore. Planetary cooling, however, will lead to oversaturation of Si and undersaturation of O in the core.

2007; Laneuville et al., 2018). Although Fig. 5 represents an unrealistically low pressure for Earth and Venus BMOs, it illustrates that high core concentrations of Si would be possible at high temperature and high $f_{O2}$, and that the SS reaction reaches 2 log-units below the IW reference at 5058 K and 20 GPa. The phase relations presented by Hirose et al. (2017a) indicate that cooling of Earth's protocore, in equilibrium with the BMO at about 136 GPa, might cause crystallisation and floatation of silica in the core and into the basal magma ocean where the crystals would dissolve (Section 4).

Minor amounts of MgO, $Al_2O_3$ and other oxides, commonly regarded as non-siderophile, might also dissolve in the core if the Earth's basal magma ocean and outermost protocore reached temperatures of about 5600 K during a late core segregation stage (Laneuville et al., 2018). The liquid miscibility ranges in the systems Fe-MgO and Fe-$AlO_{1.5}$ determined experimentally by Badro et al. (2016) are reproduced in Fig. 6. Their model, based on experimental data covering the 35–74 GPa range, does not indicate any pressure effect on the solvus location. The $AlO_{1.5}$ solubility is less than that of MgO below 8100 K, where the solubility curves intersect. At an estimated outer protocore temperature of 5600 K (Laneuville et al., 2018), the solubilities expressed as wt% Al and Mg are 1.3 and 2.7, respectively. At a current median temperature of the outer core of approximately 4750 K (representing the 4000–5500 K range), the solubilities are 0.45 and 1.3 wt% Al and Mg, respectively. If the solubility limits are independent of pressure (Badro et al., 2016), the exsolution of MgO and $AlO_{1.5}$ would be confined to lowest temperatures in the uppermost part of the core. This contrasts with the results of Wahl and Militzer (2015), based on thermodynamic integration of ab initio molecular dynamics simulations, indicating a positive pressure effect on the temperatures of the Fe-MgO solvus closure of 4089, 6767, 9365 K at 1 bar, 100 GPa and 400 GPa, respectively. In Section 4.2 we review the $SiO_2$ solubility in Fe-dominated metallic liquid (system Fe-Si-O), which also decreases with increasing pressure and decreasing temperature (Hirose et al., 2017a).

### 2.5. Accretionary material and oxygen fugacity, Mercury-Venus-Earth

Insights into the initial composition and earliest evolution of the Earth's core through core-mantle chemical exchange rely on general knowledge of the provenance of the terrestrial planets and the chemical zonation and temporal evolution of the accretion disc. An apparently straightforward explanation for the gradient in bulk planetary $f_{O2}$ from Mercury via Venus to Earth would be that the proportion of oxidised material increases during the prolonged accretion of Earth (and presumably Venus) due to an earlier accretionary disc perturbation by migration of the gas giants (Walsh et al., 2011; Kruijer et al., 2017). The end of the initial separation between the NC and CC material groups by a proto-Jupiter orbital barrier (Warren, 2011; Kruijer et al., 2017) would open for influx of CC and cometary material into the inner Solar system. The accretion model of Rubie et al. (2015b) yields increasing proportions of oxidised material during the later accretionary stages. Recent isotope geochemical constraints, reviewed and modelled by e.g. Dauphas (2017), predict a considerable proportion of CC-material along with EC-type material during the initial 60% accretion of the Earth. Thereafter, and especially during the late veneer stage (about 0.5%), the EC-material must be dominant, implying delivery of highly reduced materials near the end of the accretion. The latter constraint is imposed mainly by the isotopic composition of the highly siderophile element Ru in the mantle. The Badro et al. (2015) accretion and core evolution model supports the scenario with relatively early addition of oxidised material, followed by reduced $f_{O2}$ during late accretion and core segregation. Because the initial 60% accretion period for the Earth presumably extends considerably beyond the time of disc perturbation (Walsh et al., 2011; Kruijer et al., 2017), the model of Dauphas (2017) predicting relatively early influx of oxidised CC-material to the Earth, may be in full agreement with the "Grand Tack" scenario. Although Dauphas (2017) modelled the non EC-contribution to the Earth during the initial 60% accretionary stage as CC-group materials, it seems likely that some of this might also be OC-material, which is part of the NC group of Warren (2011) and Kruijer et al. (2017). A relatively short episode of delivery of the oxidised material within the initial 60% Earth accretion period may be related to the limited time frame for the gas giant migration and disc perturbation. The observation that the dominant EC-like material which contributed to the Earth was isotopically distinct, i.e. with higher proportions of s-process Mo-isotopes than the EC and OC meteorites derived from the asteroid belt, indicates the presence of reduced material which was unique to inner Solar system feeding zones (Render et al., 2017).

At first sight, the dominance of EC-type material for Earth and Venus may seem at odds with their significantly higher bulk planetary $f_{O2}$ compared to that of Mercury. Although the Dauphas (2017) model allows for as much as 50% non-EC material during the initial 60% accretion stage, the relatively high $FeO^{mantle}$ content for the large planets Venus and Earth is also facilitated by high temperature of core segregation, related to extensive heat generated from gravitational

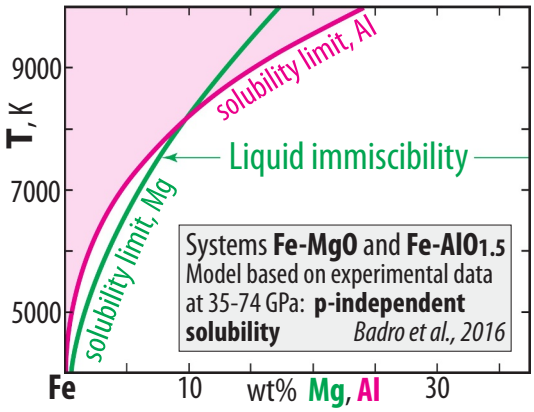


**Fig. 6.** Solubility limits of MgO and $AlO_{1.5}$ in Fe-dominated metallic liquid. The model based on experimental data in the 35–74 GPa range indicates that the solubilities of MgO and $AlO_{1.5}$ are pressure insensitive.

(potential) energy conversion (e.g. Rubie et al., 2015a). As shown in Fig. 5, elevated temperatures enable high Si concentration in the core combined with high $f_{O2}$ and $FeO^{mantle}$. During the subsequent core cooling, the reverse migration of Si, as $SiO_2$ crystals, out of the core, accompanied by FeO and $Fe_2O_3$ dissolution into the core become important processes (Section 4).

### 2.6. S-rich cores: Mars and planetesimals

The liquidus phase relations of the binary systems Fe-Si, Fe-C, Fe-S and Fe-O, covering wide ranges of pressure, are shown in Supplementary Figs. S1–S4. The relations guide the light element composition of the cores and the solids formed during possible core crystallisation. Although we will refrain from detailed discussions of these relations, it can be noted that the eutectic points closest to Fe move towards Fe with increasing pressure for these binary systems, except for the Fe-O system.

The core compositions of the iron meteorite parent bodies, as well as Vesta and Mars, are close to the Fe-S compositional join. As shown in Table 2 and Fig. 2, the core-mantle separation and partial equilibration within Vesta and Mars occurred at relatively high oxygen fugacities. The magmatic Fe-meteorite parent bodies might have experienced even higher oxygen fugacities of 0.95 log-units below the IW buffer (Bonnand and Halliday, 2018). At such conditions the incipient melting triggered by $^{26}$Al-decay in small planetesimals (diameters of 500 km, Vesta-size, to about 60 km diameter, e.g. Yoshino et al., 2003, Walter and Trønnes, 2004; Kruijer et al., 2014) would start at the binary Fe-S eutectic or the ternary Fe-S-O eutectic, which are both close to FeS in composition at 1 bar (Figs. 7 and 8). Iron sulfide melt fractions of only about 5 wt% might be able to segregate inwards by percolative flow (Yoshino et al., 2003). Further melting would produce progressively more Fe-rich melts, which would segregate and mix with the eutectic FeS-rich melt. Even if there is no miscibility gap along the Fe-FeS join, protracted crystallisation of Fe in the cores of magmatic Fe-meteorite parent bodies would enrich the residual melts in S and P, which would bring them into the liquid immiscibility field in the system Fe-P-S (Fig. 9, Jones and Drake, 1983; Ulff-Møller, 1998; Chabot and Drake, 2000; Haack and McCoy, 2003).

A very large miscibility gap covers the entire Fe-FeO join and most of the Fe-FeO-FeS compositional space at 1 bar to 6 GPa (Fig. 8). Oxygen is therefore an unlikely core component in planetary bodies with a CMB pressure below 6 GPa. The 1 bar gap extends to > 2773 K over most of the Fe-FeO join, with a solvus crest of > 3000 K (e.g. Kato and Ringwood, 1989). At 3 GPa (small inset part in the upper 1 bar panel) and 6 GPa, the eutectic moves close to the Fe-FeS join at 40–35 mol% (28-24 wt%) S. These phase relations imply that S, if available in the accreted material, is the main light core component in planetesimals in a relatively oxidised environment. In the pressure range from 1 bar to 6 GPa, the high melting temperature of FeO with a minor binary Fe-FeO eutectic at only 0.3 wt% O (at 6 GPa) and the wide and thermally extensive liquid immiscibility field along the Fe-FeO join (Fig. 8; Kato and Ringwood, 1989) preclude a significant O-component in such cores. At 16 GPa the binary Fe-FeO eutectic located at about 2 wt% O and 1973 K and a reduced liquid immiscibility field, would allow slightly more O in the cores. The eutectic applicable to the initial melting, however, is clearly the ternary eutectic close to the Fe-FeS join at 3–16 GPa. Fig. 8 also shows that the effect of Ni (with a Fe/Ni-ratio of 9) at 6–16 GPa is to reduce the ternary and binary Fe-FeS eutectic temperatures and the liquid immiscibility fields. With a CMB-pressure of about 20 GPa (Fig. 2) the Martian core might therefore have higher O-content (e.g. Rubie et al., 2004) than that of Table 2, which is the estimated ternary eutectic composition at 20 GPa. That estimate is also within the 11–16 wt% S range of Dreibus and Wänke (1985), Lodders and Fegley (1997), Sanloup et al. (1999) and Stewart et al. (2007). Our Vesta core estimate is the H-chondritic model composition of Toplis et al. (2013). An alternative ternary eutectic core estimate at 0.1 GPa (Fig. 8), interpolated between 1 bar and 3 GPa and assuming a Fe/Ni-ratio of 9, yields 51, 6, 37 and 6 wt% Fe, Ni, S and O, respectively (only the Ni-free Fe-FeS-FeO phase relations are available at 1 bar). A core composition with such high concentrations of S and O may be unrealistic due to the bulk S content of Vesta. Initially high $S^{core}$ and $O^{core}$ concentrations might have been reduced by later core addition of relatively pure Fe-Ni metal.

## 3. Early planetary melting and crystallisation of silicate magma oceans

Here we review the melting relations of peridotite at low to moderate pressures, relevant to silicate mantle melting and crystallisation in planetesimals like Vesta, in remnants of other differentiated parent bodies and in the shallow parts of the larger bodies, including the Moon. The melting relations, mineral-melt Fe/Mg partitioning and mineral-melt density relations at pressures up to the Earth's core-mantle boundary conditions are discussed as a basis for understanding the structure and crystallisation sequence of magma oceans. We conclude that an extensive basal magma ocean (BMO) would likely form in the largest planets Earth and Venus, and that such a thermally insulated BMO might have had a life-time of 1–2 Gy, crystallising slowly from the top towards the CMB. Such a life-time seems reasonable because the peridotite solidus of about 4200 K at 136 GPa (Fiquet et al., 2010; Andrault et al., 2011) is only about 200 K above the present CMB temperature and because the secular cooling of the mantle since 2.5–3 Ga is estimated to 150–200 K (Herzberg et al., 2010; Jaupart et al., 2015; Ganne and Feng, 2017). A protracted BMO crystallisation period would facilitate extensive core-BMO chemical exchange as discussed in Section 4.

### 3.1. Heat sources

The accretion of the terrestrial planets was accompanied by global pervasive melting resulting from three major heat sources. At the early planetesimal stage the radioactive decay of $^{26}$Al ($t_h$: 0.7 My) was the initiating heat source. A requirement for sufficient internal temperature rise to cause melting and core segregation is that the planetesimals grew to a minimum (critical) size within a maximum period of time, about 1–3 My. Walter and Trønnes (2004) performed thermal modelling with "canonical" $^{26}Al/^{27}Al$ initial ratio of $5 * 10^{-5}$ at 4567 My ($t_0$) and a 60 km diameter planetesimal established at $t_0$ and $t_0$ + 1 My, respectively. This produced a temperature rise to the 1 bar Fe-FeS-FeO eutectic of about 1180 K (Fig. 8) in time periods of 0.12 and 0.91 My, to the 1 bar peridotite solidus of about 1373 K (Herzberg and O'Hara, 2002) in 0.16 and 1.27 My and to 1765 K (i.e. 200 K below the peridotite liquidus) in 0.26 and 3.0 My, respectively. The latter temperature is 67% up through the melting range from the solidus and would be sufficient to create a large melt fraction and a magma ocean. If the

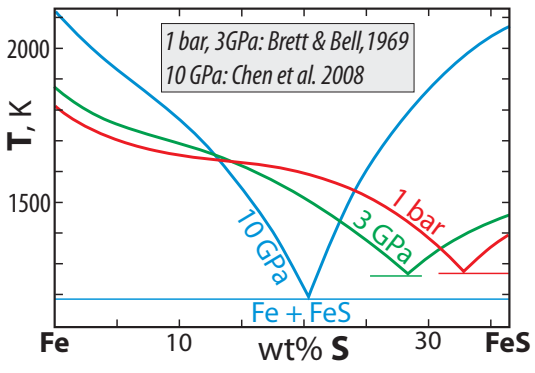


**Fig. 7.** Liquidus phase relations at 1 bar, 3 GPa and 10 GPa in the Fe-rich part of the system Fe-S.

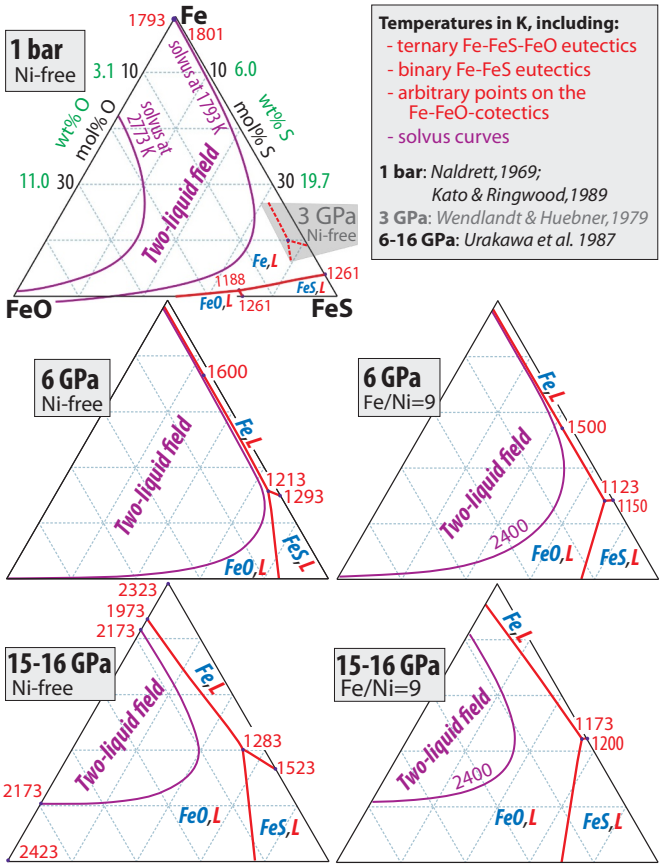


**Fig. 8.** Liquidus and immiscibility fields in the system Fe-O-S at 1 bar, 6 GPa and 15–16 GPa. The 3 GPa liquidus boundaries (stippled) close to the Fe-FeS-FeO eutectic is shown in a small grey inset field in the 1 bar diagram. The 1 bar phase relations on the Fe-FeO join near the Fe corner involves a "eutectic" composition involving solid Fe and a coexisting Fe-rich liquid with only 0.17 wt % O (0.6 mol% FeO) at the solvus at 1793 K (see Kato and Ringwood, 1989). In the two diagrams on the right side the top corners represent an FeNi-alloy with an Fe/Ni ratio of 9.

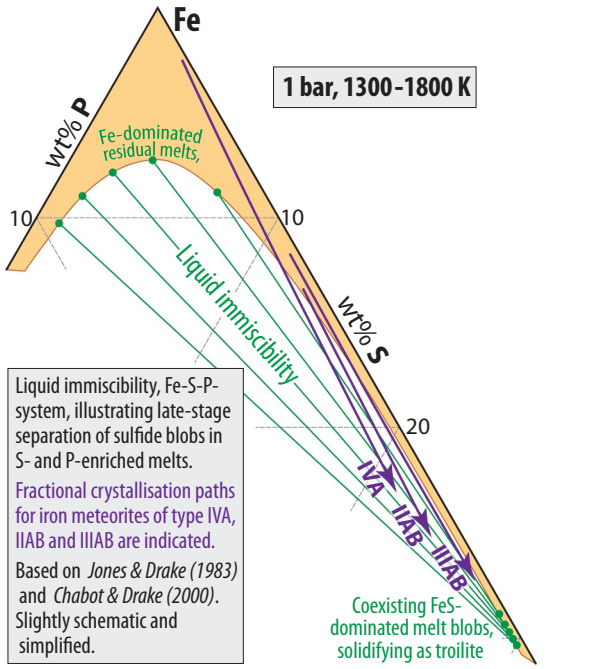


**Fig. 9.** Liquid immiscibility in the system Fe-P-S, illustrating the unmixing of FeS-blobs (solidifying as troilite) during Fe-crystallisation in iron meteorite parent body cores. The average P contents of the main iron meteorite groups are in the 0.1–2 wt% range (Mittlefehldt et al., 1998) and Fe-crystallisation and sulfide melt unmixing may result in Fe-rich residual melts with 2–5 wt% P.

accretion of such a planetesimal (60 km) occurred later than about 1 My after $t_0$, a silicate magma ocean would not be generated. A larger planetesimal could form later and still be able to melt extensively. The second major heat source is the exothermic process of metal and sulfide segregation to form the core. The inward movement of high-density material would convert potential energy to heat (e.g. Rubie et al., 2015a), contributing to the heating and melting of the silicate portion, beyond the period of intense $^{26}$Al-decay. The third major heat source, important during the gravitational runaway growth following the planetesimal stage and during the giant impact stage, is collisional energy, i.e. the conversion of kinetic energy to heat (e.g. Rubie et al., 2015a). Additional tidal (frictional) heat evolution might have been significant for the Earth-Moon system shortly after the Theia-Earth collision. The rotational energy associated with higher Earth rotation rate has largely been dissipated by the Earth-Moon tidal heat evolution, increasing the Earth-Moon orbital distance and reducing the lunar orbital speed.

### 3.2. Peridotite melting relations at low pressure

The melting phase relations involving peridotitic and basaltic model compositions at 1 bar and 1–1.5 GPa pressure are shown in Figs. 10 and 11. The 1 bar diagrams illustrate the silicate melting and magma ocean crystallisation in small planetesimals. Even in a larger planetesimal like Vesta with a CMB pressure of about 0.1 GPa, the 1 bar relations are representative for a major proportion of the mantle. The low pressure crystallisation sequence of a peridotitic magma ocean will be olivine (ol), followed by orthopyroxene (opx), and then by plagioclase (pl) and clinopyroxene (cpx). That sequence also applies to the lunar magma ocean.

The deep crust and uppermost mantle of Vesta have been sampled by intrusive cumulate-type eucrites (basaltic compositions) and diogenites (opx-dominated cumulates) which are exposed within the Rhea Silvia and Venenia crater regions of the southern hemisphere (Russell et al., 2012; De Sanctis et al., 2012; McSween et al., 2013). The abundance of opx-cumulates, also present in the polymict howardite breccias, contrasts with low-pressure mafic and ultramafic cumulate sequences on Earth, which are rarely dominated by opx. Insights into these liquidus phase relations are provided by Figs. 10 and 11. The voluminous mid-ocean ridge tholeiites, as well as many other tholeiites, e.g. in flood basalt provinces, are generated in equilibrium with spinel lherzolite minerals in the uppermost mantle, e.g. at 1.5 GPa (Fig. 10). The melt, marked as BE (basalt-Earth) in the lower figure panel, is in equilibrium with ol, opx, cpx and spinel at 1.5 GPa, where the liquidus phase volumes of ol and pl are reduced relative to those of spinel and cpx. When such a melt migrates to shallow magma chambers, mostly near the Moho, the BE melt composition is well inside the expanded liquidus volume of ol, illustrated by the 1 bar diagram. The crystallisation sequence will then be ol, followed by ol + pl and then ol + pl + cpx, indicated by the green, blue and purple arrows in the 1 bar diagram.

Partial melting in the low-pressure mantle of Vesta, however, will produce the more silica-rich composition BV (basalt-Vesta; Fig. 10, 1 bar diagram; Fig. 11) in equilibrium with ol, opx, cpx and pl. Even if that melt may also migrate towards the surface, it will not experience a significant change of pressure and liquidus phase relations. A simple analysis of the phase relations in Fig. 11 illustrates the dominance of opx cumulates (diogenites) on Vesta. Extensive melting of the mantle will produce mixed magmas from the ternary ol-opx-pl peritectic at 1260 °C and the binary ol-opx peritectic at 1570 °C, following elimination of pl. Crystal fractionation of such magma mixes, illustrated by

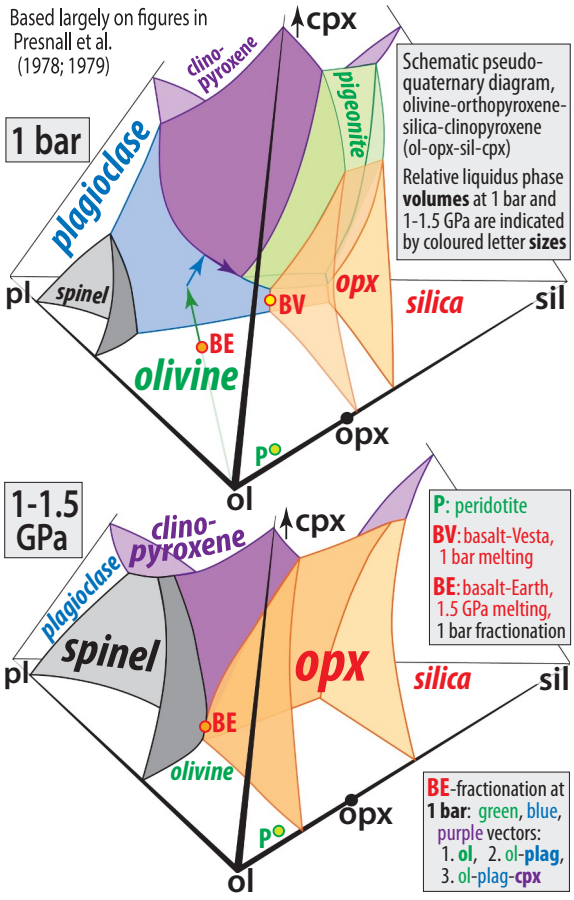


**Fig. 10.** Schematic drawings of the liquidus phase volumes (separated by coloured walls/surfaces) in the pseudo-quaternary system olivine-silica-clinopyroxene-plagioclase at 1 bar and 1–1.5 GPa. The phase volumes (between the cotectic walls) include the labelled liquidus mineral, in addition to melt.

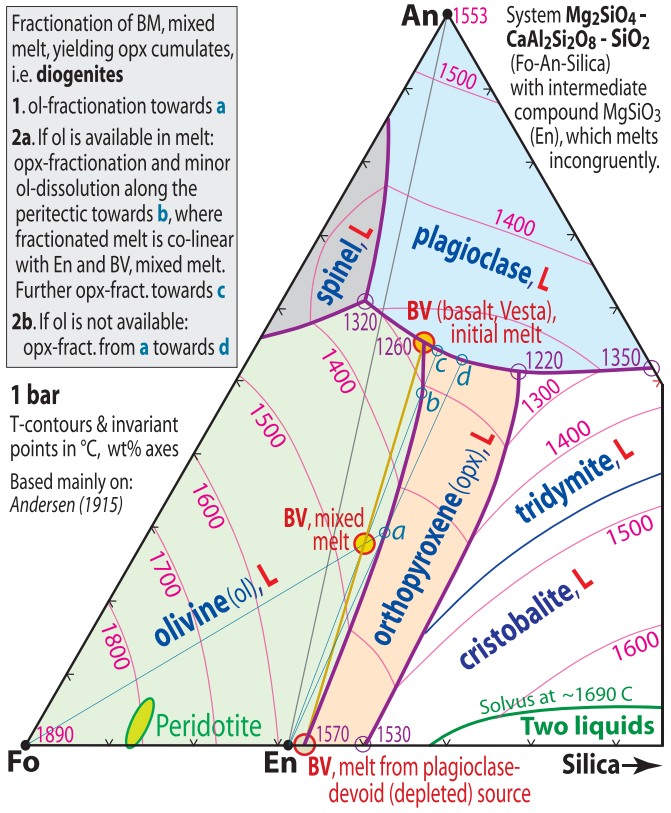


**Fig. 11.** Liquidus phase fields with peritectic and cotectic boundaries and invariant points. Contours and invariant points are marked with temperatures in °C. See text for further explanations.

the "BV, mixed melt" composition, will involve minor olivine subtraction before the melt composition reaches the nearby peritectic curve at "a".

The further crystallisation depends on whether ol crystals are either available for dissolution in the melt or unavailable. If ol is available, the melt will evolve along the peritectic curve towards "b", crystallising opx and dissolving ol. In a closed model system the melt composition at "b" is co-linear with the enstatite (En) and bulk ("BV, mixed melt") compositions. Further fractionation will therefore involve only opx subtraction towards "c", from where opx + pl crystallise. In an open system where the early olivine crystals are physically prevented from equilibrium with the melt, the fractionation from "a" would involve only opx, causing the melt to move along an opx fractionation vector towards "d". The simplified phase relations illustrated in Figs. 10–11 demonstrate how low-pressure melting and crystallisation in planetesimals may yield opx-dominated cumulates (e.g. diogenites at Vesta), whereas melting at moderate to high pressure in larger planets, followed by fractionation in shallow magma reservoirs, will mostly produce dunitic, troctolitic and gabbroic cumulates.

### 3.3. Peridotite melting relations at high pressure

The p-T diagram in Fig. 12, displaying the approximate liquidus phase relations of peridotite in the 2–36 GPa pressure range, illustrates the changes of liquidus phases through the upper mantle, transition zone and the upper part of the lower mantle to a depth of about 930 km (e.g. Zhang and Herzberg, 1994; Walter, 1998; Herzberg and O'Hara, 2002; Trønnes and Frost, 2002; Ito et al., 2004). Olivine is the first liquidus phase throughout the upper mantle and is replaced by garnet (ga) at pressures above about 14 GPa. In the uppermost mantle, opx and cpx are the second and third crystallising phases, respectively. The aluminous phases pl and spinel are stable up to the solidus at about 1 and 2.5 GPa, respectively, but melt away at minor T-increments above the solidus (e.g. Herzberg and O'Hara, 2002; not shown in Fig. 12). From about 2.5 GPa, ga appears at and above the solidus and its proportion and thermal stability within the melting range increases greatly towards 14 GPa, where it overtakes ol as the first liquidus phase. The

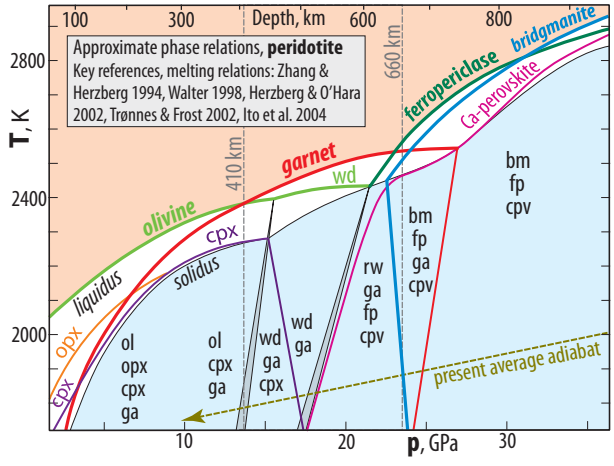


**Fig. 12.** Liquidus phase relations of pyrolitic peridotite. Mineral abbreviations: ol, olivine; cpx, clinopyroxene; opx, orthopyroxene; plag, plagioclase; ilm, ilmenite; ga, garnet; wd, wadsleyite; rw, ringwoodite; fp, ferropericlase; cpv, Ca-perovskite, bm, bridgmanite. A tiny suprasolidus field of the anhydrous-B phase (Zhang and Herzberg, 1994) is omitted for simplicity and clarity.

proportion of the majorite component from pyroxene dissolution into ga increases greatly from 7 to 14 GPa. The two separate pyroxenes also merge into one cpx-structured phase in this pressure range. The transition zone subsolidus mineral assemblage is about 40% ga and 60% wadsleyite (wd) or ringwoodite (rw), and wd is the second mineral to crystallise after ga from a cooling peridotite magma. Ca-perovskite (cpv) appears as a minor subsolidus phase at about 19 GPa along the present geotherm and reaches the solidus in the lowermost transition zone and uppermost lower mantle (Fig. 12). Ferropericlase (fp) appears in the melting range with ga at 21–22 GPa and becomes the first liquidus phase in the 22–31 GPa range, being replaced by bridgmanite (bm) above 31 GPa (Ito et al., 2004). Although cpv remains near the solidus in the uppermost part of the lower mantle, its thermal stability increases with pressure, and it is the first liquidus phase in basaltic compositions throughout the lower mantle pressure range (Hirose and Fei, 2002; Andrault et al., 2014; Pradhan et al., 2015; Tateno et al., 2018).

LH-DAC melting experiments on natural peridotite and basalt compositions, using TEM and field-emission EMPA of sectioned run products, are diagnostic in terms of the crystallisation sequence. These studies agree that the crystallisation sequence of natural peridotite is bm, followed by fp and then cpv, at pressures above 30–40 GPa (Fiquet et al., 2010; Andrault et al., 2011; Tateno et al., 2014; Nomura et al., 2014). Experiments in the 143–179 GPa range also demonstrate that post-bridgmanite (pbm) is the first liquidus phase, followed by fp at lower temperatures (Nomura et al., 2011; Tateno et al., 2014). For basaltic melt compositions in the lower mantle pressure regime, the crystallisation sequence is cpv, followed by stishovite or modified stishovite (β-stishovite, $CaCl_2$-structured) and then bm (Andrault et al., 2014; Pradhan et al., 2015; Tateno et al., 2018). At pressures exceeding 108 and 123 GPa, the crystallisation sequence is cpv-bm-silica and cpv-pbm-silica, respectively (Tateno et al., 2018). Seifertite might replace β-stishovite ($CaCl_2$-structured silica) as the silica phase near the solidus in the lowermost mantle. Based on multianvil experiments, Hirose and Fei (2002) found that cpv and stishovite crystallise almost simultaneously at 23–24 GPa, but that cpv is clearly the first liquidus phase, preceding stishovite at slightly higher pressures of 25–28 GPa.

### 3.4. Melting relations in the CaO-MgO-$SiO_2$ systems, 24–136 GPa

The acquisition of experimental and ab initio computational data on the melting relations in the system CaO-MgO-$SiO_2$ (CMS) is a useful approach to develop a more comprehensive thermodynamic model applicable to melting and crystallisation in the pressure regime of the Earth's lower mantle. This ternary system includes the main end members for the three lower mantle peridotite phases, bm, fp and cpv. In a basaltic mineral assemblage the CMS-phases bm, cpv and a silica mineral comprise about 75 mol%, even if the bm composition may have about 20, 10 and 7 mol% of the $FeAlO_3$, $FeSiO_3$ and $Al_2O_3$ components, respectively.

Based on multianvil experiments to establish the melting relations in the MS system at 16–26 GPa, Liebske and Frost (2012) developed a thermodynamic model, using it to predict the pc-bm eutectic melt composition through the lower mantle pressure range. The observed MgO content of eutectic melts, including the ol-enstatite and wd-majorite eutectics, increases from 52 to 57 mol% in in the 4 to 26 GPa range, and the model predicts a further rise to 60 mol% MgO at 80 GPa, followed by nearly constant composition in the 80–136 GPa range. The pc-bm eutectic (pc: periclase) in the MS-system is therefore slightly more silicious and magnesian than peridotite compositions at 24 and 136 GPa, respectively (Fig. 13, upper panel). A compositional crossover between bulk peridotite and the predicted pc-bm eutectic with 58 mol% MgO (for the MS-system) at 30–40 GPa implies that partial melts of

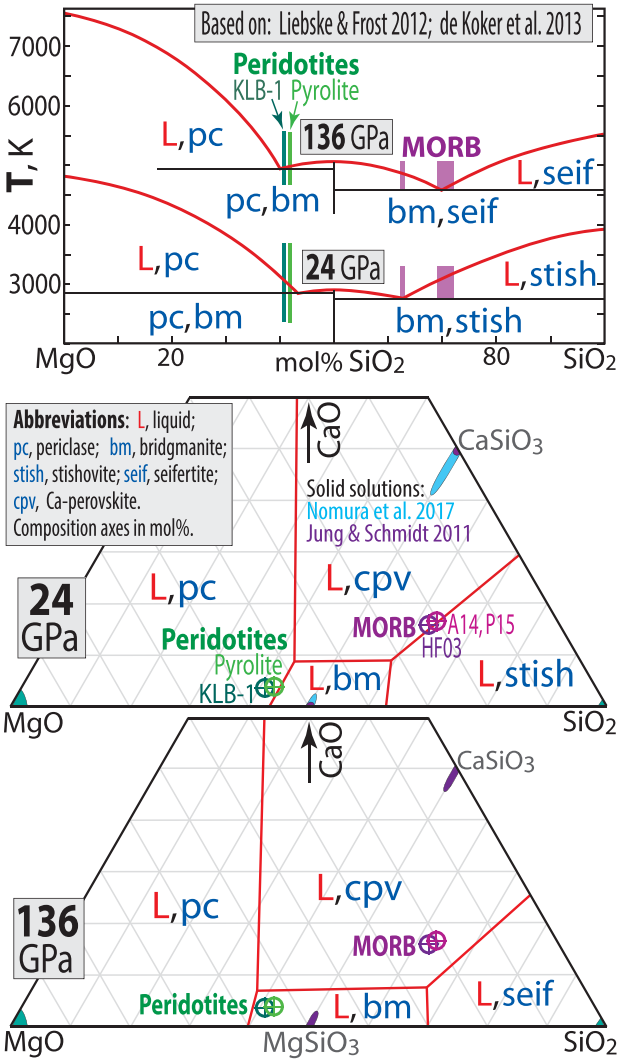


**Fig. 13. Top**: Liquidus phase relations in the system MgO-$SiO_2$ based mainly on de Koker et al. (2013), with the pc-bm-eutectic composition at 24 GPa adjusted to the Liebske and Frost (2012) result (see text). **Bottom**: Inferred liquidus phase relations in the system CMS (CaO-MgO-$SiO_2$). The solidus mineral compositional ranges are shown as blue fields. The binary MS-eutectics are transferred from the upper panel and the $MgSiO_3$-$CaSiO_3$ join at 24 GPa is based on Nomura et al. (2017). The more limited solid solution on the $MgSiO_3$-$CaSiO_3$ join from Jung and Schmidt (2011) is also indicated (dark blue). Abbreviations for the basaltic composition (MORB) references: HF03, Hirose and Fei (2003); A-2014: Andrault et al. (2014); P-2015, Pradhan et al. (2015). The MORB ranges of the binary diagram cover those three compositions. To display the natural peridotite and basalt compositions in a meaningful way we merged cations (or oxides). Cation% is equivalent to oxide% when using one-cation oxides (e.g. CaO, $AlO_{1.5}$ and $NaO_{0.5}$). In the binary diagrams we show the compositions as Si versus Mg+Fe, as well as Si+Al versus the sum of the other cations. For peridotites the difference is minor, and the dark and light green bars are slightly wider than the range. For the MORB compositions, however, the wide bar at high "$SiO_2$" represents the Si versus Mg+Fe range for the three samples, whereas the narrow bar at low "$SiO_2$" represent the same sample range for Si+Al versus the sum of other cations. Because the MORB compositions include as much as 16 mol% Ca+Na+K and fall within the liquidus field of cpv in the system CaO-MgO-$SiO_2$, their positions in the binary diagram are somewhat irrelevant, but they are included for completeness. In the ternary diagrams the peridotite and basalt compositions are calculated by assuming that mol% Ca, Mg and Si are represented by Ca+Na+K, Mg+Fe+Mn+Ni+Cr+Ti and Si+Al, respectively.

peridotite will have a slightly higher (Mg + Fe)/Si ratio than bulk compositions and solid residues in most of the Earth's lower mantle. The ab initio theoretical study of de Koker et al. (2013) determined the positions of the pc-bm and bm-silica eutectics in the MS system and obtained pc-bm eutectic compositions very similar to those of Liebske and Frost (2012). The experimental LH-DAC results of Ohnishi et al. (2017) are also in general agreement with Liebske and Frost (2012) and de Koker et al. (2013).

Although the difference between the pc-bm eutectic composition of de Koker et al. (2013) and Liebske and Frost (2012) is very small for the 136 GPa eutectic, Liebske and Frost (2012) determined a composition of 43.2 mol% $SiO_2$, versus 40.6 mol% in de Koker et al., for the 24 GPa eutectic. The pc-bm eutectics in Fig. 13 are adjusted to the Liebske and Frost (2012) results for two reasons. The multianvil experiments at 24 and 26 GPa establish the position of that eutectic, and by using the 24 GPa eutectic of de Koker et al. (2013), the pyrolite composition, in particular, would be inside the liquidus field of bm, which is clearly not the case at 24 GPa (Fig. 12). The cotectic boundaries in our predicted CMS system diagrams at 24 and 136 GPa, shown in the two lower panels of Fig. 13, are based on the MS system eutectics in the upper panel and adjusted to the transposed compositions of the two peridotite compositions (pyrolite and a slightly melt-depleted KLB-1 composition) and the mid-ocean ridge basalt (MORB) compositions used in the melting experiments of Hirose and Fei (2002), Andrault et al. (2014) and Pradhan et al. (2015). The bm-cpv cotectic at 24 GPa is also constrained by the Nomura et al. (2017) results for the $MgSiO_3$-$CaSiO_3$ join. As described in Section 3.3, the peridotites fall within the liquidus fields of fp and bm at 24 and 136 GPa, respectively. At 24 GPa the basaltic compositions of Hirose and Fei (2002) is close to co-saturation of the primary liquidus mineral, cpv, with stishovite. At the higher pressures of 58 and 101 GPa, however, the TEM-images of the sectioned run products of Pradhan et al. (2015) demonstrate a clear and consistent crystallisation sequence of cpv, followed by stishovite or β-stishovite and then bm, down the T-gradient.

### 3.5. Mineral-melt density relations and Fe/Mg-partitioning, 24–136 GPa

As shown in Fig. 13, the Mg/Si ratios of bulk peridotites and their partial melts are similar throughout the lower mantle (LM). This is in contrast to the upper mantle and transition zone, where basaltic, picritic and komatiitic melts from peridotite have strongly to slightly reduced Mg/Si ratios relative to bulk peridotites. In the systems MS-FeO and CMS-FeO the (Mg + Fe)/Si ratio in melts and residues will vary approximately as the Mg/Si ratio in the system MS. Further constraints on the pc-bm-cpv and bm-silica-cpv eutectics in the system CMS by LH-DAC experiments and first principles atomistic computations are still needed.

The solid-melt density relations are of fundamental importance for planetary differentiation and magmatic processes in the widest sense. At low pressure, melts are generally more voluminous than solids of comparable or identical composition. A remarkable anomaly is the unary system $H_2O$ at 1 bar, where ice is less dense than water due to the charge-polarised nature of the $H_2O$-molecule. Because melts are generally more compressible than solids, they might ultimately densify to overcome the density of the coexisting (residual) solid. Solids, on the other hand, tend to undergo densifying phase transitions. The wide pressure range of the peridotite minerals bm, fp and cpv through the Earth's lower mantle above the D″-zone could, in principle, be conducive to a melt-solid density crossover. The issue has recently been addressed for Fe-free systems by e.g. Stixrude and Karki (2005), Stixrude et al. (2009), Murakami and Bass (2011), Ghosh et al. (2014) and Baron et al. (2017). Petitgirard et al. (2015) measured the density of $MgSiO_3$ bm and glass by an X-ray absorption method in the DAC, and Ghosh and Karki (2016) conducted ab initio molecular dynamics calculations to determine the density of pc and a range of fp and melt compositions in the system MgO-FeO. The upper panel of Fig. 14, based on these studies, shows that in the MS system at 4000 K, bm and pc remain denser than $MgSiO_3$ and MgO melts, respectively, through the lower mantle pressure regime. However, the solid-melt density differences decrease steadily with increasing pressure, and at 136 GPa (CMB), the density differences are 1.5 and 2.9% for the bm-melt and pc-melt pairs, respectively. At 80 GPa (1860 km depth, approximately mid-LM) the corresponding differences are 2.8 and 3.6%.

Even without a solid-melt density inversion in Fe-free systems, the strong partitioning of Fe and Mg between melt and the ferromagnesian minerals, bm and fp, will induce a density crossover within the pressure range of the Earth's lower mantle. At transition zone and uppermost lower mantle pressures of 14–26 GPa, the $K_D^{min/melt}$(Fe/Mg) is 0.2–0.6, but mostly within the narrower 0.3–0.6 range for wd, ga and bm (e.g. Trønnes et al., 1992). The lower panel of Fig. 14 shows a clustering of multianvil-based $K_D^{min/melt}$(Fe/Mg) values of 0.4–0.6 for garnet, fp and bm in the 23–33 GPa range. The LH-DAC investigation by Nomura et al. (2011) on an Al-free olivine composition gave $K_D^{bm/melt}$(Fe/Mg) values of 0.2–0.3 in the 35–75 GPa range with a strong decrease to about 0.07 at 70–80 GPa. Although their suggestion that the strong $K_D$ decrease is related to an iron spin transition in the melt is disputed, the Tateno et al. (2014) study of the KLB-1 peridotite composition also gave a

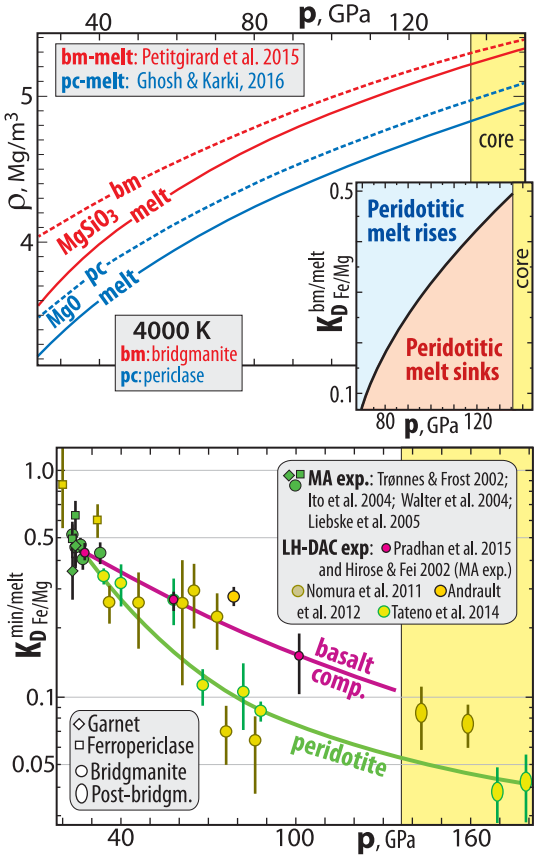


**Fig. 14. Top**: Densities for $MgSiO_3$ bridgmanite (bm) and melt and for MgO periclase (pc) and melt calculated for 4000 K in the 30–150 GPa range. Based on experimental and ab initio computational results from Petitgirard et al. (2015) and Ghosh and Karki (2016). The small inset figure shows the boundary between the fields of rising and sinking peridotite melts as a function of $K_D^{bm/melt}$(Fe/Mg) and p (Petitgirard et al., 2015). **Bottom**: Fe/Mg-partitioning between minerals and melt in peridotitic and basaltic bulk compositions at 20–180 GPa. An Al-free composition in the form of natural olivine (Mg# 89) from the KLB-1 peridotite was used for the Nomura et al. (2011) experiments. The $K_D^{bm/melt}$(Fe/Mg) value for a peridotitic bulk composition decreases to about 0.1 at 70–80 GPa. The inset panel above indicates neutral buoyancy between peridotitic melts and bridgmanite-dominated residues at 72 GPa.

strong, but more gradual, decrease from about 0.3 to about 0.1 in the 35–85 GPa range. Nomura et al. (2011) and Tateno et al. (2014) determined $K_D^{min/melt}$(Fe/Mg) values for pbm of 0.04–0.08 at 140–180 GPa. Andrault et al. (2012) measured simple $D^{bm/melt}$(Fe) coefficients based on experiments on peridotitic (chondritic) compositions with synchrotron-based XRF. One of their run products from an 80 GPa experiment, analysed by EPMA, is reproduced in Fig. 14. The $K_D$-value slightly below 0.3 is in the upper range of the Nomura et al. (2011) data in the 40–70 GPa range. The $K_D^{bm/melt}$(Fe/Mg) for basaltic bulk compositions, measured in run products from multianvil and LH-DAC experiments by Hirose and Fei (2002) and Pradhan et al. (2015), respectively, confirm a steady decrease from 0.4–0.5 to 0.1–0.2 in the 28–101 GPa range (purple curve in Fig. 14, lower panel). The basaltic composition $K_D^{bm/melt}$(Fe/Mg) values are higher than the peridotite values. This may largely be related to bm crystallisation well below the liquidus (after Ca-perovskite and silica crystallisation) in the basaltic compositions and to the fact that the Fe/Mg ratios of bm and fp consistently increase from the liquidus to the solidus, as demonstrated by multi-anvil experiments (e.g. Herzberg and Zhang, 1996; Trønnes, 2000; Trønnes and Frost, 2002). With bm crystallisation restricted to near-solidus conditions, the analysed bm crystals might inevitably be intermediate between super-solidus crystal with low Fe/Mg ratio in chemical equilibrium with the analysed melt pools and solidus crystals with high Fe/Mg, in incomplete equilibrium with the melt. We also suggest that some of the higher $K_D^{min/melt}$(Fe/Mg) values for peridotitic compositions might be affected by electron or X-ray beams that partially activated two neighbouring phases, i.e. mineral and quenched melt. Partial overlap would be difficult to eliminate completely in tiny LH-DAC cells, especially with conventional EMP (without field emission) and synchrotron-based XRF analyses, and would always distort the $K_D^{min/melt}$ values towards unity.

Petitgirard et al. (2015) evaluated the consequences of various $K_D^{bm/melt}$(Fe/Mg) values for bm-melt neutral buoyancy at various depths in the Earth's lower mantle (Fig. 14, right-hand inset panel). Based on a $K_D^{bm/melt}$(Fe/Mg) value of about 0.1 at 70–80 GPa in a peridotitic (pyrolitic) bulk composition from Tateno et al. (2014), the neutral buoyancy level in the Earth is likely at about 1700 km depth (72 GPa). As early cumulates crystallise in the middle of the lower mantle, increasing the $(Fe/Mg)^{melt}$ ratio the neutral buoyancy level might be displaced to a slightly shallower level. However, the density relations between lower mantle solid peridotite mineral assemblages and melt are also affected by the gradual spin transition in fp starting at about 70 GPa along an ambient mantle adiabat (e.g. Fei et al., 2007; Komabayashi et al., 2010; Holmström and Stixrude, 2015), as well as the complex crystal chemistry of bm. Iron is dominantly incorporated as the bm components $Fe^{3+}_{A\text{-}HS}Al_BO_3$ and $Fe^{2+}_{A\text{-}HS}Si_BO_3$, where A, B and HS indicate the large irregularly coordinated A-site, the regular octahedral B-site and high-spin state, respectively. The incorporation of considerable amounts of Al in bm (almost all the Al present in peridotites) appears to drive the redox reaction which is required for incorporation of the crystal-chemically favourable $Fe^{3+}_AAl_BO_3$-component (Section 5.4). Because subsolidus bm in peridotitic and basaltic lithologies have (Si + Al) ≥ 1 (2-cation formula basis) and commonly also Al ≥ $Fe^{total}$, the $Fe^{3+}_AFe^{3+}_BO_3$ component is generally absent, whereas the $Al_AAl_BO_3$ and $Fe^{2+}_ASi_BO_3$ components are present. Both $Fe^{3+}$ and $Fe^{2+}$ will therefore remain as A-site, high-spin Fe through the entire mantle (e.g. Potapkin et al., 2013; Lin et al., 2016; Mohn and Trønnes, 2016; Mao et al., 2017). In some experiments in which bm was synthesised from gels or glasses, the additional $Al_AFe^{3+}_{B\text{-}LS}O_3$ configuration was recorded spectroscopically (Catalli et al., 2011; Fujino et al., 2012, 2014), possibly related to metastable trapping of B-site, low-spin ferric iron (Mohn and Trønnes, 2016). This may also explain the increasing $K_D^{bm/fp}$(Fe/Mg) values at pressures exceeding about 100 GPa (Sinmyo and Hirose, 2013; Piet et al., 2016).

A few studies of relevant Al-bearing peridotitic and basaltic model compositions include analyses of ferric and ferrous iron in bm. Nakajima et al. (2012) parameterised the available data to yield an equation for $Fe^{3+}$ as a function of Al and $Fe^{total}$, making it possible to estimate the $Fe^{3+}$ content in datasets with poor or lacking $Fe^{3+}$ determinations. In peridotitic bm the $Fe^{3+}/Fe^{total}$ ratios are 40–60% for Al and $Fe^{total}$ cation contents of 4–10 and 9–10 cations, respectively, for 200 cation formulas. The maximum $Fe^{3+}/Fe^{total}$ ratio in basaltic bm with about 36 Al-cations and 25 Fe-cations may be about 70%. Prescher et al. (2014), who performed experiments on a peridotitic mineral assemblage synthesised from an oxide mix in a multianvil press at 25 GPa, recorded a rise in the $FeSiO_3$-component (from 4.8 to 6.4 mol%) and decrease in the $FeAlO_3$-component (from 4.8 to 2.9%) in bm in the 80–100 GPa range, without any significant change in the $K_D^{bm/fp}(Fe^{total}/Mg)$ of about 0.5. A decreasing $Fe^{3+}/Fe^{total}$ ratio in bm might be related to the reaction:

$$2\ FeAlO_3^{bm} + Fe^{metal\ alloy} = Al_2O_3^{bm} + 3\ FeO^{fp}$$

combined with Fe-Mg exchange between fp and bm:

$$FeO^{fp} + MgSiO_3^{bm} = MgO^{fp} + FeSiO_3^{bm}$$

Although there is some uncertainty regarding possible variations in the $K_D^{bm/fp}(Fe^{total}/Mg)$ value and $Fe^{3+}/Fe^{total}$ ratio through the lower 900–1100 km of the mantle, the resulting variations in the peridotite-melt Fe/Mg-partitioning and density relations are likely to be minor.

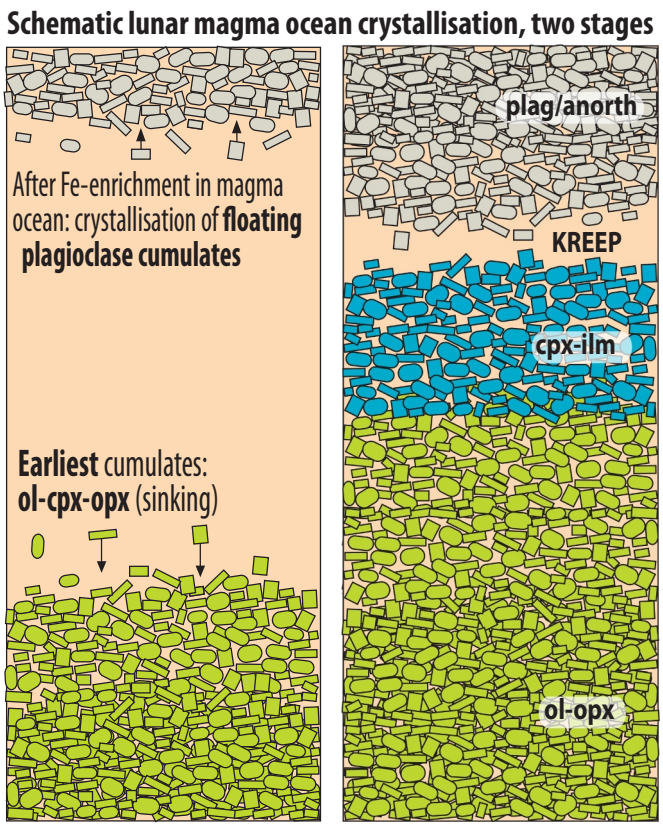


**Fig. 15.** Schematic illustration of the crystallisation of the lunar magma ocean. Abbreviations: ol, olivine; cpx, clinopyroxene; opx, orthopyroxene; plag, plagioclase; ilm, ilmenite; anorth, anorthosite, KREEP: residual melt enriched in incompatible elements, including K, REE (rare-Earth elements) and P. The sequence of crystallisation is: ol-opx-cpx, followed by plag and cpx-ilm. The cpx-ilm-cumulates and solidified KREEP-material have high densities and did likely cause overturn (inversion) of the magma ocean cumulate layers, resulting in convection and partial melting, possibly related to some of the Mare basalt volcanism.

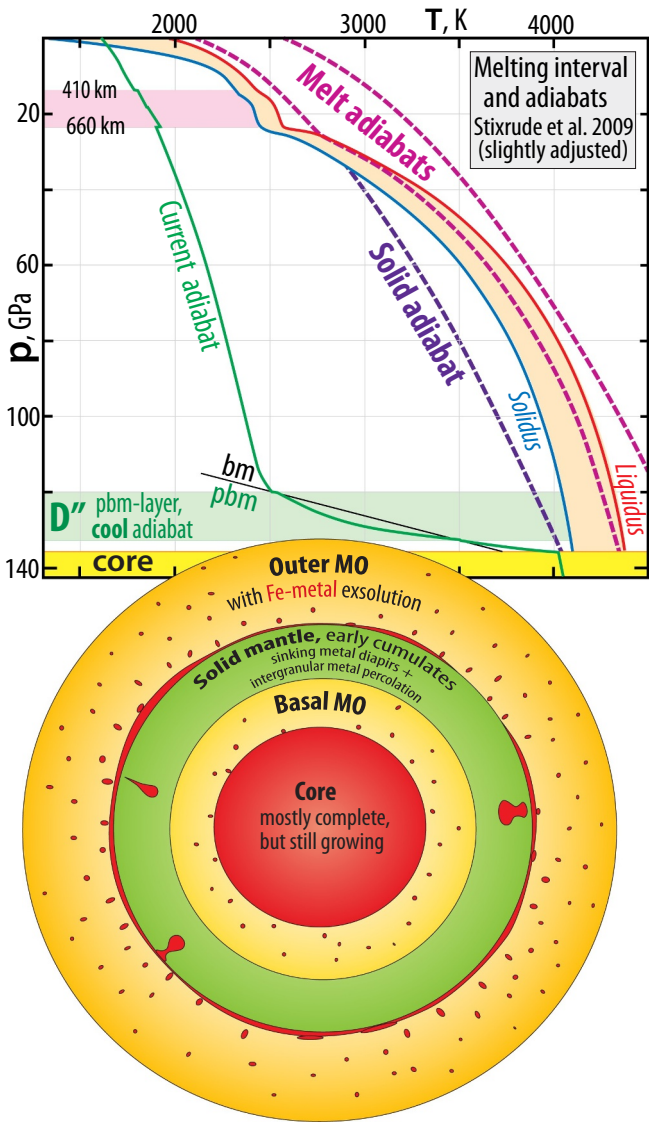


**Fig. 16. Top**: Melting interval (liquidus and solidus) for primitive mantle peridotite, 0–136 GPa, with Hadean melt and solid adiabats (stippled curves) relevant to the crystallisation of a magma ocean, as well as the current mantle adiabat (all from Stixrude et al. (2009)). The D″-zone is outlined in green. Abbreviations: bm, bridgmanite; pbm, post-bridgmanite. **Bottom**: Schematic illustration of the Earth with an outer magma ocean (outer MO) and a basal MO (BMO).

### 3.6. Magma ocean crystallisation and dense cumulates

In situations where the dT/dp-slopes of liquid peridotite adiabats are less steep than the dT/dp-slope of the curved and locally inflected peridotite liquidus, planetary magma oceans will crystallise from the bottom towards the surface (e.g. Walter and Trønnes, 2004). During the crystallisation sequence, density crossover between certain liquidus minerals and coexisting melt may develop, especially as the Fe/Mg-ratio of the melt increases during the crystallisation. A classic example is the plagioclase crystal floatation in the lunar magma ocean, recognised immediately after the Apollo 11 mission (Fig. 15; Smith et al., 1970; Wood et al., 1970; Grove and Krawczynski, 2009). The primary lunar anorthositic crust is still partly intact. The impact of Apollo-related petrological investigations, documenting the existence and crystallisation sequence of planetary magma oceans, has been profound. The bottom to top crystallisation of a magma ocean will generally lead to the final solidification of residual and dense (high Fe/Mg-ratio) melts at shallow levels in the planetary mantle. In the Moon, this resulted in shallow-level clinopyroxene-ilmenite-rich cumulates (source of later high-Ti basalts) and residual KREEP-material. Upon cooling and thermal contraction of the lunar interior, such an "inverted" density-profile could induce gravitational instability, sinking of dense cumulates and mantle convection episodes (e.g. Elkins-Tanton, 2012), possibly associated with mare basalt magmatism. At the higher pressures in Earth and Venus, the peridotitic melt adiabats may be subparallel to melting curves, as shown in Fig. 16 (Stixrude and Karki, 2005; Mosenfelder et al., 2007, 2009; Stixrude et al., 2009). Upon cooling of a terrestrial magma ocean, with this scenario, the liquid adiabats may initially intersect the liquidus at a mid-mantle neutral buoyancy level, causing two separate magma oceans (Fig. 16). The outer magma ocean and the basal magma ocean (BMO) will crystallise from the bottom and from the top, respectively, and the residual liquids collecting near the surface (as in the Moon, Fig. 15) and at the CMB will develop increasing Fe/Mg-ratios and density as crystallisation proceeds. During the early stages of crystallisation of the outer MO, moderately Fe-enriched melts might have drained through the early cumulates near the neutral buoyancy level, lifting them slightly to expand the BMO volume. A preexisting convection pattern of spherical harmonic degree-2 might have swept late-stage Fe-rich cumulate piles formed directly above the CMB into incipient LLSVP-layers (Labrosse et al., 2007; Torsvik et al., 2016).

Early theoretical studies based on experimental data established that komatiitic melts in equilibrium with peridotitic residues would also be neutrally buoyant with olivine (and pyroxenes) at about 300–350 km depths and therefore sink in the 350–410 km depth range (Stolper et al., 1981; Nisbet and Walker, 1982; Herzberg, 1984). This scenario, evaluated further by Lee et al. (2010), is shown in Fig. 17, left panel. In the three largest terrestrial planets, Earth, Venus and Mars, a melt accumulation zone would consequently be centred at depths corresponding to 14–15 GPa. This internal magma ocean would crystallise olivine and pyroxenes at the top (partly by floatation) and garnet and wadsleyite at the bottom (partly by sinking). The evolving residual melt would steadily increase its Fe/Mg ratio, reflected also by the last cumulate crystals. After cooling and thermal equilibration with the surrounding mantle, such residual cumulate piles at 410, 450 and 1100 km depths in Earth Venus and Mars, respectively (Khan and Connolly, 2008; Aitta, 2012), would have sufficient excess density to sink to the CMB. In the Earth and Venus, such material might either add to the dense cumulates formed in-situ above the CMB or, more likely, be dissolved in a long-lived basal magma ocean (BMO).

The crystallisation scenarios for magma oceans in planets like Earth and Venus, with mantle pressure ranges exceeding 100 GPa, will likely include a BMO, established after the initial crystallisation of bm from a neutral buoyancy level of 72–80 GPa (1700–1860 km depth) for the Earth. Because of the smaller size, lower pressure regime and lower $FeO^{mantle}$ content in Venus, its neural buoyancy level would be deeper and a BMO would be more restricted. The neutral buoyancy would result from the small density difference between pure $MgSiO_3$ bm and glass and a $K_D^{bm/melt}(Fe/Mg)$ below 0.1 at pressures exceeding 80 GPa (Fig. 14; Tateno et al., 2014; Petitgirard et al., 2015). Fig. 17 (right hand panel) summarises broadly the entire magma ocean cumulate stratigraphy in such large planets. Early crystallisation of Mg-rich bm, which is the first liquidus phase (Figs. 12 and 13), is expected at the neutral buoyancy level. The cotectic between bm and ferropericlase (fp) is close to a peridotitic bulk composition of the initial magma ocean, and a moderate amount of bm crystallisation will gradually increase the liquid (Mg + Fe)/(Si + Al) ratio, moving the composition towards saturation with ferropericlase. Transfer of $SiO_2$ from the core to the BMO and FeO in the opposite direction, which is a likely scenario discussed in Section 4, would extend the crystallisation of bm as the liquidus phase.

The efficient thermal insulation of a BMO, overlain by a solid mantle dominated by cumulates of $MgSiO_3$-enriched bm at 1500–1700 km depth and peridotitic cumulates at shallower levels, will prolong the high-temperature regime for the core and extend the BMO life-time (e.g. Labrosse et al., 2007; Laneuville et al., 2018). This will

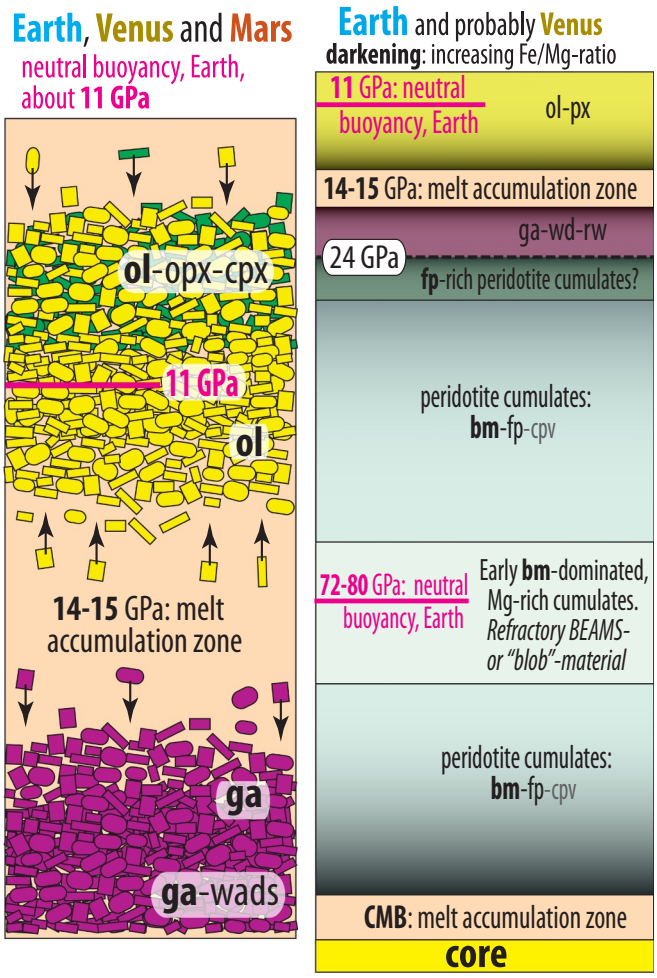


**Fig. 17.** Schematic illustrations of magma ocean crystallisation, mineral melt-neutral buoyancy and the nature of cumulates. **Left**: Pressure range of about 5–20 GPa, with a neutral buoyancy pressure of about 11 GPa for Earth (Lee et al., 2010). Melt accumulation zones at14–15 GPa and near the surface. This scenario is also applicable to Mars and Venus. Because the magma ocean (MO) and bulk mantle Fe/Mg ratios were higher for Mars and lower for Venus compared to Earth (Table 2), the neutral buoyancy pressures were lower for Mars and higher for Venus. The Venus MO might possibly not have reached the ol-melt neutral buoyancy pressure below the stabilisation of the denser phases wadsleyite and garnet. Mineral abbreviations are in Table 1. **Right**: Pressure range of about 8–150 GPa (for Earth), showing neutral buoyancy levels at 11 GPa and 72–80 GPa and melt accumulation zones above the transition zone and the CMB. Because the Venus MO had lower Fe/Mg ratio than the Earth, the occurrence of a lower mantle neutral buoyancy level and associated BMO is uncertain for Venus because of lower Fe/Mg ratio of its bulk MO. The establishment of neutral buoyancy in the lowermost parts of the upper mantle (left) and lower mantle (right), especially in Venus, might require some degree of prior crystallisation to increase the Fe/Mg ratio and density of the melt.

facilitate protracted core-mantle chemical transfer driven by a partial approach towards equilibrium between the protocore, BMO melt and bm and fp, crystallising at or near the top of the BMO. The timescale of the solidifying BMO is not firmly established, but it might have lasted through the Archean. A residual BMO could therefore have extended into the period of modern plate and Wilson cycle tectonics, starting at about 3 Ga (e.g. Shirey and Richardson, 2011).

## 4. Core-mantle interaction and D″ structure and dynamics

Core-segregation and (partial) equilibration between protocores and magma oceans at high temperatures in large terrestrial planets like Earth and Venus would have displaced the equilibrium:

$$SiO_2^{sil} + 2Fe^{met} = 2FeO^{sil} + Si^{met}$$

towards the product side, allowing extensive dissolution of Si into the core at relatively high oxygen fugacities and FeO concentrations in the silicate melt (e.g. Malavergne et al., 2004; Frost et al., 2008; Tsuno et al., 2013; Fischer et al., 2016; Hernlund, 2016; Laneuville et al., 2018). Cooling and slow crystallisation of a basal magma ocean (BMO) would reverse the equilibrium towards the reactants, making the core saturated with Si and undersaturated with O. This is the basis for the core-BMO chemical exchange to be reviewed in this section.

### 4.1. Core-mantle disequilibrium and exchange

Core-mantle interaction in the largest terrestrial planets, Earth and Venus, which experienced protracted accretion and high-temperature magma ocean processes on time scales exceeding 60–100 My, may be significant. During the BMO life-time, such interaction is expected to occur at a significant rate, changing the chemical composition of the protocore and the lowermost mantle. Even today the thin ultra-low velocity zones might represent partially molten domains with potential for chemical exchange with the core. Multi-anvil experiments by Otsuka and Karato (2012) at 12.5 GPa and 2000–2400 K with single crystals of fp in contact with liquid Fe-metal for up to 20 min, showed that 1–2 μm wide and 5–10 μm long worm-like tubes of Fe-melt penetrated into the crystal over total length scales of 50–70 μm, extracting FeO from the fp crystal during ascent. They suggested that the interfacial energy would be sufficient to pull such metallic melt fingers several km up into the lower mantle (see also Knittle and Jeanloz, 1991; Kanda and Stevenson, 2006). Even if such iron migration on km-scales could potentially overcome the severe limitations related to the slow chemical diffusion, especially in bm (Holzapfel et al., 2005), it is unsubstantiated at the pressure, temperature and dynamic flow conditions of the lowermost mantle.

The oxygen fugacity of 2.2 log-units below IW, calculated for the bulk core-mantle compositional pair of the Earth (Table 2) is considerably lower than the average $f_{O2}$ recorded by the mantle mineral assemblages (e.g. Frost and McCammon, 2008). This realisation has motivated several investigations of the chemical equilibrium between Fe-dominated metal and the minerals fp and bm at high pressures and temperatures (e.g. Ohtani and Ringwood, 1984; Rubie et al., 2004; Takafuji et al., 2005; Asahara et al., 2007; Ozawa et al., 2008). Frost et al. (2010) summarized the results on the Fe-FeO equilibrium, added more LH-DAC experiments and developed a thermodynamic model to investigate the equilibrium at CMB conditions (Fig. 18). The upper panel shows that the Fe-FeO immiscibility range contracts with increasing pressure and temperature, dramatically increasing the O-solubility in the metallic melt. The thermodynamic model (lower panel) indicates that Earth's present core composition (Table 2) would be in equilibrium with fp with Mg# 99, assuming a CMB temperature of 4000 K. This is a remarkable result, showing how far out of equilibrium the present convecting core is with a mantle with Mg# of about 90 and ferropericlase with Mg# below 86. Even the top of the E′-layer with an estimated O-content of 6.7 wt% (Table 3), recording extensive core-BMO exchange, would be in equilibrium with ferropericlase with Mg# 96–97. An inferred protocore (Table 3), compositionally intermediate between the current Earth and Venus core compositions, would be even more undersaturated with O.

At pressures of 60–140 GPa, fp is expected to have an Fe/Mg ratio about twice as high as that of the dominant ferromagnesian mineral bm (Section 3.6 and Prescher et al., 2014), even if the proportion of $Fe^{2+}$ in bm increases at pressures above about 90 GPa. The experiments by Otsuka and Karato (2012) confirm the tendency for extraction of FeO into the Fe-dominated metallic melt as the "capillary" irregular metal fingers dissolve the fp crystal as they migrate against gravity upwards through the crystal.

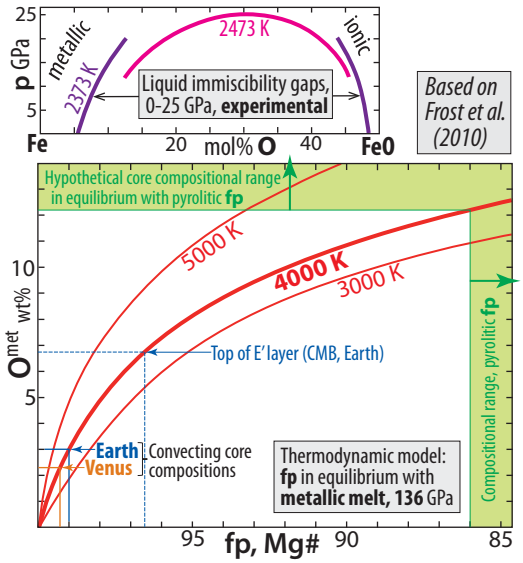


**Fig. 18. Top**: Liquid immiscibility in the system Fe-FeO at 0–25 GPa and 2373 and 2475 K. The metallic-ionic melt immiscibility range contracts rapidly with increasing pressure *and* temperature. **Bottom**: Thermodynamic model based on experimental data, illustrating the Mg-rich composition of ferropericlase (fp) in equilibrium with Fe-dominated metallic melt with variable O contents at 136 GPa (Frost et al., 2010). The Earth and Venus core compositions are from Table 2, and composition of the top of the E′-layer near the CMB is from Table 3.

LH-DAC experiments equilibrating bm and Fe-dominated metal at 25–97 GPa and 2300–3150 K resulted in similar relations (Takafuji et al., 2005). The upper panel of Fig. 19 shows the general trends for the O- and Si-contents of the metal as a function of pressure and Mg# of bm. In the concentration versus pressure diagram, the experimental temperatures are also broadly correlated with p and wt% O and Si. Takafuji et al. (2005) fitted the experimental results to the equation:

$$FeSiO_3{}^{bm} = Fe^{met} + Si + 3O$$

to derive thermodynamic data according to the relation:

$$RT \ln [a_{Fe}{}^{met}\, a_{Si}{}^{met}\, (a_O{}^{met})^3 / a_{FeSiO3}{}^{bm}] = -(\Delta H - T\Delta S + p\Delta V)$$

Based on the results, they constructed the relations between O- and Si-concentrations in the metal with coexisting bm with variable Mg#. The curves corresponding to 135 GPa and 3500 K are shown in the lower panel. As can be inferred from the upper panel, the O- and Si-concentrations in the metal increases with increasing p and T and with decreasing Mg# of bm. This is consistent with the thermodynamic modelling of the lower p- and T-conditions of 95 GPa and 3100 K (omitted for clarity), where the curve for bm with Mg# 95 almost overlaps with the Mg# 99.9 curve for the conditions of 135 GPa and 3500 K (lower panel). The Earth and Venus core compositions in Table 2 illustrates the gross disequilibrium between the present core and mantle bm in the Earth, and presumably also in Venus.

### 4.2. Chemical transfer: iron oxides to the core and silica to the mantle

The strong O-undersaturation in the core would promote the extraction of FeO and $Fe_2O_3$ from the BMO liquid. Iron is dominantly in the ferrous oxidation state in the Earth's mantle, and $Fe^{3+}$ constitute only about 2 mol% of total Fe in upper mantle peridotites (Canil and O'Neill, 1996) and presumably also in the convecting mantle. A net oxidation of the lowermost mantle would result if only FeO, and no $Fe_2O_3$, was extracted from the BMO to the core. The ferric oxide components in BMO liquid and solid bm, however, would presumably be extracted at least as efficiently into the outer core as the ferrous oxide components, and this would reduce the BMO and the solidified lowermost mantle.

Fig. 20 illustrates the effect of cyclic crystallisation and dissolution of bm near the ceiling of the BMO. The bm crystallisation would convert some ferrous iron to ferric iron, to be incorporated as the essential $FeAlO_3$ component (e.g. Frost et al., 2004). The ferric iron component is charge-balanced by exsolved metal, which would aggregate into growing and sinking drops (Wade and Wood, 2005). Partial dissolution of bm crystals below the BMO crystalline ceiling would release $Fe_2O_3$ (and $Al_2O_3$) to the silicate melt. Some of the $Fe_2O_3$ and FeO components in the BMO melt would dissolve in the metal droplets, ultimately sinking to the core. The drops were probably not completely saturated with O, but even if they were, this two-stage process would result in a net oxidation of the BMO because the O-saturation level in the metal at 136 GPa and 4000–4500 K is < 20 wt% (Figs. 18–19), whereas the O-contents of FeO and $Fe_2O_3$ are higher, i.e. 22.2 and 30.1 wt%, respectively. Andrault et al. (2018) emphasised the mechanism of BMO oxidation by bm-derived metal exsolution but did not consider the modifying effect caused by partial recharging of the metal with $Fe_2O_3$ and FeO from the BMO. The partitioning of Fe oxides from the BMO liquid into sinking Fe-dominated metal drops might have been an efficient mechanism for O transport into the cooling core, even if this process would have oxidised the BMO and lowermost mantle, as well as the core.

The dissolution of iron oxide into the core, either directly through the BMO-core interphase or via core-merging metal drops, would probably be accompanied by exsolution of Si as crystallising $SiO_2$ in the core (Hirose et al., 2017a). The upper part of Fig. 21 shows how the solubility limits in O-Si space vary with T and p. In general, the two elements are mutually exclusive in the metal, although the solubility range of combined O and Si increases with increasing temperature. Increasing pressure decreases their solubility ranges. The lower panel, representing the solubility limits at 136 GPa, shows compositional vectors for FeO-addition and $SiO_2$-fractionation. To maintain a constant O-content in the core, FeO and $SiO_2$ must be added and subtracted, respectively, in a 2/1 molar ratio, whereas the corresponding $FeO_{1.5}$/$SiO_2$ molar ratio would have to be 4/3. To increase the O-content, as expected for core evolution in the two largest terrestrial planets, Earth and Venus, the molar ratios must exceed these values. The Venus core composition in Table 2 is chosen to lie on a vector from the O-free core composition of Mercury with 15 wt% Si to the convecting core compositional estimate for the Earth (lower panel), which is within the range of Badro et al. (2015), based on seismological data and material physics properties.

Fig. 22, also based on Hirose et al. (2017a), shows the liquidus phase relations in the system Fe-Si-O (or Fe-FeSi-FeO) at 136 GPa and temperatures above 3500 K. These conditions are close to the silica phase transition between β-stishovite ($CaCl_2$-structure) and seifertite, and the location and slope of the phase boundary differ slightly between various experimental and theoretical studies (e.g. Driver et al., 2010; Grocholski et al., 2013 and references therein). The phase relations presented by Hirose et al. (2017a) involve cotectics parallel with and very close to the Fe-Si join, involving CaCl-structured FeSi, and the Fe-O join, involving hcp-Fe to 8 wt% O and FeO further on. The silica liquidus surface rises steeply inside these cotectics, strongly limiting the combined solubilities of O and Si in the liquid metal alloy at the outer core conditions. The figure also shows the core compositions of Mercury, Venus and Earth (Table 2), as well as a postulated early Haden protocore composition and the compositional vector from the Mercury core towards the current Earth core composition.

The elevated silica liquidus surface, extending to temperatures above 4000 K over most of the Fe-Si-O compositional space at 136 GPa, limits the permissible composition of the outermost core, assuming that the CMB temperature is 4000 K. In that case, the outermost core composition must project to the 4000 K contour or to the area outside, where the liquidus surface lies below 4000 K.

**Table 3**
Mass balance models illustrating a possible two-stage chemical exchange between magma oceans and cores.

Stage 1. **PC** + **earlyMO** = **convC** + **pyroliteMO**
Stage 2. **Upper-convC** (34 vol%, 31 wt% of core) + **BMO** (28 vol%, 34 wt% of mantle) = **E′-layer** + **mlmM**

**Abbreviations**, **explanations**: **PC**, hypothetical early protocore; **earlyMO**, hypothetical FeO-rich, early silicate magma ocean (12.4 wt% FeO, Moon mantle value, Table 2); **convC**: current convecting core (Table 2, see below); **pyroliteMO**, whole-mantle magma ocean with pyrolitic composition (Table 2); **upper-convC**, upper 445 km of the core, starting with convC composition; **BMO**, basal magma ocean, 1700–2891 km depth range, starting with pyrolite-MO composition; **E′-layer**, stagnant uppermost layer of the present core with a compositional gradient in the radial direction (Figs. 21, 22). **mlmM**, modified lowermost mantle, $SiO_2$-enriched and FeO-depleted. Distinct geochemical reservoirs, including thin Fe-rich bridgmanitic LLSVP base layers and voluminous and Fe-poor bridgmanitic blobs or BEAMS, were generated in the mlmM. Currently, the high-viscosity and refractory blob or BEAMS material would be convectively distributed over most of the lower mantle depth range (but esp. in the 1000–2600 km depth range). The high Mg/Fe ratio and large volume of such material will easily balance the Fe-poor mlmM composition. Mineral abbreviations as in Table 1.

**General approach**: we assume neutral buoyancy between bridgmanite and melt at 1700 km depth (72 GPa, PREM) with a $K_{DFe/Mg}^{bm/melt}$-value of 0.1 (Fig. 14). Even if the initial crystallisation might possibly have occurred at a slightly deeper neutral buoyancy level, within the 1700–1900 km depth range (e.g. at 80 GPa), the initial cumulate pile would likely float upwards as some of the dense fractionated melts sink through the initial pile (viscous layer of Andrault et al., 2018) into the BMO. For simplicity, we used the solid mantle PREM densities in the mass balance modelling involving the MO and BMO. This is largely justified due to the neutral buoyancy between peridotite and melt at about 11 and 72 GPa. The increase in BMO density during solidification and fractionation will be partly offset by the chemical exchange with the E′-layer. For the early protocore (PC) and convecting core (convC), we also used the PREM densities, with a reduction of the inner core densities by about 5%, corresponding to the current solid to liquid transition at about 5150 km depth. We used constant volumes for the current core and mantle in the calculations, in spite of small adjustments caused by the $SiO_2$-FeO exchange. In the calculations, we integrated the volumes and average densities for each 200 km or less (next to the discontinuous density changes recorded in PREM). For the E′-layer, we used four 100 km thick layers (0–400 km below CMB) and one 45 km thick layer (400–445 km below CMB). The calculated masses of the early PC (the entire core volume), E′-layer, earlyMO (total mantle volume) and BMO are 1935, 608, 4045 and 1381 Yg, respectively (1 Yg, yottagram = $10^{24}$ g).

**Chemical compositions**: the earlyMO was chosen to have 12.4 wt% FeO. The other oxides and elements of the earlyMO and PC were fitted in the mass balance model to yield a pyroliteMO. The E′-layer O-Si compositional vector is from Fig. 3 of Brodholt and Badro (2017). The median core estimate (3.9 wt% O and 2.8 wt% Si) of Badro et al. (2015) would result in negative Si-content in the uppermost E′-layer (near the CMB) to match the observed E′-gradient in seismic velocity (also discussed by Brodholt and Badro (2017)). The PC and convC compositions is on the vector from the Mercury through the Venus core. For the convC (="bulk" core, Table 1), we used a Si-rich and O-poor composition within the range of Badro et al. (2015). This yields a top E′-layer (at CMB) composition very close to the 4000 K contour on the silica liquidus surface in the system Fe-Si-O determined by Hirose et al. (2017a). The stage 2 mass balance model calculates the mlmM composition.

**Calculation of compositional gradient of the E′-layer**: the $V_P$ ($=V_\phi$) difference between PREM and the KHOMC model (e.g. Kaneshima, 2018, Fig. 9) is used as a starting point. We smoothed out the undulations of the KHOMC curve to obtain an even gradient as a basis for discrete $\Delta V_P^{PREM\text{-}KHOMC}$-values at 0, 100, 200, 300 and 400 km below the CMB. At 445 km below CMB, $\Delta V_P = 0$. The other five $\Delta V_P$-values of 0.433, 0.300, 0.174, 0.076 and 0.018%, respectively, were converted to corresponding values for density deficits, Si-depletion and O-enrichment, using Fig. 2b of Brodholt and Badro (2017).

| | | Composition, wt% | | |
|---|---|---|---|---|
| | | Si | O | Fe + Ni |
| **PC** (protocore) | | 5.12 | 2.60 | 92.3 |
| **convC** | | 3.60 | 3.00 | 93.4 |
| **E′-layer total** | | | | |
| From the mass of individual layers | | 2.21 | 4.62 | 93.2 |
| **E′-layer shells** | km below CMB | | | |
| | 0–100 | 0.87 | 6.17 | 93.0 |
| | 100–200 | 1.82 | 5.07 | 93.1 |
| | 200–300 | 2.62 | 4.14 | 93.2 |
| | 300–400 | 3.18 | 3.50 | 93.3 |
| | 400–445 | 3.50 | 3.12 | 93.3 |

| **E′-layer levels** | | | | |
|---|---|---|---|---|
| km below CMB | Density deficit, % | Composition, wt% | | |
| | | Si | O | Fe + Ni |
| 0 | 0.98 | 0.37 | 6.74 | 92.9 |
| 100 | 0.69 | 1.37 | 5.60 | 93.0 |
| 200 | 0.42 | 2.28 | 4.53 | 93.2 |
| 300 | 0.19 | 2.96 | 3.76 | 93.3 |
| 400 | 0.05 | 3.40 | 3.25 | 93.4 |

| | Composition, wt% (normalised to 100% sums) | | | | | | | | | | mol% minerals | | | mol-ratio |
|---|---|---|---|---|---|---|---|---|---|---|---|---|---|---|
| | $SiO_2$ | $TiO_2$ | $Al_2O_3$ | $Cr_2O_3$ | NiO | MnO | FeO | MgO | CaO | $Na_2O$ | bm | fp | cpv | bm/fp |
| **earlyMO** | 42.0 | 0.20 | 4.29 | 0.36 | 0.24 | 0.13 | 12.4 | 36.6 | 3.39 | 0.35 | 74.2 | 19.6 | 6.2 | 3.8 |
| **pyroliteMO**, calculated | 44.9 | 0.21 | 4.43 | 0.37 | 0.25 | 0.13 | 8.05 | 37.8 | 3.50 | 0.36 | 78.4 | 15.3 | 6.3 | 5.1 |
| **BMO**, pyr. Table 2, norm. | 44.9 | 0.20 | 4.44 | 0.38 | 0.25 | 0.14 | 8.04 | 37.7 | 3.54 | 0.36 | 78.3 | 15.3 | 6.4 | 5.1 |
| **mlmM**, calculated | 48.7 | 0.21 | 4.68 | 0.40 | 0.26 | 0.15 | 1.80 | 39.7 | 3.73 | 0.38 | 83.3 | 10.0 | 6.6 | 8.3 |

Combined $SiO_2$ fractionation and FeO assimilation would displace the protocore composition to the current convecting core composition (Table 2) and, by increasing the $FeO^{added}/SiO_2{}^{subtracted}$ ratio, further towards the E′-layer compositional vector (Table 3). In our mass balance modelling of this chemical exchange (Section 4.3; Table 3), we have chosen the protocore composition to be on the Mercury vector and an early whole-mantle magma ocean composition, which after core-MO exchange, yields a bulk pyrolitic mantle (Table 2). We further assume that the traces of a second-stage core-BMO exchange is recorded by our calculated chemical gradient of the outermost stagnant E′-layer of the core, based on the $V_P$-deviation of the KHOMC-model (Kaneshima, 2018) from PREM and the mineral physics calibration of the Si-depletion and O-enrichment of the E′-layer (Brodholt and Badro, 2017).

The outermost E′-layer composition (CMB composition) falls close to and slightly outside the 4000 K contour on the silica liquidus surface from Hirose et al. (2017a). With crystallisation and floatation (removal) of silica, accompanied by assimilation of FeO, the outermost E′-layer composition may have moved to and barely pierced through the silica liquidus surface. With a CMB temperature of 4000 K, the top of the E′-

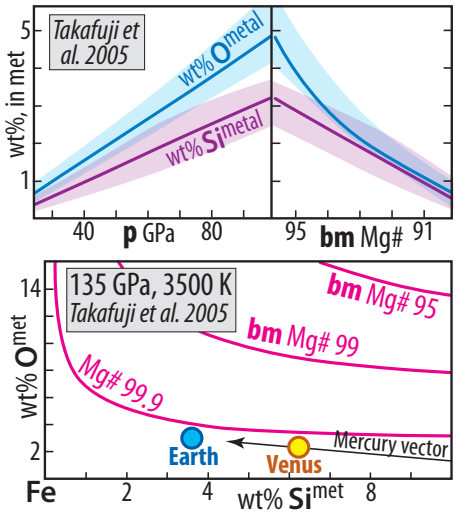


**Fig. 19. Top**: Approximate concentration of O and Si in metal in equilibrium with bridgmanite (bm) as a function of pressure and bm composition (Mg#) in the system Fe-Mg-Si-O. Experimental temperatures: 2750–2950 and 3000–3150 K at 30–60 and 90–100 GPa, respectively. **Bottom**: Thermodynamic model showing that extremely Mg-rich bm is in equilibrium with the Earth and Venus core compositions (Table 2). A vector between the Mercury (also Table 2) and Earth core compositions is also shown.

layer compositional gradient (Figs. 21–22) will therefore not crystallise silica.

Within most of the E′-layer pressure range of 136–182 GPa, seifertite will be the liquidus mineral, and the liquidus surface will presumably rise considerably in temperature in the pressure range just above the β-stishovite to seifertite transition. With an unrealistic assumption that the phase relations remain approximately unchanged through the E′-layer pressure range, the convecting core composition projects to the silica liquidus surface at a temperature of about 4600 K (Fig. 22, top panels and bottom, right inset). With a *convective* adiabat of 0.79 K/km in the outermost 445 km of the core, as indicated by Hirose et al. (2013) and Olson et al. (2015), the bottom of the E′-layer and top of the convecting core would be below the silica liquidus surface and crystallise seifertite. An E′-layer *conductive* geotherm considerably > 1.35 K/km, however, implies that the top of the convecting core might be at or above the crest of the silica liquidus surface (Fig. 22, lowermost right inset). Such a conductive geotherm is required in order to suppress crystallisation, especially when the silica liquidus surface expectedly rises with increasing pressures. The likely scenario for the present state of the core with a dominantly solid mantle and limited possibilities for core-mantle chemical exchange might be that silica crystallisation in the outer core has ceased. Seifertite crystallisation in the lower part of the E′-layer or outermost convecting core and dissolution near the CMB, especially without compensating FeO and $Fe_2O_3$ influx from the solid mantle, would reduce the O/Si ratio gradient of the E′-layer compared to our modelled O/Si molar ratio range of 32–1.7 in the 0–400 km depth range below the CMB (Table 3). The convecting core and stoichiometric silica have molar ratios of 1.5 and 2.0, respectively. The upper 300 km of the E′-layer, which has the largest chemical deviation from the underlying convecting core composition (Table 3), comprises 70% of the E′-layer by volume and mass.

The silica liquidus surface is expected to rise further in temperature in the 182–364 GPa pressure range. This temperature increase, relative to the slope of the convective core adiabat, will determine the conditions for, and the extent of, silica crystallisation at different stages of BMO and core evolution. The phase transition from seifertite to pyrite-structured silica at a pressure of about 268 GPa and 1800 K (Kuwayama et al., 2005; see also Wu et al., 2011; Umemoto et al., 2017) will likely result in further steepening of the silica liquidus with increasing

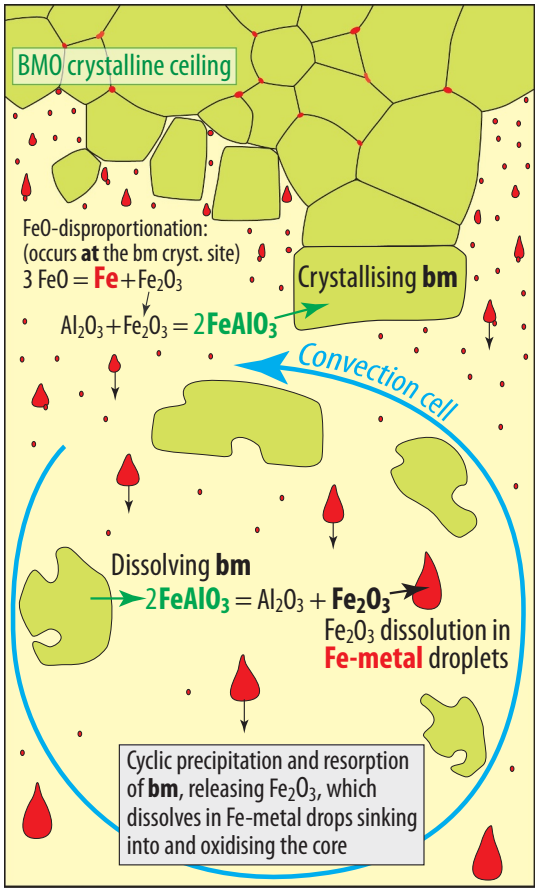


**Fig. 20.** Schematic diagram, illustrating cyclic crystallisation and dissolution of bridgmanite (bm) near the ceiling of the basal magma ocean (BMO). This is based on Frost et al. (2004), Wade and Wood (2005) and Wood et al. (2006) with the added modification that $Fe_2O_3$, released by resorption of bm, largely dissolves into the sinking Fe-dominated metal droplets. FeO from the BMO melt will also dissolve in the metal drops, which would gradually merge and grow while sinking through the BMO and ultimately sink into the core. This process might represent an efficient mechanism for O-loading of the core during the BMO life-time.

pressure. The Clapeyron slope of this transition is unknown, but with a slope of 2.5–10 MPa/K (0.035–0.14 km/K) and a core adiabat of about 1.8 km/K (e.g. Hirose et al., 2013; Olson et al., 2015; Laneuville et al., 2018), it might occur in the 4400–4900 km depth range. Extensive silica crystallisation might therefore have occurred in the lowermost 1500–2000 km of the core prior to the formation of the inner solid core. The dT/dp slope (or dT/dz slope, where z is depth) of the melting curve for the core alloy might be steeper than the core adiabat (Hirose et al., 2013; Olson et al., 2015), possibly favouring crystallisation at the deepest levels.

With an early and hot core alloy above the liquidus surface in the outer parts of the core, the question is whether and how silica crystals might have survived buoyant ascent to the outer regions towards the CMB. In this context, the local bulk compositions involving ascending liquid portions with entrained silica crystals would be decisive. Partial accumulation or aggregation of silica crystals to form meter- to hundred-meter-sized domains with low proportions of interstitial Fe-alloy melt would be a possible scenario to keep the local bulk (aggregate) composition well below the liquidus surface at any core pressure, even at very hot Hadean conditions. Schematic phase relations associated with such scenarios are illustrated in Fig. 22, lowermost, left panel. Crystal-rich plumes would have had strong compositional *and* thermal buoyancy, and could therefore have risen rapidly. The thermal buoyancy would stem from the latent heat of crystallisation and the

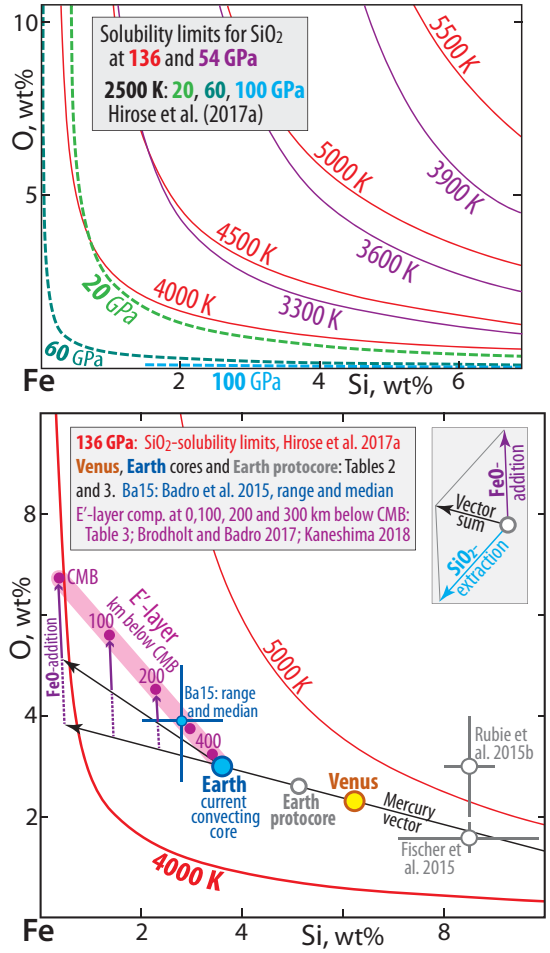


**Fig. 21.** Solubility limits for $SiO_2$ in Fe-dominated alloy as a function of O and Si concentrations. Mainly from Hirose et al. (2017a). **Top**: Solubility curves at 136 and 45 GPa for various temperatures (thin lines) and at 20, 60 and 100 GPa for the low temperature of 2500 K (thick, stippled lines). **Bottom**: Solubility limits at about 136 GPa and 4000–5000 K. The Venus and Earth core compositions are from Table 2 and an early Earth protocore composition from Table 3. A vector from the Mercury core composition (also Table 2) through the cores of Earth and Venus passes between the Fischer et al. (2015) and Rubie et al. (2015b) core compositions. The Earth protocore composition is also chosen to be on this vector (Table 3). Core evolution along such a vector corresponds to an appropriate combination of FeO addition and $SiO_2$ subtraction (upper right-hand inset figure). Mass balance modelling of an early stage evolution from the hypothetical protocore to the current convecting core by FeO-$SiO_2$ exchange (along the same vector) with an FeO-rich whole-mantle magma ocean leads to a pyrolitic whole-mantle magma ocean (Table 3, Section 4.3). A second stage exchange model involving a basal magma ocean (BMO, 28 vol% of the mantle) and the upper part of the current convecting core yields the stagnant E′-layer (34 vol% of the core, extending to 445 km below the CMB) with a radial compositional gradient, in addition to a chemically modified lowermost mantle. The second stage model, which is constrained by combined mineral physics and seismic data (Brodholt and Badro, 2017; Kaneshima, 2018; Table 3), involves a higher ratio of FeO-addition to the core to $SiO_2$-extraction from the core. The E′-layer compositional gradient, shown by compositions at 0, 100, 200, 300 and 400 km below the CMB, might result from the generation of core liquid batches between the Mercury vector and the E′-trend, followed by FeO-addition.

compositional buoyancy would be caused by the low-density silica crystal enrichment, even if the surrounding liquid might have had negative compositional buoyancy, resulting from Si- and O-depletion. Large crystal aggregates, as well as large individual crystals, would also have a high Stoke's ascent velocity relative to the surrounding liquid and could have left behind the compositionally dense liquid region where they originally formed. A recent evaluation of processes related to inner core nucleation and survival rate of solids in the core might be of interest in this context (Huguet et al., 2018).

Even if some of the crystalline material might have melted (dissolved) during buoyant ascent through the outer parts of the core, a resulting Si- and O-rich liquid plume might have had sufficiently large compositional buoyancy (Fig. 1a in Brodholt and Badro, 2017) to rise towards the CMB without being fully mixed with the ambient core fluid. Silica from rising Si-and O-rich metal plumes might easily dissolve into the BMO magma at the CMB interphase in exchange for Fe-oxide components dissolving in the outermost core. The most efficient mechanism of silica transfer, however, might be in the form of silica crystals with a density far below the core density and also below the BMO density. The silica crystals would also dissolve in the BMO magma. The dynamics of the possible E′-layer generation is still uncertain, especially if most of the silica crystallisation occurred in the deepest part of the core. Such an upper stagnant layer, however, must presumably reflect the local CMB transfer of silica crystals and melt component from the core and Fe-oxide components into the core.

### *4.3. Core-mantle chemical exchange: mass balance and compositional constraints*

To quantify the possible extent of chemical exchange between an early whole-mantle magma ocean and a protocore (stage 1) and the subsequent exchange between the BMO and the uppermost 34 vol% of the core, corresponding to a low-velocity E′-layer (stage 2), we performed simplified mass balance calculations, which are presented in Table 3. The calculations represent an endmember case in the sense that we used only ferrous iron oxide, FeO, and metallic Fe as iron-bearing components. Because the Fe/O weight ratios of FeO and $FeO_{1.5}$ are about 3.5 and 2.3, respectively, the amount of required Fe-transfer for a given amount of O-exchange is a maximum for the case of FeO as the only iron oxide. The stage 1 calculation is based on a hypothetical whole-mantle magma ocean with 12.4 wt% FeO and a hypothetical protocore, to yield a pyrolitic whole-mantle magma ocean (Table 2) and the current convecting core composition (Table 2). Although the chosen FeO content of the hypothetical early MO is the same as that of the lunar mantle (Table 2), we do not imply any specific significance to this correspondence. The stage 2 calculation is more accurately constrained, based on the $V_P$ profile for the E′-layer (Kaneshima, 2018) and the mineral physics and chemical relations presented by Brodholt and Badro (2017). This stage involves exchange between the uppermost 34 vol% of the core (bulk core, Table 2) and 28 vol% of the mantle (BMO with pyrolite composition, Table 2) to yield a compositionally gradational E′-layer and a modified lowermost mantle (mlmM) composition. Although the stage 2 calculations are strictly constrained by the velocity gradient in the outermost core and the mineral physics based density-velocity relations of Badro et al. (2014) and Brodholt and Badro (2017), they do not represent the detailed physical realities of the E′-layer establishment. As suggested in Section 4.2, the silica extraction might have occurred largely in the deeper parts of the core. An evaluation of the convective readjusting flow and thermal equilibration of thermally light, but chemically dense, liquid from the main crystallisation regions is beyond the scope of this review. It seems likely, however, that FeO- and $Fe_2O_3$-addition to liquids lying between the Mercury vector and the E′-layer compositional trend is essential during the latest stage of the E′-layer establishment (Figs. 21–22). A requirement for the establishment of an E′-layer might be that silica-loss by crystallisation and ascent is restricted to the outermost core and occurs simultaneously with Fe-oxide supply from the BMO. Further experimental and theoretical constraints on the silica liquidus surface in the system Fe-Si-O and on core adiabats are needed to clarify this.

The calculated mlmM composition (modified lowermost mantle, i.e. 28% of the mantle, corresponding to the former BMO) has a low FeO content of 1.8 wt% and an elevated bm/fp ratio of 8.3, corresponding to 83.3, 10.0 and 6.6 mol% bm, fp and cpv, respectively. The lithological

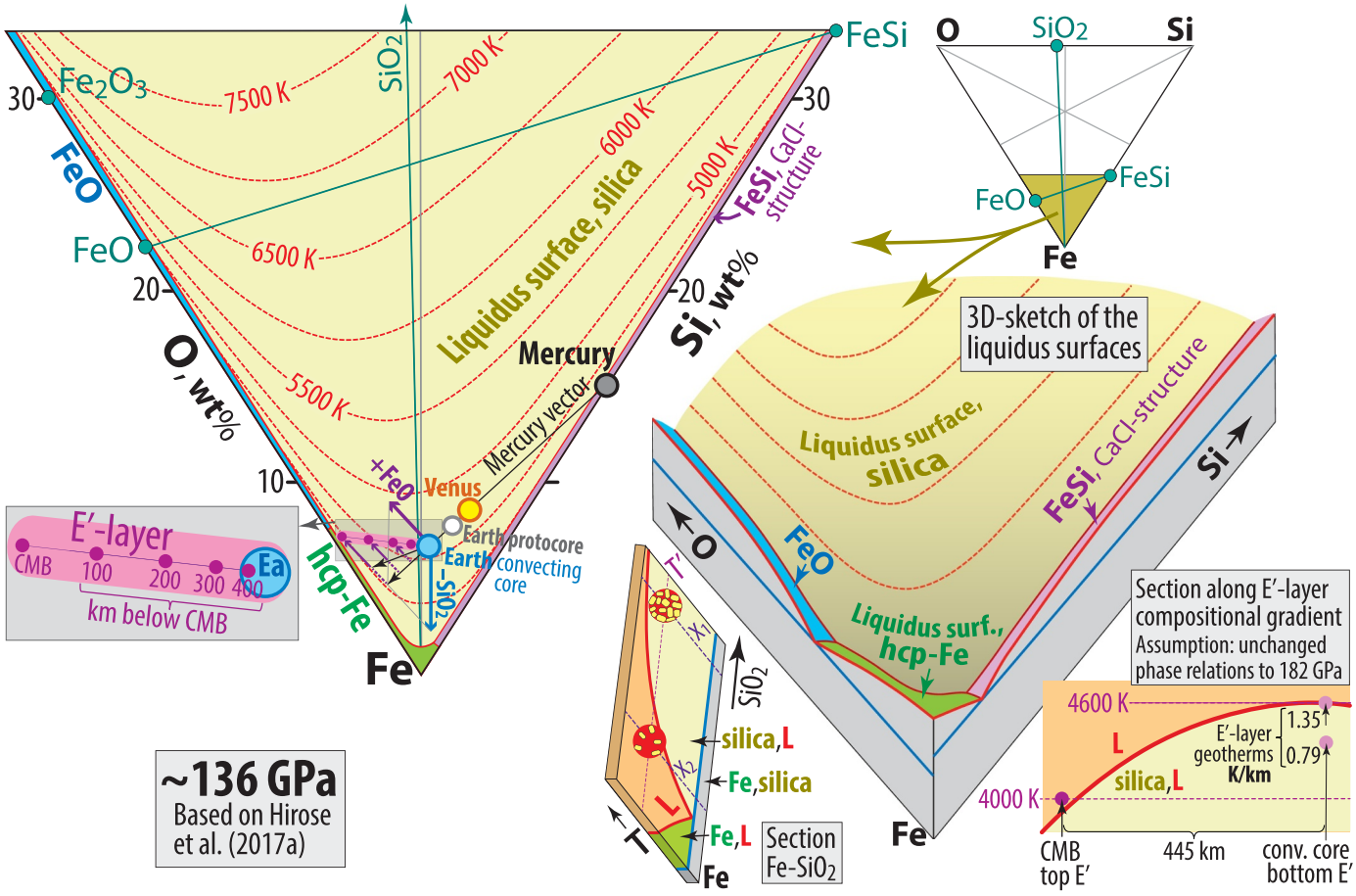


**Fig. 22.** The **main upper left panel** shows the liquidus phase relations in the Fe-rich part of the system Fe-Si-O at about 136 GPa from Hirose et al. (2017a). The core compositions of Mercury, Venus and Earth are from Table 2 and the Earth protocore composition is from Table 3. The E′-layer compositional gradient is shown by compositions at 0, 100, 200, 300 and 400 km below the CMB (see also left inset figure). The mass balance modelling involving Earth's protocore, current convecting core, E′-layer and corresponding magma oceans is described in Table 3, Fig. 21 and Section 4.3. The **three lower right panels** include a three-dimensional perspective sketch of the liquidus surfaces (middle), a section along the Fe-rich part of the Fe-$SiO_2$ join (lower left) and a section along the E′-layer compositional gradient (lower right). The latter section, to be used to illustrate principles regarding precipitation or dissolution of silica along the E′-gradient, is oversimplified because it assumes that the phase relations are approximately unchanged in the 136–182 GPa range. Although the E′-layer pressure range of 46 GPa is only 20% of the core pressure range, the silica liquidus surface might increase considerably in temperature within this range. The lower left Fe-$SiO_2$ section illustrates the effect of aggregation (or collection into local concentration maxima) of silica crystals on their stability and ability to survive during buoyant ascent through the core. At a temperature of T′, silica crystals are stable in the "local" composition $X_1$ with high proportion of (aggregated) silica crystals. In contrast, pre-existing crystals are not stable and will tend to dissolve in the composition $X_2$ at the same pressure and temperature condition. hcp-Fe: hexagonally close-packed Fe.

units likely to form in such a compositionally evolving BMO include voluminous early refractory, bridgmanitic cumulates, and minor late-stage Fe-rich cumulates. With a $K_{DFe/Mg}^{bm/melt}$ value of 0.1, or below 0.1 at pressures exceeding 80 GPa (Section 3.5), the earliest crystallised bm in the uppermost part of the BMO would have Mg# of 98.8 or higher. With a chemical tendency for core-BMO exchange of $SiO_2$ and iron oxides, a large proportion of the BMO would ultimately have crystallised as $MgSiO_3$-rich bridgmanitic cumulates. Due to high viscosity and neutral buoyancy around 1900 km depth, also in the solidified mantle (Section 3.5), the cumulates might have been convectively aggregated into large blobs or BEAMS (Becker et al., 1999; Ballmer et al., 2017) in the middle part of the lower mantle and largely preserved to the present time. The late-stage crystallisation of the BMO, however, would result in cumulates with relatively Fe-rich bm and some coexisting fp and cpv. Such material might have given rise to 100–200 km thick base layers within the LLSVPs (Section 4.5). With an outermost core temperature of about 4500 K during an intermediate to late stage of BMO crystallisation, the ferropericlase-metal equilibrium of Frost et al. (2010) gives an O-saturation level of about 15 wt% O in the outermost core, assuming a pyrolitic BMO and a $K_{DFe/Mg}^{bm/fp}$ of 0.5 (Prescher et al., 2014). In spite of the loss of Fe-oxides to the core, the Fe-concentration of the BMO melt is unlikely to fall below that of an original pyrolitic MO composition due to extensive crystallisation of buoyant bridgmanitic cumulates with high Mg/Fe ratios near the BMO ceiling.

### 4.4. Core-mantle exchange: heat generation

Heat generated as a net effect of core-BMO chemical exchange might have been essential for powering the early geodynamo prior to the start of inner core crystallisation. Such heat would have flowed into the BMO and prolonged its life-time. If the thermal conductivity of outer core metal is as high as some recent studies have suggested (de Koker et al., 2012; Pozzo et al., 2012; Gubbins et al. 2015; Ohta et al., 2016), the resulting thermal and chemical buoyancy could have driven core convection prior to the start of inner core crystallisation. A stagnant E′-layer of the outermost core, facilitated by such high conductivity, may also have a stabilising effect on the dynamo (Sreenivasan and Gubbins, 2008; Hernlund and McNamara, 2015).

The strong reduction of the $SiO_2$-solubility of Fe-metal (Fig. 21, upper panel), and a likely increase in the silica liquidus surface with

increasing pressure, suggests that silica crystals might have formed over an extensive depth interval, and primarily in the innermost part of the core. Crystals-rich plumes were likely to rise towards the CMB, where silica could dissolve into the BMO and/or react with fp to form bm. The silica crystallisation and density-driven rise of crystals and surrounding liquid, are exothermic processes. The latent heat of crystallisation would add thermal buoyancy to the crystal-rich plumes and the dense sinking counter-flow would convert additional potential energy to heat. The dense residual liquid alloy depleted in Si and O after silica crystallisation would have had negative compositional buoyancy, releasing heat during descent. Crystallisation of silica directly at the CMB or reaction of the silica component from the metallic melt with fp to form bm are also exothermic, but less likely processes. The complementary dissolution of FeO and $Fe_2O_3$ into the core, however, is endothermic.

Whereas the exchange of 1 mol $SiO_2$ with 2 mol FeO conserves the total mass of O in the core, it implies a net core growth of 2Fe − Si = 85.6 g, with an associated heat generation (e.g. Rubie et al., 2015a). The corresponding exchange of 1 mol $SiO_2$ with 2/3 mol $Fe_2O_3$, also conserving the O content of the core, would result in a net core growth of 4/3 Fe − Si = 46.4 g. A more likely scenario with increasing O content (e.g. Figs. 21–22), results in more extensive core growth. An increase of 1 mol O based on the exchanges 3FeO versus $SiO_2$ and $Fe_2O_3$ versus $SiO_2$ would lead to a core growth of 155.4 and 99.6 g/mol, respectively. The sinking of iron alloy drops, charged with some O (Fig. 20), from the BMO to the core and a similar leakage of O-charged Fe-alloy from ULVZs to the core (Fig. 23) involve additional minor core growth and heat generation.

Additional exothermic energy to drive an early geodynamo might have been provided by the exsolution of MgO and $Al_2O_3$ from the core (Wahl and Militzer, 2015; O'Rourke and Stevenson, 2016; Badro et al., 2016). Because the solubility of MgO and $Al_2O_3$ in Fe-dominated metal under protocore temperatures of about 5600 K (Laneuville et al., 2018) are considerably lower than that of Si (Figs. 6, 20), the heat contribution from the exsolution of MgO and $Al_2O_3$ is expected to be minor compared to that of the $SiO_2$ exsolution. If the solubilities of MgO and $Al_2O_3$ in the core are independent of pressure (Badro et al., 2016), the oxide exsolution would mainly occur at the lowest temperatures of the outermost core. Negative buoyancy of sinking Fe-enriched melt and positive buoyancy associated with the lighter counter-flow would therefore be the main convective contributions. The conversion of potential energy to heat associated with this re-distribution of mass would also transfer minor thermal buoyancy to the deeper parts of the core.

### 4.5. Long-lived, major mantle heterogeneities

The delivery of $SiO_2$ to the BMO and extraction of FeO and $Fe_2O_3$ from the BMO would stabilise bm as the primary liquidus phase during prolonged periods of crystallisation, increasing the amount of early bm-cumulates with low Fe/Mg ratios, centred at a neutral buoyancy level at 72–80 GPa pressure and 1700–1860 km depth (Fig. 17). Such bm-dominated cumulates would be refractory and viscous, providing resistance to convective and diffusional homogenisation with the ambient mantle. Slightly positive $^{142}Nd/^{144}Nd$ deviations from the bulk mantle composition of primitive basalts and picrites in the North Atlantic and Ontong Java large igneous provinces (Rizo et al., 2016) might originate from such cumulate material. Rizo et al. (2016) found corresponding positive $^{182}W/^{184}W$ deviations in these lavas, possibly indicating that some of the refractory heterogeneities were established before, and survived through, the last major magma ocean, following the Moon-forming impact. The validity of the positive $^{182}W/^{184}W$ anomalies, however, has been questioned by Kruijer and Kleine (2018). $MgSiO_3$-dominated bridgmanitic material is very refractory in the lower mantle. If it is entrained in hot plumes and converted to orthopyroxene in the upper mantle, however, it becomes less refractory and may contribute to the magma during large-scale melting of a diverse lithological mixture expected in starting plume heads, as well as in major stationary plume conduits.

Moderately elevated density, higher bulk modulus and higher viscosity compared to the surrounding D″ materials are three favourable properties for discrete, antipodal thermochemical LLSVP piles with locally steep and seismically resolved sides and long-term stability (e.g. Garnero and McNamara, 2008; Wolf et al., 2015; Torsvik et al., 2016; Heyn et al., 2018). Without the inferred core-BMO chemical exchange, the residual melts and final BMO cumulates near the CMB might have acquired too high Fe/Mg ratios and density to form two discrete accumulations. The cumulates might also have acquired too large fp contents to satisfy the requirements of high bulk modulus and high viscosity without silica addition and Fe-oxide loss. We discuss the observed density contrasts and the likely compositions of bm-rich thermochemical piles in Section 4.7.

Limited exchange between the core and the lower late-stage cumulates when the BMO was nearly completely solidified, could partially modify the dense Fe-rich bm-fp-cpv cumulates to slightly less dense lithologies with reduced Fe/Mg and fp/bm ratios, possibly to nearly 100% bm and minor cpv. FeO and $Fe_2O_3$ extraction to the core, combined with the transfer of liquid silica component to the last BMO magma might alter lower cumulate layers with broadly peridotitic (Fe + Mg + Ca)/(Si + Al) ratios of up to 1.33 to bm-cpv lithologies with ratios near unity. The volumes of such modified late-stage cumulates would be much lower than those of $MgSiO_3$-rich, bm-dominated early cumulates crystallising at the neutral buoyancy level near the top of the BMO. The core-BMO exchange during the early bm crystallisation period could have produced voluminous domains in the lower mantle with pyroxenitic, i.e. strictly bridgmanitic, composition.

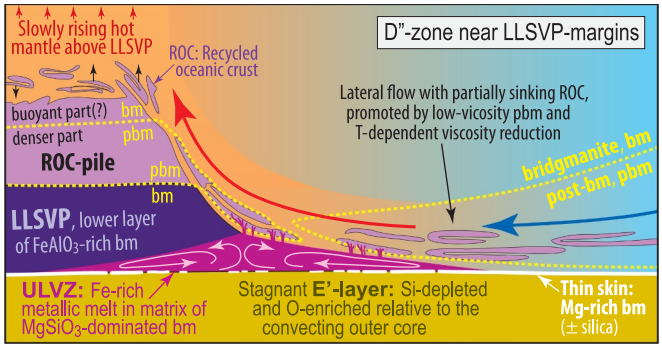


**Fig. 23.** Inferred structure and dynamics of the D″-zone, modified from Torsvik et al. (2016). Internal convection in the ULVZ is indicated by arrows, and the continuous lateral flow along the core-mantle boundary is shown by blue (cool) and red (hot) arrows. The distribution of post-bridgmanite (pbm) is indicated in the cool regions away from the LLSVPs, in thin basaltic ROC slivers (recycled oceanic crust) and in the lower parts of basaltic ROC accumulations above a thin and stable layer of bridgmanitic LLSVP-material, rich in the $FeAlO_3$ component. Extensive stability of pbm in basaltic material relatively high above the CMB within the LLSVP-regions is supported by seismic tomography modelling of Koelemeijer et al. (2018) and by atomistic simulations by Mohn and Trønnes (2018), who found a more restricted stability range of pbm in bridgmanitic material with moderate amounts of the $FeAlO_3$ component (about 16 mol%). The D″ flow with minor differential sinking of ROC is promoted by low-viscosity pbm (Amman et al., 2010; Nakada and Karato, 2012; Goryaeva et al., 2016). An outermost stagnant E′-layer of the core is inferred from Brodholt and Badro (2017). A thin skin of nearly pure $MgSiO_3$-bm, formed by core-mantle chemical equilibration, may be locally and intermittently stable. Due to low diffusion rate in bm (e.g. Holzapfel et al., 2005), and in spite of its positive buoyancy, such a layer might provide a temporal chemical barrier between core and mantle (e.g. Frost and McCammon, 2008). The thin layer may be episodically eroded under the ULVZs, which may tend towards equilibrium with the outermost core. Our preferred ULVZ-material is therefore interstitial dense metallic melt largely derived by partial melting of ROC slivers (Liu et al., 2016) in a matrix of $MgSiO_3$-dominated bm. Small melt veins tapping low-degree metallic melts from the ROC slivers to the ULVZ are schematically indicated in the figure.

The calculated bulk "modified lowermost mantle" (Table 3, Section 4.3), corresponding to the BMO fraction of 28 vol% of the mantle and 41 vol% of the lower mantle, has 1.8 wt% FeO and a mineralogy of 83.3, 10.0 and 6.6 mol% of bm, fp and cpv, respectively. Currently, most of this domain may be occupied by the ambient convecting mantle of depleted peridotite and 6–7 vol% of basaltic slivers (recycled oceanic crust). The early refractory bridgmanitic cumulates with high viscosity, perhaps comprising as much as 15–30 vol% of the lower mantle, were likely aggregated by convection into irregular blobs or larger BEAMS (Becker et al., 1999; Ballmer et al., 2017; Hirose et al., 2017b) in the 1000–2600 km depth range.

The volumes of late-stage dense BMO-cumulates within the LLSVPs are much more limited. With a maximum thickness of 100 km, as suggested by the Stoneley mode analysis of Koelemeijer et al. (2017), the two LLSVPs comprise only 0.4 vol% of the entire mantle and 0.6 vol % of the lower mantle. Based on other seismological models for the LLSVP density excess (Ishii and Tromp, 1999; Moulik and Ekström, 2016; Lau et al., 2017), we infer a base layer thickness of about 150 km, which would imply a volume fraction of about 0.9% of the lower mantle. The LLSVP-areas limited by the $-1\%$ $\delta V_S$-contour in the SMEAN model (Becker and Boschi, 2002) cover about 23% of the CMB surface. A base layer thickness of 150 km within the LLSVPs spread evenly over the entire CMB surface ($1.5 * 10^8\,km^2$), would correspond to a global CMB-layer thickness of about 35 km. The low volume/surface ratio of the base layer LLSVPs cumulates, even if they were rapidly swept into piles, might have exposed them to chemical exchange with the core via late-stage thin lenses of BMO residual liquid.

### 4.6. Ultra-low velocity zones

The absence of core-BMO chemical equilibrium is partly related to the very limited solid-state diffusion rates, especially in bm (e.g. Holzapfel et al., 2005). Based on the low diffusion rates and the existing data for the fp-metal and bm-metal equilibria in the Fe-Mg-O and Fe-Mg-Si-O systems, Frost and McCammon (2008) suggested that a thin layer at the CMB ("only a few meters thick") with low contents of FeO and $Fe_2O_3$ would shield the mantle from further extensive exchange with the outer core. The Fe-Si-O phase relations (Figs. 21–22; Hirose et al., 2017a) support the notion that a thin skin, which may intermittently be eroded, would contain $MgSiO_3$-dominated bm, possibly with minor additional amounts of seifertite (Fig. 23). Minor seiferitite within this thin skin does probably not originate from core crystallisation, but rather from FeO and $Fe_2O_3$ extraction to the core by decomposition of bm. Although such a layer would be buoyant, the limited thickness, due to the low bm diffusion rates, and a high viscosity might contribute to survival on intermediate time scales. After an episode of convective erosion, a thin layer might grow rapidly, before the limiting diffusion rates slow the growth again.

The most favourable sites for minor core-mantle exchange at the present might be the ULVZs, which appear to be partially molten and preferentially confined to the root zones of concentrated upwelling near the LLSVP margins (e.g. Lay, 2015; Liu et al., 2016; Torsvik et al., 2016; Yuan and Romanowicz, 2017). Internal convection in the 5–40 km thick ULVZs is probably required in order to explain the lack of extensive melt separation from the solid matrix (e.g. Hernlund and Jellinek, 2010; Lay, 2015; Liu et al., 2016). Therefore, we infer that the thin and chemically insulating layer of $MgSiO_3$-dominated bm might be preferentially eroded under the ULVZs (Fig. 23), which might approach chemical equilibrium with the core. Materials rich in iron oxides are unlikely ULVZ candidates in that case. Subducted banded iron formations (Dobson and Brodholt, 2005), Fe-rich post-bridgmanite (Mao et al., 2006) and subducted goethite-rich lateritic sediments converted to H-bearing Fe-peroxide, $FeO_2H_x$ (Liu et al., 2017) can probably also be excluded. Our preferred ULVZ materials are instead low-degree, Fe-O-C-dominated metallic liquids in a matrix dominated by bm, enriched in the $MgSiO_3$ and $Al_2O_3$ components after extraction of FeO and $Fe_2O_3$ to the core and to the interstitial ULVZ melt. The ULVZ matrix is also likely to contain moderate amounts of cpv, enriched in the heat-producing and other large-ion lithophile elements (Corgne and Wood, 2005).

Liu et al. (2016) suggested that a Fe-C eutectic liquid can be derived continuously by low-degree melting of recycled oceanic crust (ROC) in the hot regions of the D″ zone (Fig. 23). Altered oceanic crust has commonly some carbonate, which will be reduced to diamond in subducted slab material when it sinks into the stability field of metallic Fe, coexisting with majoritic garnet and bridgmanite at depths exceeding 250 and 660 km, respectively (Rohrbach and Schmidt, 2011; Walter et al., 2011). ROC has probably also considerable amounts of metallic Fe, exsolved during FeO-disproportionation during incorporation of a large proportion of an $FeAlO_3$ component in bm. At 136 GPa, an Fe-C eutectic with 2.2 wt% C forms at about 3700 K (Fei and Brosh, 2014; Supplementary Fig. S2), which is about 270 K below the C-free basalt solidus (Pradhan et al., 2015). An interstitial metallic melt approaching equilibrium with bm and the uppermost E′-layer alloy, will likely acquire higher concentrations of O (about 7 wt%; Fig. 21) compared to Si ($\leq$1 wt%; Figs. 19, 21) and C. A continuous replenishment of the ULVZs with a near-eutectic metallic melt fraction from the partial melting of subducted basalts and the leakage of some of the interstitial melt into the E′-layer might imply a very slow ongoing core growth. A consequence of such a minor ULVZ-based core growth may be a further weak oxidation of the D″ zone.

### 4.7. Density, bulk modulus and viscosity of LLSVP and refractory bridgmanitic material

Bridgmanitic LLSVP piles with elevated Fe/Mg ratios would result in elevated density, bulk modulus and viscosity compared to an ambient peridotitic mantle (Amman et al., 2010; Marquardt and Miyagi, 2015; Irifune and Tsuchiya, 2015; Girard et al., 2016; Wolf et al., 2015). It is noteworthy that the present spherical harmonic degree-2 pattern involving the LLSVPs, the residual geoid and the large-scale convection pattern of the Earth is linked to the rotation axis (e.g. Steinberger and Torsvik, 2010; Dziewonski et al., 2010; Torsvik et al., 2016). We suspect that the high rotation rate of the early Earth might have stabilised such a convective pattern, possibly even at the BMO stage, before the collection of intrinsically dense material in the root zones of the two antipodal upwelling columns.

The density excess of 1.0–1.5% for the inferred 100–200 km thick thermochemical piles of the LLSVPs (Ishii and Tromp, 1999; Moulik and Ekström, 2016; Lau et al., 2017) includes the intrinsic material density excess with a reduction due to elevated LLSVP temperatures. Equation of state data along the lower mantle adiabat presented by Irifune and Tsuchiya (2015) yield material densities for basalt, fertile peridotite (pyrolite) and harzburgite at 115 GPa of 5447, 5397 and 5387 $kg/m^3$ respectively, compared to the PREM density of 5404 $kg/m^3$ (Dziewonski and Anderson, 1981). This corresponds to density deviations from pyrolite of $+0.93\%$ for basalt and $-0.18\%$ for harzburgite. Because basaltic lithologies might have higher bulk moduli than peridotite (e.g. Ballmer et al., 2015, 2016; Torsvik et al., 2016), the intrinsic density excess will increase in a rising mantle column, e.g. to 1.41% at 40 GPa. We estimate roughly the thermal expansion effect, using an excess LLSVP temperature of about 750 K at 200 km above the CMB. The lateral T variation in the D″ layer is estimated from the observed depths of D″ discontinuities in various high S-wave velocity regions from Figs. 6 and 8 in Lay (2015) and the dp/dT slope of the bm-pbm transition in $MgSiO_3$ from Tateno et al. (2009). Based on Cobden et al. (2015), we assume that pbm is absent in peridotitic and bridgmanitic rocks in the LLSVP regions. With thermal expansion coefficients for bm from Wolf et al. (2015), the basaltic lithology changes from negative buoyancy ($\Delta\rho$: $+0.93\%$) to slightly positive buoyancy ($\Delta\rho$: $-0.06\%$) at LLSVP temperature conditions. Accumulations of recycled oceanic crust are therefore unlikely to constitute stable thermochemical LLSVP-

layers. Relatively stable 100–200 km thick layers of modified lowermost mantle cumulates, however, may be overlain by unstable piles of nearly neutrally buoyant basaltic material, behaving in a "lava lamp fashion" in the rising hot mantle column above the LLSVPs (Ballmer et al., 2016; Torsvik et al., 2016).

We have also estimated the intrinsic material density excess for bm-dominated LLSVP layers with a globally averaged D″ temperature of the lower LLSVP-layers at 130 GPa, assuming a density excess of 1.25%, which is the average estimate of Ishii and Tromp (1999), Moulik and Ekström (2016), and Lau et al. (2017). Using a temperature difference of 750 K and a thermal expansion coefficient of $1.27 * 10^{-5} K^{-1}$ from Wolf et al. (2015), the derived intrinsic material density excess is 2.2%. Fig. 24, based on Wolf et al. (2015), relates the composition of bridgmanitic LLSVP-layers to differences in temperature, density and isentropic bulk modulus (ΔT, Δρ and $\Delta K_S$) between the LLSVPs and the ambient D″ materials, represented by PREM. The detailed p-V-T equation of state data of Wolf et al. (2015) are confined to the system $MgSiO_3$-$FeSiO_3$, and yield a bm composition with about 16 mol% $FeSiO_3$ for ΔT of 750 K and Δρ of 1.25%. At the same ΔT, the neutrally buoyant bm composition will have 12.2 mol% $FeSiO_3$ (grey stippled line).

Because the $FeSiO_3$ and $FeAlO_3$ components have similar molar weights of 131.9 and 130.8 g, respectively, i.e. about 31% higher than that of $MgSiO_3$ (100.4 g), the densities might be similar for the two iron components. Our preliminary DFT results indicate that the volume and density of bm with 16 mol% $FeAlO_3$ are 0.6% higher and 0.7% lower, respectively, than those of bm with 16 mol% $FeSiO_3$ at 120 GPa and 3000 K. Replacing 16 mol% $FeSiO_3$ by 16 mol% $FeAlO_3$ in the LLSVP bridgmanitic layer would therefore amount to < 0.01% of an inferred density contrast of 1.25% between the LLSVPs and the surrounding D″ zone, assuming that the thermal expansion of the two bm solid solutions are broadly similar. In spite of considerably lower bulk modulus, $K_0$, and its pressure derivative, K′, for the $FeAlO_3$ component of bm compared to those of the $FeSiO_3$ component (e.g. Caracas, 2010; Kurnosov et al., 2017), Caracas (2010) also found a 0.2% density reduction of bm with 16 mol% $FeSiO_3$ at 120 GPa and the static limit (0 K) compared to that for bm with 16 mol% $FeAlO_3$.

Fractional crystallisation of a BMO affected by core-mantle exchange is expected to enrich both Al and Fe in the residual melt. The $Al_2O_3$ solubility in bm appears to be well below 10 mol% at D″-pressures, which might favour a high proportion of the $FeAlO_3$ component (Mohn and Trønnes, 2018). At a given temperature the $FeSiO_3$ component alone would reduce the pressure of the bm-pbm transition relative to $MgSiO_3$ considerably (e.g. Mao et al., 2004; Mohn and Trønnes, 2018), whereas the $FeAlO_3$ component would not change the pressure of the transition much, because the $MgSiO_3$-$FeAlO_3$ phase loop is flat and narrow, i.e. nearly constant in pressure (Mohn and Trønnes, 2018). The observations that the D″-discontinuities are confined mainly to the longitudinal high-velocity belt under the Arctic, Asia, Australia, Antarctica and the Americas (Cobden et al., 2015; Lay, 2015), indicate that the $FeAlO_3$ component may be the dominating iron components in bm in the LLSVP base layer. Koelemeijer et al. (2018) infer the presence of pbm in basaltic lithologies in the LLSVP domains up to about 300 km above the CMB. In this pressure range, pbm is expected in a basaltic lithology, containing about 34 mol% pbm with 21, 9 and 7 mol% of the $FeAlO_3$ and $FeSiO_3$ components, respectively, assuming a temperature profile of 500 K above the Stixrude et al. (2009) geotherm and 1300 K above the Nishi et al. (2014) slab geotherm. An underlying base layer of 100–150 km thickness dominated by bm with 16 and 6 mol% of the $FeAlO_3$ and $Al_2O_3$ components, respectively, would remain within the bm stability field according to the result of Mohn and Trønnes (2018). This observation appears to be consistent with relatively thin high-viscosity bridgmanitic base layers of the LLSVPs, overlain by basaltic piles, largely in the pbm stability field (Fig. 23).

The collection and subsequent stabilisation of bridgmanitic material with elevated density, viscosity and bulk modulus into two separate

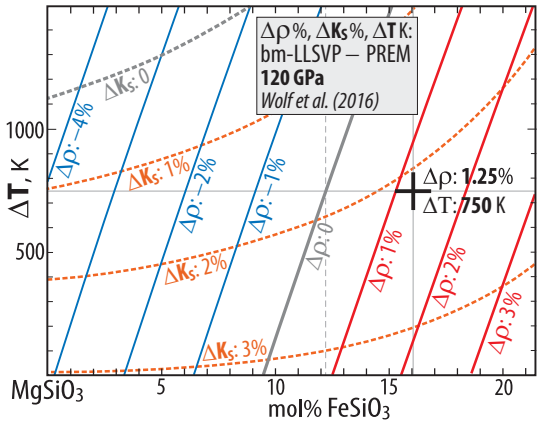


**Fig. 24.** Temperature difference between thermochemical piles dominated by bridgmanite (bm) and PREM (Dziewonski and Anderson, 1981) versus bm composition at 120 GPa with contours for the difference (%) in density and adiabatic bulk modulus. From Wolf et al. (2015). The large black cross, representing estimated density and temperature differences of about 1.25% and 750 K between the LLSVPs and the ambient D″ mantle, indicates a bm composition with 16 mol% combined $FeSiO_3$ and/or $FeAlO_3$. With a ΔT of 750 K at 120 GPa, the neutrally buoyant bm will have 12.2 mol% $FeSiO_3$ (grey stippled line).

antipodal LLSVP piles of 100–200 km thickness in equatorial positions might have been facilitated by a pre-existing degree-2 convection pattern, possibly active already during the BMO stage. Such a convective pattern with two antipodal upwelling columns and a wide longitudinal belt of sinking flow would sweep the dense material at the CMB into the root zones of the rising flow columns. Through the subsequent Earth evolution, the LLSVP piles might remain stable, not only by their elevated density and viscosity, but also by the degree-2 convection (e.g. Wolf et al., 2015).

## 5. Summary, discussion and conclusions

### 5.1. Accreted materials and core and mantle compositions

The accretion of the two outermost differentiated bodies, Vesta and Mars appears to have been terminated at the planetesimal and planetary embryo stages, respectively (e.g. Dauphas and Pourmand, 2011; Touboul et al., 2015). The interrupted accretion, in particular for Mars and possibly for Vesta, might be related to disc disruption caused by the inwards and outwards migration of Jupiter and Saturn at about 3–4 My after $t_0$ (Walsh et al., 2011). Therefore these two bodies received insignificant CC-group material from outside the proto-Jupiter orbit (about 5 AU), as indicated by their O-Cr-Ti-Ni-Ca-isotope systematics (e.g. Warren, 2011; Dauphas, 2017). Vesta and Mars may have grown from OC-ureilite mixtures and from OC material, respectively. Mercury, Venus and Earth grew mainly from EC-like material, which orbited closer to the Sun than corresponding EC and aubrite meteorite samples from the inner part of the main asteroid belt (e.g. Dauphas, 2017; Render et al., 2017). The EC- and aubrite-like material building the Earth had higher proportions of s-process Mo-isotopes than the corresponding samples in our meteorite collections. Earth, and possibly also Venus, received considerable amounts (up to 50%) of more oxidised non-EC material during the initial 60% accretion stage, probably also caused by time-limited disc disruption related to the early gas giant migration.

The bulk planetary oxygen fugacities of 4.6, 2.4, 2.2, 1.9, 1.4 and 1.1 log-units below IW for Mercury, Venus, Earth, Moon, Mars and Vesta, respectively, are most sensitive to the large ranges in the $FeO^{mantle}$ contents, which are 0.5, 6.3, 8.1, 12.4, 17.9 and 23.9 wt% in the same order. The Earth's bulk mantle composition is inferred to be

broadly pyrolitic, before limited modification of the lowermost mantle related to chemical interaction between the core and a basal magma ocean (BMO).

The MESSENGER results indicate equilibration of three strongly O-deficient liquids at the CMB pressure of about 5.7 GPa, providing very useful constraints on the Mercury core composition. The three liquids included a silicate magma ocean with about 10 wt% S and 0.5 wt% FeO, an FeS-dominated melt at the CMB and an Fe-dominated core alloy with 15 wt% Si and 1 wt% S. Recent experiments on O-deficient compositions (Morard and Katsura, 2010; Malavergne et al., 2014; Wood and Kiseeva, 2015) define the phase relations, and core and mantle compositions are further supported by density and size constraints for the core and mantle (Hauck et al., 2013; Knibbe and van Westrenen, 2018).

Strong gradients in velocity and density in the outermost 445 km of Earth's core might suggest an outer stagnant E′-layer with Si-depletion and O-enrichment relative to the convecting outer core (e.g. Brodholt and Badro, 2017). We infer a present core composition with 3.6 wt% Si and 3.0 wt% O, within the range of Badro et al. (2015), which is based on constraints from seismology and mineral physics. The E′-layer gradient is mainly ascribed to chemical core-BMO exchange. Our Venus core compositional estimate (6.2 wt% Si, 2.3 wt% O) is on a vector from Mercury to Earth and the distance along the vector is scaled to the $FeO^{mantle}$ compositions. The impact of a reduced Mercury- and aubrite-like Theia on the Earth would probably have incorporated some sulfide (not included in Table 2) with elevated concentrations of U and Th into the Earth's core (Wohlers and Wood, 2015, 2017; Wade and Wood, 2016; Greenwood et al., 2018), providing additional heat and geodynamo power. The cores within the more oxidised smaller bodies, Mars and Vesta, are S-rich (13–14 wt% S) due to the liquidus phase relations in the system Fe-FeS-FeO with the ternary eutectic close to the Fe-FeS join and a large immiscibility gap with a high-temperature solvus surface, covering most of the ternary field and the Fe-FeO join.

### 5.2. Magma ocean crystallisation, melt accumulation zones and dense cumulates

An immediate petrological discovery emerging from the Apollo program was the concept of planetary magma oceans (Smith et al., 1970; Wood et al., 1970). Thick anorthositic highland crust and the very distinct low-Ti, high-Ti and KREEP basalts, covering the nearside mare basins, originated by partial melting of the disrupted magma ocean cumulates dominated by olivine-orthopyroxene-, clinopyroxene-ilmenite and solidified late-stage residual melts, respectively. The mare basalt volcanism itself might have been triggered by the sinking of dense mantle cumulates, especially the clinopyroxene-ilmenite cumulates and possibly also KREEP-material, located at shallow mantle depths. The preferential segregation of magma ocean KREEP-type residual melt under the nearside Procellarium KREEP terrain would in itself promote the mare basalt magmatism in this region (Laneuville et al., 2013). The preservation of the primary anorthositic lunar highland crust, formed by plagioclase floatation, is unique in the Solar system, although Mercury might have had a corresponding magma ocean crust of graphite (Vander Kaaden and McCubbin, 2015).

Mars, Venus and Earth have neutral buoyancy levels for olivine versus peridotitic or komatiitic melt at about 11 GPa and melt accumulation zones at 14–15 GPa. Residual melts with elevated Fe/Mg-ratios would evolve in the melt accumulation zones, giving rise to high density cumulates that could sink to the CMB or into a partially molten BMO after thermal equilibration in the transition zone (e.g. Lee et al., 2010). Due to the strong partitioning of Fe and Mg to melt and solids, respectively, especially at pressures exceeding 80–100 GPa, Venus and Earth probably developed an upper and a basal magma ocean, crystallising from the bottom and from the top, respectively. After relatively extensive crystallisation, the upper magma ocean would be divided in two at the neutral buoyancy level at 11 GPa. Mars, Venus and Earth would barely have had primary crust from anorthositic floatation products. The depth range of plagioclase stability (1 GPa) is much greater in the Moon and Mars than in Venus and Earth. Without extensive core-BMO exchange, an advanced downwards BMO crystallisation with a $K_D^{bm/melt}$(Fe/Mg) of about 0.1 would have yielded residual melts and associated cumulates with extremely high Fe/Mg-ratios.

### 5.3. Core-mantle chemical exchange and modification of the lowermost mantle

The bulk planetary oxygen fugacities (Sections 2.2 and 5.1) indicate that the cores of the large planets, in particular, are far from equilibrium with their corresponding mantles. Core segregation with superheating of the early magma oceans and cores would have driven the equilibrium:

$$SiO_2^{sil} + 2Fe^{met} = 2FeO^{sil} + Si^{met}$$

towards the product side, increasing the $f_{O2}$ and silicate magma FeO content, coupled with considerable partitioning of Si into the cores (Fig. 5). Additional effects of high core segregation temperatures might have been the dissolution of minor amounts of other major oxides like MgO and $Al_2O_3$ into the cores. At 4000 K the solubilities of these oxides are lower than 0.6 wt%, but at 6000 K they might be as high as 2–3 wt% (Fig. 6). The exothermic exsolution of such components during core cooling will develop heat and buoyancy, adding to the geomagnetic driving force prior to the inner core crystallisation (O'Rourke and Stevenson, 2016). More important, however, is probably the exsolution of Si as $SiO_2$ (Hirose et al., 2017a), coupled with dissolution of FeO and $Fe_2O_3$ from the BMO melt and indirectly from the coexisting bm and fp. Silica crystallisation in response to decreasing Si-solubility in the core with decreasing temperature and increasing pressure is reflected by the mutual incompatibility of O and Si in Fe-dominated metal. Several experimental and thermodynamic modelling studies have shown that the core is strongly undersaturated with O, implying that FeO and $Fe_2O_3$ from bm, fp (e.g. Takafuji et al., 2005; Frost et al., 2010) and BMO melt would readily dissolve in the core metal unless the BMO was completely solidified such that the solid state diffusion rates, especially in bm, were the limiting factors (Holzapfel et al., 2005). Post-bridgmanite, which has a much higher diffusion rate (Amman et al., 2010) would probably not be present in direct contact with the core due to its low entropy and thermal stability. If bm and fp were in equilibrium with the core at 136 GPa and 4000 K, their Mg# would be about 99, which is much higher than Mg# of about 90 for bm and 83 for fp in the ambient peridotitic mantle.

Silica transfer from the core to the BMO as ascending and assimilating silica crystals, and possibly as $SiO_2$ from Si-enriched metal alloy plumes, combined with extraction of FeO and $Fe_2O_3$ from the BMO, dissolving into the core, would stabilise bm as the first liquidus phase and prolong the period of early bm crystallisation. Early bm-dominated cumulates would be refractory and viscous and might have partly survived the latest impact and heating events. The positive and μ($^{142}$Nd) and possibly also positive μ($^{182}$W) isotopic anomalies, recorded by Baffin Island and Ontong Java plume head basalt (Rizo et al., 2016; but see also Kruijer and Kleine, 2018), indicate that refractory mantle source heterogeneities might have survived as solids, probably near the lower mantle neutral buoyancy level, through the latest magma ocean event following the Earth-Theia collision. Subsequent convective aggregation of such viscous, refractory and neutrally buoyant materials in the solid lower mantle would tend to preserve it as large blobs or BEAMS (bm-enriched ancient mantle structures) through the Earth's history (Becker et al., 1999; Ballmer et al., 2017; Hirose et al., 2017b). The transfer of iron oxides from the BMO into the core and silica in the opposite direction would therefore change the bulk composition of the mantle slightly in the direction from peridotitic towards pyroxenitic or

bridgmanitic. Late-stage cumulates with relatively high bm/fp ratio and a bm with about 16 mol% of the $FeAlO_3$ component may form suitable 100–200 km thick base layers of the LLSVPs. Such LLSVP layers, remaining in the bm stability field, would have high viscosity and bulk modulus, and a density excess of 1–1.5% relative to the ambient D″ zone, assuming a temperature excess of 750 K for the LLSVPs at about 128 GPa. Whereas such LLSVP piles comprise only about 0.9% of the lower mantle volume, the refractory blobs or BEAMS might constitute 15–30 vol%.

### 5.4. Core-mantle redox relations and the transfer of O through the Earth

The O-undersaturation of the Earth's core and its disequilibrium with the mantle is related to cooling of the Earth from initial conditions of high temperature magma oceans in which the silicate-metal separation occurred. Whereas high MO temperatures would partition reduced Si into the core and FeO into the MO (Fig. 5), decreasing temperatures would lower the Si-solubility in the core and induce precipitation of silica (Figs. 21 – 22). If the molar ratios $SiO_2^{precipitated}/FeO^{dissolved}$ and $SiO_2^{precipitated}/FeO_{1.5}^{dissolved}$ exceed 0.5 and 0.67, respectively, the core would become even more O-undersaturated. The transfer of silica crystals from the outermost core to the BMO and Fe-oxide components in the opposite direction might have proceeded until the outermost E′-layer composition (0.4 wt% Si, 6.7 wt% O) reached the 4000 K contour on the silica liquidus surface, as indicated in Figs. 21–22. The core-mantle chemical exchange would also be greatly reduced after the complete solidification of the BMO. At the present, limited exchange might be focussed through the ultra-low velocity zones (Fig. 23), which by themselves might have originated as remnants of the BMO (e.g. Trønnes, 2010). ULVZs, comprising a convecting mixture of molten Fe-alloy in a solid matrix of $MgSiO_3$-dominated bm and cpv, may approach equilibrium with the top of the E′-layer and be continuously replenished by eutectic Fe-C melts (97.8 wt% Fe) from subducted basaltic ROC materials (Liu et al., 2016). The expected O, C and Si concentrations in the evolved and largely equilibrated molten Fe-alloy might be about 7, 2 and < 1 wt%, respectively. A continuous replenishment of Fe-dominated alloy from partially melting ROC, coupled with some leakage to the E′-layer, would imply a very slow core growth and associated oxidation of the D″ zone and bulk mantle.

With a completely solid mantle and no transfer of a molten Fe-alloy to the E′-layer, solid state mantle convection combined with limited diffusional exchange across the CMB would result in O-migration to the core and weak reduction of the deep mantle. Upper mantle peridotites without secondary alteration have $Fe^{3+}/Fe^{total}$ molar ratios of about 2% (Canil and O'Neill, 1996), whereas oxidised sediments, altered oceanic crust and depleted harzburgite in subducting slabs have much higher ferric iron proportions. With no silica transfer from the core to the mantle, the transfer of only FeO from the mantle to the core would therefore increase the iron oxidation state in the mantle. It is likely, however, that trivalent Fe oxide would have the same or even stronger tendency to diffuse through the CMB. The continuous ferrous iron oxide disproportionation to ferric and metallic iron associated with bm formation near the top of the lower mantle (e.g. Frost et al., 2004; Frost and McCammon, 2008), however, reduces the lower mantle considerably. The phase transition from ringwoodite and garnet to bridgmanite and ferropericlase in the uppermost lower mantle produces the essential $FeAlO_3$ component in bridgmanite and a coexisting Fe-metal phase, according to the reaction:

$$(2Fe_2SiO_4 + 2Mg_2SiO_4)^{rw} + Al_2O_3^{from\ ga} =$$
$$(2FeAlO_3 + 4MgSiO_3)^{bm} + FeO^{fp} + Fe^{metal\ alloy}$$

Even in the D″ zone, bm is likely to retain much of the $FeAlO_3$ component, although Prescher et al. (2014) recorded a slightly decreasing proportion at pressures exceeding 90 GPa in an experimental study on a peridotitic bulk composition. Their experiments indicate a decrease from 5 mol% $FeAlO_3$ at 60–80 GPa to 3 mol% at 100–130 GPa, combined with an increase from 5 to 6 mol% $FeSiO_3$ and from 0.5 to 1% $Al_2O_3$. The crystal chemical changes of Prescher et al. (2014) may be explained by the following two reactions:

$$2\ FeAlO_3^{bm} + Fe^{metal\ alloy} = Al_2O_3^{bm} + 3\ FeO^{fp}$$

$$FeO^{fp} + MgSiO_3^{bm} = MgO^{fp} + FeSiO_3^{bm}$$

At the BMO-stage, the O-undersaturation in the core could be efficiently reduced by bm-core exchange, via an interstitial silicate liquid, according to bm-core reactions involving ferric iron oxide dissolution in the core:

$$2\ FeAlO_3^{bm} = Al_2O_3^{bm\ or\ CF-structured\ phase} + Fe_2O_3^{to\ core}$$

$$2\ FeAlO_3^{bm} + SiO_2^{from\ core} + MgO^{fp} = Fe_2O_3^{to\ core} + (MgSiO_3 + Al_2O_3)^{bm}$$

The last reaction would transfer 2 O from the core and 3 O into the core. Although the two last reactions cannot explain the experimental results of Prescher et al. (2014), they are likely to have contributed to a reduced lowermost mantle with low proportion of the $FeAlO_3$ component in bridgmanite. As shown by Takafuji et al. (2005), Frost et al. (2010) and Otsuka and Karato (2012), there is no chemical tendency for metal alloy grains in the lowermost mantle to dissolve into the core. During the BMO period, however, dense Fe-alloy drops, formed by cyclic crystallisation and dissolution of bm and recharged with some O, might have descended into the core (Fig. 20). This process would presumably have oxidised both the core and the BMO, and Andrault et al. (2018) suggested that mantle convection, bringing the solidified BMO material to the upper mantle, might have oxidised the Earth's surface. The Fe-alloy drops would likely acquire a higher O-content than that of the outermost core before crossing the CMB, but their O-concentration must have been significantly lower than 22 and 30 wt%, corresponding to the oxides FeO and $Fe_2O_3$, respectively. The evidence for an outermost stagnant E′-layer enriched in O and depleted in Si relative to the convecting outer core (Brodholt and Badro, 2017) appears to support core-mantle chemical exchange during the BMO lifetime.

The Earth's crust and mantle have been oxidised from the atmosphere and hydrosphere throughout Earth history. $H_2O$ molecules degassed from volcanoes, even at the magma ocean stage, would be exposed to photo-dissociation in the upper atmosphere with loss of hydrogen to space. Volcanic degassing of $H_2O$ occurred on Venus also, but its position closer to the Sun might have prevented condensation to form glaciers, lakes and oceans. Venus might therefore have reached a nearly desiccated state, and the lack of a hydrosphere would prevent carbonate precipitation, resulting in the runaway $CO_2$ greenhouse effect (e.g. Wood, 1979). The gradually developing photosynthesis on Earth appears to have increased the $f_{O2}$ of the atmosphere both gradually and stepwise in the 2.4 to 0.54 Ga period (e.g. Lyon et al., 2014; Andersen et al., 2015), and oxidised surface materials are continuously injected into the convecting mantle by subduction. In spite of minor leakage of Fe-alloy melt from the ULVZs to the core, the net oxygen transport in the present-day Earth might therefore be from the surface, via the mantle, to the core.

### 5.5. Recent progress and future challenges

Our insights into the provenance and accretionary evolution of the terrestrial planets have developed rapidly within this decade. Hydrodynamic simulations and isotopic studies have shown that early growth and migration of the gas giants disrupted the protoplanetary disc and enabled oxidised material beyond the original Jupiter orbit to migrate inwards (e.g. Walsh et al., 2011; Morbidelli et al., 2012; Warren, 2011; Kruijer et al., 2017). This has provided useful constraints on accretionary time scales and material provenance. The long-held

suspicion that the Earth's geochemical fingerprint is EC-like (Javoy, 1995) is supported by recent isotope geochemistry, which also indicates that the most reduced material arrived late, partly by the Earth-Theia collision and during the late veneer stage (e.g. Dauphas, 2017; Render et al., 2017; Greenwood et al., 2018). An emerging view is that Theia itself was a Mercury- or aubrite-like body, 1–2 times the mass of Mars (e.g. Wade and Wood, 2016; Greenwood et al., 2018). The MESSENGER and Dawn missions provided extremely useful data on the innermost and reduced Mercury and the outermost, differentiated and oxidised planetesimal, Vesta. The Mercury data included surprises in terms of an extremely reduced planetary environment, whereas the Vesta data confirmed the results from geochemical investigations of the HED-meteorite collections and provided detailed surface and planetary structure information. Recent rover-based investigations of Mars have also been useful. The imminent planetary missions to Mercury (BepiColombo mission, ESA-JAXA mission) and the Psyche mission to a metallic asteroid (a NASA, Discovery Mission) will hopefully provide renewed momentum in the exploration of the terrestrial planets. Sample-collection missions to the Moon and Mars and renewed mapping of Venus would be important additional initiatives. Further developments of the analytical instruments and methods in isotope geochemistry, coupled with better and more accurately located planetary samples, will presumably expand our understanding of accretion and core segregation processes.

Experimental studies covering the pressure and temperature ranges of the Earth's mantle and most of the core have given valuable constraints on the subsolidus and melting phase relations of silicate and Fe-dominated metallic materials. Studies of Fe/Mg partitioning between bridgmanite and melt in peridotitic compositions (e.g. Tateno et al., 2014), coupled with density measurements (e.g. Petitgirard et al., 2015), support the notion of neutral buoyancy between the first bm crystals and the magma ocean melt at about 1700–1800 km depth and confirm the formation of a BMO, as suggested by Labrosse et al. (2007). Whereas the concept of an O-undersaturated core was established over a decade ago (e.g, Takafuji et al., 2005; Frost et al., 2010), the realisation that complementary Si-saturation could be alleviated by silica crystallisation is very recent (Hirose et al., 2017a). The chemical exchange involving dissolution of FeO and $Fe_2O_3$ components from the BMO into core metal, coupled with the buoyant rise of silica crystals from the core, dissolving in the BMO, can explain the bulk core composition, an outermost stagnant boundary layer (E′-layer), as well as refractory and viscous bm-dominated domains and thermochemical LLSVP-piles in the lower mantle. The initial study of the liquidus phase relations in the system Fe-Si-O at CMB pressure (Hirose et al., 2017a) has set the stage for further exploration of this system throughout the core pressure range. This is experimentally challenging and may be successfully complemented by ab initio atomistic simulations. Although the solubility of Mg and Al in Fe-dominated melts are lower than that of Si (e.g. Badro et al., 2016), high temperatures during core segregation in the largest terrestrial planets may incorporate at least 1–3 wt% of each of the elements at an expected protocore temperature of 5600 K (Laneuville et al., 2018) or higher. Further experimental and ab initio theory investigations within the system Fe-Mg-Al-O at pressures above the 35–74 GPa pressure range of Badro et al. (2016) are needed.

Mantle and core convection modelling is also an essential approach towards a fuller understanding of planetary dynamics. The Earth's mantle, including the D″ zone, encompasses large viscosity ranges that have barely been explored in convection models beyond a reconnaissance level. Global convection models have not fully explored the observed the degree-2 mantle and geoid structure observed for the Earth and other terrestrial planets, except Venus (Steinberger et al., 2010). Exploring different ranges and combinations of parameters, including gravity fields modulated by planetary rotation, to obtain such convection patterns might be a fruitful approach. The two most rapidly rotating terrestrial planets, Mars and Earth, have currently also the most pronounced degree-2 gravity structures, and a central question for the Earth is whether the degree-2 structure and convection pattern could have originated during the period of extra high rotation rates in the Hadean and Archean.

## References cited only in figure legends

Andersen, 1915
Brett and Bell, 1969
Chen et al., 2008
Garcia et al., 2012
Kiseeva and Wood, 2013
Kiseeva and Wood, 2015
Liebske et al., 2005
Naldrett, 1969
Presnall et al., 1978
Presnall et al., 1979
Urakawa et al., 1987
Walter et al., 2004
Wendlandt and Huebner, 1979

## Acknowledgements

The Centre for Earth Evolution and Dynamics, proposed and initiated by Trond Torsvik, is funded by CoE-grant 23272 from the Research Council of Norway. Trond's scientific insights and intuition, grand visions and persistence, as well as his generosity and sense of humour, have inspired us. We thank the present CEED director, Carmen Gaina, and the other guest editors for the opportunity to review Earth and planetary differentiation processes. Guest editor Bernhard Steinberger is thanked for his patience through a series of revisions. Two anonymous reviewers, and in particular Dan Frost, provided perceptive and extremely useful reviews. Helpful suggestions were also provided by John Hernlund and John Brodholt. The authors, however, take full responsibility for interpretations and speculations. Computational resources for atomistic simulations are provided by the Norwegian infrastructure for high-performance computing (NOTUR, grants NN9329K and NN2916K).

## Appendix A. Supplementary data

Supplementary data to this article can be found online at https://doi.org/10.1016/j.tecto.2018.10.021.

## References

Aitta, A., 2012. Venus' internal structure, temperature and core composition. Icarus 218, 967–974.
Amman, M.W., Brodholt, J.P., Wookey, J., Dobson, D.P., 2010. First-principles constraints on diffusion in lower-mantle minerals and a weak D″ layer. Nature 465, 462–465.
Andersen, O., 1915. The system anorthite-forsterite-silica. Am. J. Sci. 407–454 (Art. XXVII).
Andersen, M.B., Elliott, T., Freymuth, H., Sims, K.W.W., Niu, Y., Kelley, K.A., 2015. The terrestrial uranium isotope cycle. Nature 517, 356–359.
Andrault, D., Bolfan-Casanova, N., Nigro, G.L., Bouhif, M.A., Garbarino, G., Mezouar, M., 2011. Melting curve of the deep mantle applied to properties of early magma ocean and actual core-mantle boundary. Earth Planet. Sci. Lett. 304, 251–259.
Andrault, D., Petitgirard, S., Lo Nigro, G., Devidal, J.-L., Veronesi, G., Garbarino, G., Mezouar, M., 2012. Solid-liquid iron partitioning in Earth's deep mantle. Nature 487, 354–357.
Andrault, D., Pesce, G., Bouhifd, M.A., Bolfan-Casanova, N., Hénot, J.-M., Mezouar, M., 2014. Melting of subducted basalt at the core-mantle boundary. Science 344, 892–895.
Andrault, D., Muñoz, M., Pesce, G., Cerantola, V., Chumakov, A., Kantor, I., Pascarelli, S., Rüffer, R., Hennet, L., 2018. Large oxygen excess in the primitive mantle could be the source of the Great Oxygenation Event. Geochem. Perspect. Lett. 6, 5–10.
Antonangeli, D., Morard, G., Schmerr, N.C., Komabayashi, T., Krisch, M., Fiquet, G., Fei, Y., 2015. Toward a mineral physics reference model for the Moon's core. Proc. Natl. Acad. Sci. U. S. A. 112, 3916–3919.
Anzellini, S., Dewaele, A., Mezouar, M., Loubeyre, P., Morard, G., 2013. Melting of iron at Earth's inner core boundary based on fast X-ray diffraction. Science 340, 464–466.

Asahara, Y., Frost, D.J., Rubie, D.C., 2007. Partitioning between magnesiowu¨ stite and liquid iron at high pressures and temperatures: implications for the composition of the Earth's outer core. Earth Planet. Sci. Lett. 257, 435–449.
Badro, J., Cote, A.S., Brodholt, J.P., 2014. A seismologically consistent compositional model of Earth's core. Proc. Natl. Acad. Sci. U. S. A. 111, 7542–7545.
Badro, J., Brodholt, J.P., Piet, H., Siebert, J., Ryerson, F.J., 2015. Core formation and core composition from coupled geochemical and geophysical constraints. Proc. Natl. Acad. Sci. U. S. A. 112, 12310–12314.
Badro, J., Siebert, J., Nimmo, F., 2016. An early geodynamo driven by exsolution of mantle components from Earth's core. Nature 536, 326–328.
Ballmer, M.D., Schmerr, N.C., Nakagawa, T., Ritsema, J., 2015. Compositional mantle layering revealed by slab stagnation at ~1000-km depth. Sci. Adv. 1, e1500815.
Ballmer, M.D., Schumacher, L., Lekic, V., Thomas, C., Ito, G., 2016. Compositional layering within the large low shear-wave velocity provinces in the lower mantle. Geochem. Geophys. Geosyst. 17, 5056–5077.
Ballmer, M.C., Houser, C., Hernlund, J.W., Wentzcovitch, R.M., Hirose, K., 2017. Persistence of strong silica-enriched domains in the Earth's lower mantle. Nat. Geosci. 10, 236–240.
Barboni, M., Boehnke, P., Keller, B., Kohl, I.E., Schoene, B., Young, E.D., McKeegan, K.D., 2017. Early formation of the Moon 4.51 billion years ago. Sci. Adv. 3, e1602365.
Baron, M.A., Lord, O.T., Myhill, R., Thomson, A.R., Wang, W., Trønnes, R.G., Walter, M.J., 2017. Experimental constraints on melting temperatures in the MgO-$SiO_2$ system at lower mantle pressures. Earth Planet. Sci. Lett. 472, 186–196.
Becker, T.W., Boschi, L., 2002. A comparison of tomographic and geodynamic mantle models. Geochem. Geophys. Geosyst. 3, 1003. https://doi.org/10.1029/2001GC000168.
Becker, T.W., Kellogg, J.B., O'Connell, R.J., 1999. Thermal constraints on the survival of primitive blobs in the lower mantle. Earth Planet. Sci. Lett. 171, 351–365.
Bonnand, P., Halliday, A.N., 2018. Oxidized conditions in iron meteorite parent bodies. Nat. Geosci. 11, 401–404.
Brearley, A.J., Jones, R.H., 1998. Chondritic meteorites. Rev. Mineral. Geochem. 36, 3.1–3.398.
Brett, R., Bell, P.M., 1969. Melting relations in the Fe-rich portion of the system Fe-FeS at 30 kb pressure. Earth Planet. Sci. Lett. 6, 479–482.
Brodholt, J., Badro, J., 2017. Composition of the low seismic velocity E′ layer at the top of Earth's core. Geophys. Res. Lett. 44, 8303–8310.
Buffett, B.A., 2010. Chemical stratification at the top of Earth's core: constraints from observations of nutations. Earth Planet. Sci. Lett. 296, 367–372.
Buffett, B.A., Seagle, C.T., 2010. Stratification of the top of the core due to chemical interactions with the mantle. J. Geophys. Res. 115, B04407. https://doi.org/10.1029/2009JB006751.
Burke, K., Torsvik, T.H., 2004. Derivation of Large Igneous Provinces of the past 200 million years from long-term heterogeneities in the deep mantle. Earth Planet. Sci. Lett. 227, 531–538.
Canil, D., O'Neill, H.S.C., 1996. Distribution of ferric iron in some upper-mantle assemblages. J. Petrol. 3, 609–635.
Canup, R.M., 2012. Forming a Moon with an Earth-like composition via a giant impact. Science 338, 1052–1055.
Caracas, R., 2010. Spin and structural transitions in $AlFeO_3$ and $FeAlO_3$ perovskite and post-perovskite. Phys. Earth Planet. Inter. 182, 10–17.
Caro, G., Bourdon, B., Halliday, A.N., Quitte, G., 2008. Super-chondritic Sm/Nd ratios in Mars, the Earth and the Moon. Nature 452, 336–339.
Catalli, K., Shim, S.-H., Dera, P., Prakapenka, V.B., Zhao, J., Sturhahn, W., Chow, P., Xiao, Y., Cynn, H., Evans, W.J., 2011. Effects of the $Fe^{3+}$ spin transition on the properties of aluminous perovskite - new insights for lower-mantle seismic heterogeneities. Earth Planet. Sci. Lett. 310, 293–302.
Chabot, N.L., Drake, M.J., 2000. Crystallization of magmatic iron meteorites: the effects of phosphorus and liquid immiscibility. Meteorit. Planet. Sci. 35, 807–816.
Chen, B., Li, J., Hauck, S.A., 2008. Non-ideal liquidus curve in the Fe-S system and Mercury's snowing core. Geophys. Res. Lett. 35. https://doi.org/10.1029/2008GL033311.
Clesi, V., Bouhifd, M.A., Bolfan-Casanova, N., Manthilake, G., Schiavi, F., Raepsaet, C., Bureau, H., Khodja, H., Andrault, D., 2018. Low hydrogen contents in the cores of terrestrial planets. Sci. Adv. 4, e1701876.
Cobden, L., Thomas, C., Trampert, J., 2015. Chapter 13. Seismic detection of post-perovskite inside the Earth. In: Khan, A., Deschamps, F. (Eds.), The Earth's Heterogeneous Mantle. Springer, pp. 391–440.
Connelly, J.N., Bizarro, M., Krot, A.N., Nordlund, A., Wielandt, D., Ivanova, M.A., 2012. The absolute chronology and thermal processing of solids in the solar protoplanetary disk. Science 338, 651–655.
Corgne, A., Wood, B.J., 2005. Trace element partitioning and substitution mechanisms in calcium perovskites. Contrib. Mineral. Petrol. 149, 85–97.
Cuk, M., Stewart, S.T., 2012. Making the Moon from a fast-spinning Earth: a Giant impact followed by resonant despinning. Science 338, 1047–1052.
Dauphas, N., 2017. The isotopic nature of the Earth's accreting material through time. Nature 541, 521–524.
Dauphas, N., Pourmand, A., 2011. Hf-W-Th evidence for rapid growth of Mars and its status as a planetary embryo. Nature 473, 489–492.
Dauphas, N., Poitrasson, F., Burkhardt, C., Kobayashi, H., Kurosawa, K., 2015. Planetary and meteoritic Mg/Si and $\delta^{30}Si$ variations inherited from solar nebula chemistry. Earth Planet. Sci. Lett. 427, 236–248.
de Koker, N., Steinle-Neumann, G., Vlcek, V., 2012. Electrical resistivity and thermal conductivity of liquid Fe alloys at high P and T, and heat flux in Earth's core. Proc. Natl. Acad. Sci. U. S. A. 109, 4070–4073.
de Koker, N., Karki, B.B., Stixrude, L., 2013. Thermodynamics of the MgO–$SiO_2$ liquid system in Earth's lowermost mantle from first principles. Earth Planet. Sci. Lett. 361, 58–63.
De Sanctis, M.C., Ammannito, E., Capria, M.T., Tosi, F., Capaccioni, F., Zambon, F., Carraro, F., Fonte, S., Frigeri, A., Jaumann, R., Magni, G., Marchi, S., McCord, T.B., McFadden, L.A., McSween, H.Y., Mittlefehldt, D.W., Nathues, A., Palomba, E., Pieters, C.M., Raymond, C.A., Russell, C.T., Toplis, M.J., Turrini, D., 2012. Spectroscopic characterization of mineralogy and its diversity across Vesta. Science 336, 697–700.
DeMeo, F.E., Carry, B., 2014. Solar System evolution from compositional mapping of the asteroid belt. Nature 505, 629–634.
Deschamps, F., Cobden, L., Tackley, P.J., 2012. The primitivenatureoflargelowshear-wavevelocityprovinces. Earth Planet. Sci. Lett. 349–350, 198–202.
Dobson, D.P., Brodholt, J.P., 2005. Subducted banded iron formations as a source of ultralow-velocity zones at the core-mantle boundary. Nature 434, 371–374.
Dreibus, G., Wänke, H., 1985. Mars: a volatile-rich planet. Meteoritics 20, 367–381.
Driver, K.P., Cohen, R.E., Wu, Z., Militzer, B., Ríos, P.L., Towler, M.D., Needs, R.J., Wilkins, J.W., 2010. Quantum Monte Carlo computations of phase stability, equations of state, and elasticity of high-pressure silica. Proc. Natl. Acad. Sci. 107, 9519–9524.
Dziewonski, A.M., Anderson, D.L., 1981. Preliminary reference Earth model. Phys. Earth Planet. Inter. 25, 297–356.
Dziewonski, A., Lekic, V., Romanovich, B.A., 2010. Mantle anchor structure. An argument for bottom-up tectonics. Earth Planet. Sci. Lett. 299, 69–79.
Elkins-Tanton, L.D., 2012. Magma oceans in the inner Solar System. Annu. Rev. Earth Planet. Sci. 40, 113–139.
Fei, Y., Brosh, E., 2014. Experimental study and thermodynamic calculations of phase relations in the Fe–C system at high pressure. Earth Planet. Sci. Lett. 408, 155–162.
Fei, Y., Zhang, L., Corgne, A., Watson, H., Ricolleau, A., Meng, Y., Prakapenka, V., 2007. Spin transition and equation of state of (Mg,Fe)O solid solutions. Geophys. Res. Lett. 34, L17307.
Fiquet, G., Auzende, A.L., Siebert, J., Corgne, A., Bureau, H., Ozawa, H., Garbarino, G., 2010. Melting of peridotite to 140 GPa. Science 329, 1516–1518.
Fischer, R.A., Nakajima, Y., Campbell, A.J., Frost, D.J., Harries, D., Langenhorst, F., Miyajima, N., Pollok, K., Rubie, D.C., 2015. High pressure metal–silicate partitioning of Ni, Co, V, Cr, Si, and O. Geochim. Cosmochim. Acta 167, 177–194.
Fischer, R., Campbell, A., Ciesla, F., 2016. Sensitivities of Earth's core and mantle compositions to accretion and differentiation processes. Earth Planet. Sci. Lett. 458, 252–262.
French, S.W., Romanowicz, B., 2015. Broad plumes rooted at the base of the Earth's mantle beneath major hotspots. Nature 525, 95–99.
Frost, D.J., McCammon, C.A., 2008. The redox state of Earth's mantle. Annu. Rev. Earth Planet. Sci. 36, 389–420.
Frost, D.J., Liebske, C., Langenhorst, F., McCammon, C.A., Trønnes, R.G., Rubie, D.C., 2004. Experimental evidence for the existence of Fe-rich metal in the Earth's lower mantle. Nature 428, 409–412.
Frost, D.J., Mann, U., Asahara, Y., Rubie, D.C., 2008. The redox state of the mantle during and just after core formation. Phil. Trans. R. Soc. A 366, 4315–4337.
Frost, D.J., Asahara, Y., Rubie, D.C., Miyajima, N., Dubrovinsky, L.S., Holzapfel, C., Ohtani, E., Miyahara, M., Sakai, T., 2010. The partitioning of oxygen between the Earth's mantle and core. J. Geophys. Res. 115, B02202.
Fujino, K., Nishio-Hamane, D., Nagai, T., Seto, Y., Kunwayama, Y., Whitaker, M., Ohfuji, H., Shinmei, T., Irifune, T., 2014. Spin transition, substitution, and partitioning of iron in lower mantle minerals. Phys. Earth Planet. Inter. 228, 186–191.
Fujino, K., Nishio-Hamane, D., Seto, Y., Sata, N., Nagai, T., Shinmei, T., Irifune, T., Ishii, H., Hiraoka, N., Cai, T., Cai, Y.-Q., Tsuei, K.-D., 2012. Spin transition of ferric iron in Al-bearing Mg-perovskite up to 200 GPa and its implication for the lower mantle. Earth Planet. Sci. Lett. 317–318, 407–412.
Ganne, J., Feng, X., 2017. Primary magmas and mantle temperatures through time. Geochem. Geophys. Geosyst. 18, 872–888.
Garcia, R.F., Gagnepain-Beyneix, J., Chevrot, S., Lognonné, P., 2012. Erratum to "Very preliminary reference Moon model", by R.F. Garcia, J. Gagnepain-Beyneix, S. Chevrot, P. Lognonné [Phys. Earth Planet. Inter. 188 (2011) 96–113]. Phys. Earth Planet. Inter. 202–203, 89–91.
Garnero, E.J., McNamara, A.K., 2008. Structure and dynamics of Earth's lower mantle. Science 230, 626–628.
Garnero, E.J., Helmberger, D.V., Grand, S.P., 1993. Constraining outermost core velocity with SmKS waves. Geophys. Res. Lett. 20, 2463–2466.
Garnero, E.J., McNamara, A.K., Shim, S.-H., 2016. Continent-sized anomalous zones with low seismic velocity at the base of Earth's mantle. Nat. Geosci. 9, 481–489.
Ghosh, D.B., Karki, B.B., 2016. Solid-liquid density and spin crossovers in (Mg, Fe)O system at deep mantle conditions. Sci. Rep. 6, 37269.
Ghosh, D.B., Karki, B.B., Stixrude, L., 2014. First-principles molecular dynamics simulations of $MgSiO_3$ glass: Structure, density, and elasticity at high pressure. Am. Mineral. 99, 1304–1314.
Girard, J., Amulele, G., Farla, R., Mohiuddin, A., Karato, S., 2016. Shear deformation of bridgmanite and magnesiowüstite aggregates at lower mantle conditions. Science 351, 144–147.
Goryaeva, A.M., Carrez, P., Cordier, P., 2016. Low viscosity and high attenuation in $MgSiO_3$ post-perovskite inferred from atomic-scale calculations. Sci. Rep. 6, 34771.

Greenwood, R.C., Barrat, J.-A., Miller, M.F., Anand, M., Dauphas, N., Franchi, I.A., Sillard, P., Starkey, N.A., 2018. Oxygen isotopic evidence for accretion of Earth's water before a high-energy Moon-forming giant impact. Sci. Adv. 4, eaao5928.
Grocholski, B., Shim, S.H., Prakapenka, V.B., 2013. Stability, metastability, and elastic properties of a dense silica polymorph, seifertite. J. Geophys. Res. 118, 4745–4757.
Grove, T.L., Krawczynski, M.J., 2009. Lunar mare volcanism: where did the magmas come from? Elements 5, 29–34.
Gubbins, D., Davies, C.J., 2013. The stratified layer at the core–mantle boundary caused by barodiffusion of oxygen, sulfur and silicon. Phys. Earth Planet. Int. 215, 21–28.
Gubbins, D., Alfe, D., Davies, C., Pozzo, M., 2015. On core convection and the geodynamo: Effects of high electrical and thermal conductivity. Phys. Earth Planet. Int. 247, 56–64.
Haack, H., McCoy, T.J., 2003. Iron and stony-iron meteorites. In: Davis, Andrew M., Holland, Heinrich D., Turekian, Karl K. (Eds.), Treatise on Geochemistry. vol. 1. Elsevier, pp. 711 (0-08-043751-6. 325-345).
Hauck, S.A., Margot, J.-L., Solomon, S.C., Phillips, R.J., Johnson, C.L., Lemoine, F.G., Mazarico, E., McCoy, T.J., Padovan, S., Peale, S.J., Perry, M.E., Smith, D.E., Zuber, M.T., 2013. The curious case of Mercury's internal structure. J. Geophys. Res. Planets 118 (6), 1204–1220.
Helffrich, G., Kaneshima, S., 2010. Outer-core compositional stratification from observed core wave speed profiles. Nature 468, 807–810.
Hernlund, J., 2016. Chemistry of core-mantle boundary. In: Terasaki, H., Fischer, R. (Eds.), Deep Earth: Physics and Chemistry of the Lower Mantle and Core. Am. Geophys. Union, pp. 201–208.
Hernlund, J.W., Geissman, M., 2016. Chemical reaction between a basally molten mantle and core. In: Abstract #133, 15th Symp., Study of the Earth's Deep Interior (SEDI), pp. 190.
Hernlund, J.W., Houser, C., 2008. On the statistical distribution of seismic velocities in Earth's deep mantle. Earth Planet. Sci. Lett. 265, 423–437.
Hernlund, J.W., Jellinek, M., 2010. Dynamics and structure of a stirred partially molten ultralow-velocity zone. Earth Planet. Sci. Lett. 296, 1–8.
Hernlund, J.W., McNamara, A.K., 2015. The core-mantle boundary region. In: Treatise on Geophys. 7.11. pp. 461–519.
Hernlund, J.W., Thomas, C., Tackley, P.J., 2005. A doubling of the post-perovskite phase boundary and structure of the Earth's lowermost mantle. Nature 434, 882–886.
Herzberg, C.T., 1984. Chemical stratification of the silicate Earth. Earth Planet. Sci. Lett. 67, 249–260.
Herzberg, C.T., O'Hara, M.J., 2002. Plume-associated ultramafic magmas of Phanerozoic Age. J. Petrol. 43, 1857–1883.
Herzberg, C.T., Zhang, J., 1996. Melting experiments on anhydrous KLB-1: compositions of magmas in the upper mantle and transition zone. J. Geophys. Res. 101, 8271–8295.
Herzberg, C., Condie, C., Korenaga, J., 2010. Thermal history of the Earth and its petrological expression. Earth Planet. Sci. Lett. 292, 79–88.
Hewins, R.H., Herzberg, C.T., 1996. Nebular turbulence, chondrule formation, and the composition of the Earth. Earth Planet. Sci. Lett. 144, 1–7.
Heyn, B.H., Conrad, C.P., Trønnes, R.G., 2018. Stabilizing effect of compositional viscosity contrasts on thermochemical piles. Geophys. Res. Lett. 45, 7523–7532.
Hirose, K., Fei, Y., 2002. Subsolidus and melting phase relations of basaltic composition in the uppermost.lower mantle. Geochim. Cosmochim. Acta 66, 2099–2108.
Hirose, K., Takafuji, N., Sata, N., Ohishi, Y., 2005. Phase transition and density of subducted MORB crust in the lower mantle. Earth Planet. Sci. Lett. 237, 239–251.
Hirose, K., Labrosse, S., Hernlund, J., 2013. Composition and state of the core. Annu. Rev. Earth Planet. Sci. 41, 657–691.
Hirose, K., Morard, G., Sinmyo, R., Umemoto, K., Hernlund, J., Helffrich, G., Labrosse, S., 2017a. Crystallization of silicon dioxide and compositional evolution of the Earth's core. Nature 543, 99–102.
Hirose, K., Sinmyo, R., Hernlund, J., 2017b. Perovskite in Earth's deep interior. Science 358, 734–738.
Holmström, E., Stixrude, L., 2015. Spin crossover in ferropericlase from first-principles molecular dynamics. Phys. Rev. Lett. 114, 117202.
Holzapfel, C., Rubie, D.C., Frost, D.J., Langenhorst, F., 2005. Fe-Mg interdiffusion in (Mg,Fe)$SiO_3$ perovskite and lower mantle reequilibration. Science 309, 1707–1710.
Huguet, L., Van Orman, J.A., Hauck II, S.A., Willard, M.A., 2018. Earth's inner core nucleation paradox. Earth Planet. Sci. Lett. 487, 9–20.
Iizuka-Oko, R., Yagi, T., Gotou, H., Okuchi, T., Hattori, T., Sano-Furukawa, A., 2017. Hydrogenation of iron in the early stage of Earth's evolution. Nat. Commun. 8, 14096.
Irifune, T., Tsuchiya, T., 2015. Phase transitions and mineralogy of the lower mantle. In: Schubert, G. (Ed.), Treatise on Geophysics, 2nd edition. vol. 2. Elsevier, pp. 33–60 (Chapter 2.03).
Irving, J.C.E., Cottaar, S., Lekic, V., 2018. Seismically determined elastic parameters for Earth's outer core. Sci. Adv. 4, eaar2538.
Ishii, M., Tromp, J., 1999. Normal-mode and free-air gravity constraints on lateral variations in velocity and density of Earth's mantle. Science 285, 1231–1236.
Ito, E., Kubo, A., Katsura, T., Walter, M.J., 2004. Melting experiments of mantle materials under lower mantle conditions with implications for magma ocean differentiation. Phys. Earth Planet. Inter. 143–144, 397–406.
Jacobsen, S.A., Morbidelli, A., Raymond, S.N., O'Brien, D.P., Walsh, K.J., Rubie, D.C., 2014. Highly siderophile elements in Earth's mantle as a clock for the Moon-forming impact. Nature 508, 84–87.
Jaupart, C., Labrosse, S., Lucazeau, F., Mareschal, J.-C., 2015. Temperatures, heat and energy in the mantle of the Earth. In: Treat. Geophys. 7.06. pp. 223–270.
Javoy, M., 1995. The integral enstatite chondrite model of the Earth. Geophys. Res. Lett. 22, 2219–2222.
Javoy, M., Kaminski, E., Guyot, F., Andrault, D., Sanloup, C., Moreira, M., Labrosse, S., Jambon, A., Agrinier, P., Davaille, A., Jaupart, C., 2010. The chemical composition of the Earth: enstatite chondrite models. Earth Planet. Sci. Lett. 293, 259–268.
Jones, J.H., Drake, M.J., 1983. Experimental investigations of trace element fractionation in iron meteorites, II: the influence of sulfur. Geochim. Cosmochim. Acta 47, 1199–1209.
Jung, D.Y., Schmidt, M.W, 2011. Solid solution behavior of $CaSiO_3$ and $MgSiO_3$ perovskites. Phys. Chem. Mineral. 38, 311–319.
Kanda, R.V.S., Stevenson, D.J., 2006. Suction mechanism for iron entrainment into the lower mantle. Geophys. Res. Lett. 33, L02310.
Kaneshima, S., 2018. Array analyses of SmKS waves and the stratification of Earth's outermost core. Phys. Earth Planet. Inter. 276, 234–246.
Kaneshima, S., Helffrich, G., 2013. Vp structure of the outermost core derived from analyzing large-scale array data of SmKS waves. Geophys. J. Int. 193, 1537–1555.
Kaneshima, S., Matsuzawa, T., 2015. Stratification of earth's outermost core inferred from SmKS array data. Prog. Earth Planet. Sci. 2 (59–15).
Kato, T., Ringwood, A.E., 1989. Melting relationships in the system Fe-FeO at high pressures: implications for the composition and formation of the earth's core. Phys. Chem. Miner. 16, 524–538.
Khan, A., Connolly, J.A.D., 2008. Constraining the composition and thermal state of Mars from inversion of geophysical data. J. Geophys. Res. 113, E07003. https://doi.org/10.1029/2007JE002996.
Khan, A., Liebske, C., Rozel, A., Rivoldini, A., Nimmo, F., Connolly, J.A.D., Plesa, A.-C., Giardini, D., 2018. A geophysical perspective on the bulk composition of Mars. J. Geophys. Res. 123, 575–611.
Kiseeva, K.S., Wood, B.J., 2013. A simple model for chalcophile element partitioning between sulphide and silicate liquids with geochemical applications. Earth Planet. Sci. Lett. 383, 68–81.
Kiseeva, K.S., Wood, B.J., 2015. The effects of composition and temperature on chalcophile and lithophile element partitioning into magmatic sulphides. Earth Planet. Sci. Lett. 424, 280–294.
Knibbe, J.S., van Westrenen, W., 2018. The thermal evolution of Mercury's Fe-Si core. Earth Planet. Sci. Lett. 482, 147–159.
Knittle, E., Jeanloz, R., 1991. The Earth's core-mantle boundary: results of experiments at high pressures and temperatures. Science 251, 1438–1443.
Koelemeijer, P., Deuss, A., Ritsema, L., 2017. Density structure of Earth's lowermost mantle from Stoneley mode splitting observations. Nat. Commun. 8, 15241.
Koelemeijer, P., Schuberth, B.S.A., Davies, D.R., Deuss, A., Ritsema, L., 2018. Constraints on the presence of post-perovskite in Earth's lowermost mantle from tomographic-geodynamic model comparisons. Earth Planet. Sci. Lett. 494, 226–238.
Komabayashi, T., Hirose, K., Nagoya, Y., Sugimura, E., Ohishi, Y., 2010. High-temperature compression of ferropericlase and the effect of temperature on iron spin transition. Earth Planet. Sci. Lett. 297, 691–699.
Kruijer, T.S., Kleine, T., 2018. No $^{182}W$ excess in the Ontong Java Plateau source. Chem. Geol. 485, 24–31.
Kruijer, T.S., Touboul, M., Fischer-Gödde, M., Bermingham, K.R., Walker, R.J., Kleine, T., 2014. Protracted core formation and rapid accretion of protoplanets. Science 344, 1150–1154.
Kruijer, T.S., Burkhardt, C., Budde, G., Kleine, T., 2017. Age of Jupiter inferred from the distinct genetics and formation times of meteorites. Proc. Natl. Acad. Sci. 114, 6712–6716.
Kurnosov, A., Marquardt, H., Frost, D.J., Boffa Ballaran, T., Ziberna, L., 2017. Evidence for a $Fe^{3+}$-rich pyrolitic lower mantle from (Al,Fe)-bearing bridgmanite elasticity data. Nature 543, 543–546.
Kuwayama, Y., Hirose, K., Sata, N., Ohishi, Y., 2005. The pyrite-type high-pressure form of silica. Science 309, 923–925.
Labrosse, S., Hernlund, J.W., Coltice, N., 2007. A crystallizing dense magma ocean at the base of the Earth's mantle. Nature 450, 866–869.
Laneuville, M., Wieczorek, M.A., Breuer, D., Tosi, N., 2013. Asymmetric thermal evolution of the Moon. J. Geophys. Res. 118, 1435–1452.
Laneuville, M., Hernlund, J., Labrosse, S., Guttenberg, N., 2018. Crystallization of a compositionally stratified magma ocean. Phys. Earth Planet. Inter. 276, 86–92.
Lau, H.C.P., Mitrovica, L.X., Davis, J.L., Tromp, J., Yang, H.-Y., Al-Attar, D., 2017. Tidal tomography constrains Earth's deep-mantle buoyancy. Nature 551, 321–326.
Lay, T., 2015. Deep earth structure: lower mantle and D″. In: Schubert, Gerald (Ed.), Treatise on Geophysics, 2nd edition. vol. 1. Elsevier, Oxford, pp. 683–723 (Article 1.22).
Lay, T., Young, C.J., 1990. The stably-stratified outermost core revisited. Geophys. Res. Lett. 17, 2001–2004.
Lee, C.-T.A., Luffi, P., Hoink, T., Li, J., Dasgupta, R., Hernlund, J., 2010. Upside-down differentiation and generation of a 'primordial' lower mantle. Nature 463, 930–933.
Liebske, C., Frost, D.J., 2012. Melting phase relations in the MgO–$MgSiO_3$ system between 16 and 26 GPa: implications for melting in Earth's deep interior. Earth Planet. Sci. Lett. 345–348, 159–170.
Liebske, C., Corgne, A., Frost, D.J., Rubie, D.C., Wood, B.J., 2005. Compositional effects on element partitioning between Mg-perovskite and silicate melts. Contrib. Mineral. Petrol. 149, 113–128.
Lin, J.-F., Mao, Z., Yang, J., Liu, J., Xiao, Y., Chow, P., Okuchi, T., 2016. High-spin $Fe^{2+}$ and $Fe^{3+}$ in single-crystal aluminous bridgmanite in the lower mantle. Geophys. Res. Lett. 43. https://doi.org/10.1002/2016GL069836.

Liu, J., Li, J., Hrubiak, R., Smith, J.S., 2016. Origins of ultralow velocity zones through slab-derived metallic melt. Proc. Natl. Acad. Sci. U. S. A. 113, 5547–5551.
Liu, J., Hu, Q., Kim, D.J., Wu, Z., Wang, W., Xiao, Y., Chow, P., Meng, Y., Prakapenka, V.B., Mao, H.-K., Mao, W.L., 2017. Hydrogen-bearing iron peroxide and the origin of ultralow-velocity zones. Nature 551, 494–497.
Lodders, K., Fegley, B., 1997. An oxygen isotope model for the composition of Mars. Icarus 126, 373–394.
Lyon, T.W., Reinhard, C.T., Planavsky, N.J., 2014. The rise of oxygen in Earth's early ocean and atmosphere. Nature 506, 307–315.
Malavergne, V., Siebert, J., Guyot, F., Gautron, L., Combes, R., Hammouda, T., Borensztajn, S., Frost, D., Martinez, I., 2004. Si in the core? New high-pressure and high-temperature experimental data. Geochim. Cosmochim. Acta 68 (20), 4201–4211.
Malavergne, V., Toplis, M.J., Berthet, S., Jones, J., 2010. Highly reducing conditions during core formation on Mercury: Implications for internal structure and the origin of a magnetic field. Icarus 206, 199–209.
Malavergne, V., Cordier, P., Righter, K., Brunet, F., Zanda, B., Addad, A., Smith, T., Bureau, H., Surblé, S., Raepsaet, C., Charon, E., Hewins, R.H., 2014. How Mercury can be the most reduced terrestrial planet and still store iron in its mantle. Earth Planet. Sci. Lett. 394, 186–197.
Mao, W.L., Shen, G., Prakapenka, V.B., Meng, Y., Cambell, A.J., Heinz, D., Shu, J., Hemley, R.J., Mao, H.K., 2004. Ferromagnesian postperovskite silicates in the D″ layer of the Earth. Proc. Natl. Acad. Sci. U. S. A. 101, 15867–15869.
Mao, W.L., Mao, H.-K., Sturhahn, W., Zhao, J., Prakapenka, V.B., Meng, Y., Shu, J., Fei, Y., Memley, R.J., 2006. Iron-rich postperovskite and the origin of ultralow-velocity zones. Science 312, 564–565.
Mao, Z., Wang, F., Lin, J.-F., Fu, S., Yang, J., Wu, X., Okuchi, T., Tomioka, N., Prakapenka, V.T., Xiao, Y., Chow, P., 2017. Equation of state and hyperfine parameters of high-spin bridgmanite in the Earth's lower mantle by synchrotron X-ray diffraction and Mössbauer spectroscopy. Am. Mineral. 102, 357–368.
Marquardt, H., Miyagi, L., 2015. Slab stagnation in the shallow lower mantle linked to an increase in mantle viscosity. Nat. Geosci. 8, 311–314.
McCubbin, F.M., Riner, M.A., Vander Kaaden, K.E., Burkemper, L.K., 2012. Is Mercury a volatile-rich planet? Geophys. Res. Lett. 39, L09202.
McDonough, W.F., Sun, S.S., 1995. The composition of the Earth. Chem. Geol. 120, 23–253.
McNamara, A.K., Garnero, E.J., Rost, S., 2010. Tracking deep mantle reservoirs with ultra-low velocity zones. Earth Planet. Sci. Lett. 299, 1–9.
McSween, H.Y., Ammannito, E., Reddy, V., Prettyman, T.H., Beck, A.W., De Sanctis, M.C., Nathues, A., Le Corre, L., O'Brien, D.P., Yamashita, N., McCoy, T.J., Mittlefehldt, D.W., Toplis, M.J., Schenk, P., Palomba, E., Turrini, D., Tosi, F., Zambon, F., Longobardo, A., Capaccioni, F., Raymond, C.A., Russell, C.T., 2013. Composition of the Rheasilvia basin, a window into Vesta's interior. J. Geophys. Res. Planets 118, 335–346.
Mittlefehldt, D.W., McCoy, T.J., Goodrich, C.A., Kracher, A., 1998. Non-chondritic meteorites from asteroidal bodies. In: Rev. Mineral. Geochem. 36 (4.1-4.195).
Mittlefehldt, D.W., Clayton, R.N., Drake, M.J., Righter, K., 2008. Oxygen isotopic composition and chemical correlations in meteorites and the terrestrial planets. In: Oxygen in the Solar System, Rev. Mineral. Geochem. 68. pp. 399–428.
Mohn, C.E., Trønnes, R.G., 2016. Iron spin state and site distribution in $FeAlO_3$-bearing bridgmanite. Earth Planet. Sci. Lett. 440, 178–186.
Mohn, C.E., Trønnes, R.G., 2018. Partitioning of the $FeSiO_3$, $FeAlO_3$ and $Al_2O_3$ components between bridgmanite and post-bridgmanite. In: Goldschmidt Conf., Abstr. MR13A-2417.
Morard, G., Katsura, T., 2010. Pressure-temperature cartography of Fe–S–Si immiscible system. Geochim. Cosmochim. Acta 74, 3659–3667.
Morbidelli, A., Lunine, J.I., O'Brien, D.P., Raymond, S.N., Walsh, K.J., 2012. Building terrestrial planets. Annu. Rev. Earth Planet. Sci. 40, 251–275.
Mosenfelder, J.P., Asimow, P.D., Ahrens, T.J., 2007. Thermodynamic properties of $Mg_2SiO_4$ liquid at ultra-high pressures for shock measurements to 200 GPa on forsterite and wadsleyite. J. Geophys. Res. 112, B06208.
Mosenfelder, J.L., Asimow, P.D., Frost, D.J., Rubie, D.C., Ahrens, T.J., 2009. The $MgSiO_3$ system at high pressure: thermodynamic properties of perovskite, postperovskite, and melt from global inversion of shock and static compression data. J. Geophys. Res. 114, B01203.
Moulik, P., Ekström, G., 2016. The relationships between large-scale variations in shear velocity, density, and compressional velocity in the Earth's mantle. J. Geophys. Res. 121, 2737–2771.
Murakami, M., Bass, J.D., 2011. Evidence of denser $MgSiO_3$ glass above 133 gigapascal (GPa) and implications for remnants of ultradense silicate melt from a deep magma ocean. Proc. Natl. Acad. Sci. U. S. A. 108 (42), 17286–17289.
Murakami, M., Ohishi, Y., Hirao, N., Hirose, K., 2012. A perovskitic lower mantle inferred from high-pressure, high-temperature sound velocity data. Nature 485, 90–94.
Nakada, M., Karato, S.-i., 2012. Low viscosity of the bottom of the Earth's mantle inferred from the analysis of Chandler wobble and tidal deformation. Phys. Earth Planet. Inter. 192-193, 68–80.
Nakajima, Y., Frost, D.J., Rubie, D.C., 2012. Ferrous iron partitioning between magnesium silicate perovskite and ferropericlase and the composition of perovskite in the Earth's lower mantle. J. Geophys. Res. 117, B08201.
Naldrett, A.J., 1969. A portion of the system Fe–S–O between 900 and 1080 °C and its application to sulfide ore magmas. J. Petrol. 10, 171–201.
Nimmo, F., 2015. Thermal and compositional evolution of the core. In: Treat. Geophys. 9.08. pp. 201–219.
Nisbet, E.G., Walker, D., 1982. Komatiites and the structure of the Archean mantle. Earth Planet. Sci. Lett. 60, 105–113.
Nishi, M., Irifune, T., Tsuchiya, J., Tange, Y., Nishihara, Y., Fujino, K., Higo, Y., 2014. Stability of hydrous silicate at high pressures and water transport to the deep lower mantle. Nat. Geosci. 7, 224–227.
Nitter, L.R., Starr, R.D., Weider, S.Z., McCoy, T.J., Boynton, W.V., Ebel, D.S., Ernst, C.M., Evans, L.G., Goldsten, J.O., Hamara, D.K., Lawrence, D.J., McNutt, R.L., Schlemm, C.E., Solomon, S.C., Sprague, A.L., 2011. The major-element composition of Mercury's surface from MESSENGER X-ray spectrometry. Science 333, 1847–1850.
Nomura, R., Ozawa, H., Tateno, S., Hirose, K., Hernlund, J., Muto, S., Ishii, H., Hiraoka, N., 2011. Spin crossover and iron-rich silicate melt in the Earth's deep mantle. Nature 473, 199–202.
Nomura, R., Hirose, K., Uesugi, K., Ohishi, Y., Tsuchiyama, A., Miyake, A., Ueno, Y., 2014. Low core-mantle boundary temperature inferred from the solidus of pyrolite. Science 343, 522–525.
Nomura, R., Zhou, Y., Irifune, T., 2017. Melting phase relations in the $MgSiO_3$-$CaSiO_3$ system at 24 GPa. Prog, Earth Planet. Sci. 4, 34.
Ohnishi, S., Kuwayama, Y., Inoue, T., 2017. Melting relations in the MgO–$MgSiO_3$ system up to 70 GPa. Phys. Chem. Miner. 44, 445–453.
Ohta, K., Kuwayama, Y., Hirose, K., Shimizu, K., Ohishi, Y., 2016. Experimental determination of the electrical resistivity of iron at Earth's core conditions. Nature 534, 95–98.
Ohtani, E., Maeda, M., 2001. Density of basaltic melt at high pressure and stability of the melt at the base of the lower mantle. Earth Planet. Sci. Lett. 193, 69–75.
Ohtani, E., Ringwood, A.E., 1984. Composition of the core, I. Solubility of oxygen in molten iron at high temperatures. Earth Planet. Sci. Lett. 71 (1), 85–93.
Ohtani, E., Hirao, N., Kondo, T., Ito, M., Kikegawa, T., 2005. Iron-water reaction at high pressure and temperature, and hydrogen transport into the core. Phys. Chem. Miner. 32, 77–82.
Okuchi, T., 1997. Hydrogen partitioning into molten iron at high pressure: implications for Earth's core. Science 278, 1781–1784.
Olson, P., Deguen, R., Rudolph, M.L., Zhong, S., 2015. Core evolution driven by mantle global circulation. Phys. Earth Planet. Inter. 243, 44–55.
O'Neill, H.St.C., 1991a. The origin of the moon and the early history of the earth—a chemical model. Part 1: the moon. Geochim. Cosmochim. Acta 55, 1135–1157.
O'Neill, H.St.C., 1991b. The origin of the Moon and the early history of the Earth - A chemical model. Part 2: The Earth. Geochim. Cosmochim. Acta 55, 1159–1172.
O'Rourke, J.G., Stevenson, D.J., 2016. Powering Earth's dynamo with magnesium precipitation from the core. Nature 529, 387–389.
Otsuka, K., Karato, S., 2012. Deep penetration of molten iron into the mantle caused by a morphological instability. Nature 492, 243–246.
Ozawa, H., Hirose, K., Mitome, M., Bando, Y., Sata, N., Ohishi, Y., 2008. Chemical equilibrium between ferropericlase and molten iron to 134 GPa and implications for iron content at the bottom of the mantle. Geophys. Res. Lett. 35. https://doi.org/10.1029/2007GL032648.
Pahlevan, K., Stevenson, D.J., 2007. Equilibration in the aftermath of the lunar-forming giant impact. Earth Planet. Sci. Lett. 262, 438–449.
Palme, H., O'Neill, H.St.C., 2003. Cosmochemical estimates of mantle composition. In: Holland, H., Turekian, K.K. (Eds.), The Mantle and Core (Carlson RW), Treatise on Geochemistry. vol. 2. Elsevier-Pergamon, Oxford, pp. 1–38.
Peplowski, P.N., Evans, L.G., Hauck, S.A., McCoy, T.J., Boynton, W.V., Gillis-Davis, J.J., Ebel, D.S., Goldsten, J.O., Hamara, D.K., Lawrence, D.J., McNutt Jr., R.L., Nittler, L.R., Solomon, S.C., Rhodes, E.A., Sprague, A.L., Starr, R.D., Stockstill-Cahill, K.R., 2011. Radioactive elements on Mercury's surface from MESSENGER: implications for the planet's formation and evolution. Science 333, 1850–1852.
Petitgirard, S., Malfait, W.J., Sinmyo, R., Kupenko, I., Hennet, L., Harries, D., Dane, T., Burghammer, M., Rubie, D.C., 2015. Fate of $MgSiO_3$ melts at core–mantle boundary conditions. Proc. Natl. Acad. Sci. U. S. A. 112, 14186–14190.
Piet, H., Badro, J., Nabiei, F., Dennenwaldt, T., Shime, S.-H., Cantonic, M., Hébert, C., Gillet, P., 2016. Spin and valence dependence of iron partitioning in Earth's deep mantle. Proc. Natl. Acad. Sci. U. S. A. 113, 11127–11130.
Potapkin, V., McCammon, C., Glazyrin, K., Kantor, A., Kupenko, I., Prescher, C., Sinmyo, R., Smirnov, G.V., Chumakov, A.I., Rüffer, R., Dubrovinsky, L., 2013. Effect of iron oxidation state on the electrical conductivity of the Earths lower mantle. Nat. Commun. 1427, 4.
Pozzo, M., Davies, C., Gubbins, D., Alfè, D., 2012. Thermal and electrical conductivity of iron at Earth's core conditions. Nature 485, 355–358.
Pradhan, G.K., Fiquet, G., Siebert, J., Auzendea, A.-L., Morard, G., Antonangeli, D., Garbarino, G., 2015. Melting of MORB at core–mantle boundary. Earth Planet. Sci. Lett. 431, 247–255.
Prescher, C., Langenhorst, F., Dubrovinsky, L.S., Prakapenka, V.B., Miyajima, N., 2014. The effect of Fe spin crossovers on its partitioning behavior and oxidation state in a pyrolitic Earth's lower mantle system. Earth Planet. Sci. Lett. 399, 86–91.
Presnall, D.C., Dixon, S.A., Dixon, J.R., O'Donnell, T.H., Brenner, N.L., Schrock, R.L., Dycus, D.W., 1978. Liquidus phase relations on the join diopside-forsterite-anorthite from 1 atm to 20 kbar: their bearing on the generation and crystallization of basaltic magma. Contrib. Mineral. Petrol. 66, 203–220.
Presnall, D.C., Dixon, J.R., O'Donnell, T.H., Dixon, S.A., 1979. Generation of Mid-ocean Ridge Tholeiites. J. Petrol. 20, 3–35.
Render, J., Fischer-Gödde, M., Burkhardt, C., Kleine, T., 2017. The cosmic molybdenum-neodymium isotope correlation and the building material of the Earth. Geochem. Perspect. Lett. 3, 170–178.
Rizo, H., Walker, R.J., Carlson, R.W., Horan, M.F., Mukhopadhyay, S., Manthos, V.,

Francis, D., Jackson, M.G., 2016. Preservation of Earth-forming events in the tungsten isotopic composition of modern flood basalts. Science 352, 809–812.
Roeder, P.L., Emslie, R.F., 1970. Olivine-liquid equilibrium. Contrib. Mineral. Petrol. 29, 275–289.
Rohrbach, A., Schmidt, M.W., 2011. Redox freezing and melting in the Earth's deep mantle resulting from carbon-iron redox coupling. Nature 472, 209–214.
Romanowicz, B., 2003. Global mantle tomography: progress status in the last 10 years. Annu. Rev. Geophys. Space Phys. 31, 303–328.
Rubie, D.C., Gessmann, C.K., Frost, D.J., 2004. Partitioning of oxygen during core formation on the Earth and Mars. Nature 429, 58–61.
Rubie, D.C., Nimmo, F., Melosh, H.J., 2015a. Formation of the Earth's core. In: Treatise on Geophys. 9.03. pp. 43–79.
Rubie, D.C., Jacobson, S.A., Morbidelli, A., O'Brien, D.T., Young, E.D., de Vries, J., Nimmo, F., Palme, H., Frost, D.J., 2015b. Accretion and differentiation of the terrestrial planets with implications for the compositions of early-formed Solar System bodies and accretion of water. Icarus 248, 89–108.
Russell, C.T., Raymond, C.A., Coradini, A., McSween, H.Y., Zuber, M.T., Nathues, A., De Sanctis, M.C., Jaumann, R., Konopliv, A.S., Preusker, F., Asmar, S.W., Park, R.S., Gaskell, R., Keller, H.U., Mottola, S., Roatsch, T., Scully, J.E.C., Smith, D.E., Tricarico, P., Toplis, M.J., Christensen, U.R., Feldman, W.C., Lawrence, D.J., McCoy, T.J., Prettyman, T.H., Reedy, R.C., Sykes, M.E., Titus, T.N., 2012. Dawn at Vesta: testing the protoplanetary paradigm. Science 336, 684–686.
Sanloup, C., Jambon, A., Gillet, P., 1999. A simple chondritic model of Mars. Phys. Earth Planet. Inter. 112, 43–54.
Shahar, A., Schauble, E.A., Caracas, R., Gleason, A.E., Reagan, M.M., Xiao, Y., Shu, J., Mao, W., 2016. Pressure-dependent isotopic composition of iron alloys. Science 352, 580–582.
Shirey, S.B., Richardson, S.H., 2011. Start of the Wilson cycle at 3 Ga shown by diamonds from subcontinental mantle. Science 333, 434–436.
Sinmyo, R., Hirose, K., 2013. Iron partitioning in pyrolitic lower mantle. Phys. Chem. Miner. 40, 107–113.
Smith, J.V., Anderson, A.T., Newton, R.C., Olsen, E.J., Crewe, A.V., Isaacson, M.S., 1970. Petrologic history of the moon inferred from petrography, mineralogy and petrogenesis of Apollo 11 rocks. In: Levinson, A.A. (Ed.), Geochimica et Cosmochimica Acta Supplement, Volume 1. Proceedings of the Apollo 11 Lunar Science Conference Held 5–8 January, 1970 in Houston, TX. Mineraolgy and Petrology, vol. 1. Pergammon Press, New York, pp. 897.
Smith, D.E., Zuber, M.T., Phillips, R.J., Solomon, S.C., Hauck II, S.A., Lemoine, F.G., Mazarico, E., Neumann, G.A., Peale, S.J., Margot, J.-L., Johnson, C.L., Torrence, M.H., Perry, M.E., Rowlands, D.D., Goossens, S., Head, J.W., Taylor, A.H., 2012. Gravity field and internal structure of Mercury from MESSENGER. Science 336, 214–217.
Sreenivasan, B., Gubbins, D., 2008. Dynamos with weakly convecting outer layers: implications for core-boundary locking. Geophys. Astrophys. Fluid Dyn. 102, 395–407.
Steenstra, E.S., Lin, Y., Rai, N., Jansen, M., van Westrenen, W., 2017. Carbon as the dominant light element in the lunar core. Am. Mineral. 102, 92–97.
Steinberger, B., Torsvik, T.H., 2010. Toward an explanation for the present and past locations of the poles. Geochem. Geophys. Geosyst. https://doi.org/10.1029/2009GC002889.
Steinberger, B., Werner, S.C., Torsvik, T.H., 2010. Deep versus shallow origin of gravity anomalies, topography and volcanism on Earth, Venus and Mars. Icarus 207, 564–577.
Stewart, A.J., Schmidt, M.W., van Westrenen, W., Liebske, C., 2007. Mars: a new core-crystallization regime. Science 316, 1323–1325.
Stixrude, L., Karki, B., 2005. Structure and freezing of $MgSiO_3$ liquid in Earth's lower mantle. Science 310, 297–299.
Stixrude, L., de Koker, N., Sun, N., Mookherjee, M., Karki, B.B., 2009. Thermodynamics of silicate liquids in the deep Earth. Earth Planet. Sci. Lett. 278, 226–232.
Stolper, E., Walker, D., Hagar, B.H., Hays, J.F., 1981. Melt segregation from partially molten source regions: the importance of melt density and source region size. J. Geophys. Res. 86, 6261–6271.
Takafuji, N., Hirose, K., Mitome, M., Bando, Y., 2005. Solubilities of O and Si in liquid iron in equilibrium with $(Mg,Fe)SiO_3$ perovskite and the light elements in the core. Geophys. Res. Lett. 32. https://doi.org/10.1029/2005GL022773.
Tateno, S., Hirose, K., Sata, N., Ohishi, Y., 2009. Determination of post-perovskite phase transition boundary up to 4400 K and implications for thermal structure in D″ layer. Earth Planet. Sci. Lett. 277, 130–136.
Tateno, S., Hirose, K., Ohishi, Y., 2014. Melting experiments on peridotite to lowermost mantle conditions. J. Geophys. Res. 123, 4684–4694.
Tateno, S., Hirose, K., Sakata, S., Yonemitsi, K., Ozawa, H., Hirata, T., Hirao, N., Ohishi, Y., 2018. Melting phase relations and element partitioning in MORB to lowermost mantle conditions. J. Geophys. Res. 103. https://doi.org/10.1029/2018JB015790.
Toplis, M.J., Mizzon, H., Monnereau, M., Forni, O., McSween, H.Y., Mittlefehldt, D.W., McCoy, T.J., Prettyman, T.H., De Sanctis, M.C., Raymond, C.A., Russell, C.T., 2013. Chondritic models of 4 Vesta: Implications for geochemical and geophysical properties. Meteorit. Planet. Sci. 48. https://doi.org/10.1111/maps.12195.
Torsvik, T.H., Smethurst, M.A., Burke, K., Steinberger, B., 2006. Large Igneous Provinces generated from the margins of the large low velocity provinces in the deep mantle. Geophys. J. Int. 167, 1447–1460.
Torsvik, T.H., Burke, K., Steinberger, B., Webb, S.J., Ashwal, L.D., 2010. Diamonds sampled by plumes from the core–mantle boundary. Nature 466, 352–355.
Torsvik, T.H., van der Voo, R., Doubrovine, P.V., Burke, K., Steinberger, B., Ashwald, L.D., Trønnes, R.G., Webb, S.J., Bull, A.L., 2014. Deep mantle structure as a reference frame for movements in and on the Earth. Proc. Natl. Acad. Sci. U. S. A. 111, 8735–8740.
Torsvik, T.H., Steinberger, B., Ashwal, L.D., Doubrovine, P.V., Trønnes, R.G., 2016. Earth evolution and dynamics – a tribute to Kevin Bruke. Can. J. Earth Sci. 53, 1073–1087.
Touboul, M., Sprung, P., Aciego, S.M., Bourdon, B., Kleine, T., 2015. Hf–W chronology of the eucrite parent body. Geochim. Cosmochim. Acta 156, 106–121.
Trønnes, R.G., 2000. Melting relations and major element partitioning in an oxidized bulk Earth model composition at 15–26 GPa. Lithos 53, 233–245.
Trønnes, R.G., 2010. Structure, mineralogy and dynamics of the lowermost mantle. Mineral. Petrol. 99, 243–261.
Trønnes, R.G., Frost, D.J., 2002. Peridotite melting and mineral-melt partitioning of major and minor elements at 22–24.5 GPa. Earth Planet. Sci. Lett. 197, 117–131.
Trønnes, R.G., Canil, D., Wei, K., 1992. Element partitioning between silicate minerals and coexisting melts at pressures of 1–27 GPa, and implications for mantle evolution. Earth Planet. Sci. Lett. 111, 241–255.
Tschauner, O., Ma, C., Beckett, J.R., Prescher, C., Prakapenka, V.B., Rossman, G.R., 2014. Discovery of bridgmanite, the most abundant mineral in Earth, in a shocked meteorite. Science 346, 1100–1102.
Tsuno, K., Frost, D.J., Rubie, D.C., 2013. Simultaneous partitioning of silicon and oxygen into the Earth's core during early Earth differentiation. Geophys. Res. Lett. 40, 66–71.
Tuff, J., Wade, J., Wood, B.J., 2013. Volcanism on Mars controlled by early oxidation of the upper mantle. Nature 498, 342–345.
Ulff-Møller, F., 1998. Effects of liquid immiscibility on trace element fractionation in magmatic iron meteorites: a case study of group IIIAB. Meteorit. Planet. Sci. 33, 207–220.
Umemoto, K., Wentzcovitch, R.M., Wu, S., Ji, M., Wang, C.Z., Ho, K.-M., 2017. Phase transitions in $MgSiO_3$ post-perovskite in super-Earth mantles. 478, 40–45.
Urakawa, S., Kato, M., Kumazawa, M., 1987. Experimental study on the phase relations in the system Fe-Ni-O-S up to 15 GPa. In: High-pressure Research in Mineral Physics: A Volume in Honor of Syun-iti Akimoto.
Vander Kaaden, K.E., McCubbin, F.M., 2015. Exotic crust formation on Mercury: consequences of a shallow, FeO-poor mantle. J. Geophys. Res. Planets 120, 195–209.
Wade, J., Wood, B.J., 2005. Core formation and the oxidation state of the Earth. Earth Planet. Sci. Lett. 236, 78–95.
Wade, J., Wood, B.J., 2016. The oxidation state and mass of the Moon-forming impactor. Earth Planet. Sci. Lett. 442, 186–193.
Wahl, S.M., Militzer, B., 2015. High-temperature miscibility of iron and rock during terrestrial planet formation. Earth Planet. Sci. Lett. 410, 25–33.
Walsh, K.J., Morbidelli, A., Raymond, S.N., O'Brien, D.P., Mandell, A.M., 2011. A low mass for Mars from Jupiter's early gas-driven migration. Nature 475, 206–209.
Walter, M.J., 1998. Melting of garnet peridotite and the origin of komatiite and depleted lithosphere. J. Petrol. 39 (1), 29–60.
Walter, M.J., Cottrell, E., 2013. Assessing uncertainty in geochemical models for core formation in Earth. Earth Planet. Sci. Lett. 365, 165–176.
Walter, M.J., Trønnes, R.G., 2004. Early Earth differentiation. Earth Planet. Sci. Lett. 225, 253–269.
Walter, M.J., Nakamura, E., Trønnes, R.G., Frost, D., 2004. Experimental constraints on crystallization differentiation in a deep magma ocean. Geochim. Cosmochim. Acta 68, 4267–4284.
Walter, M.J., Kohn, S.C., Araujo, D., Bulanova, G.P., Smith, C.B., Gaillou, E., Wang, J., Steele, A., Shirey, S.B., 2011. Deep mantle cycling of oceanic crust; evidence from diamonds and their mineral inclusions. Science 334, 54–57.
Wang, K., Jacobsen, S.B., 2016. Potassium isotopic evidence for a high-energy giant impact origin of the Moon. Nature 538, 487–490.
Warren, P.H., 2011. Stable-isotopic anomalies and the accretionary assemblage of the Earth and Mars: a subordinate role for carbonaceous chondrites. Earth Planet. Sci. Lett. 311, 93–100.
Weber, R.C., Lin, P.-Y., Garnero, E.J., Williams, Q., Lognonné, P., 2011. Seismic detection of the lunar core. Science 331, 309–312.
Weisberg, M.K., Kimura, M., 2010. Petrology and Raman spectroscopy of high pressure phases in the Gujba CB chondrite and the shock history of the CB parent body. Meteorit. Planet. Sci. 45, 873–884.
Weisberg, M.K., Rinz, M., Clayton, R.N., Mayeda, T.K., Sugiura, N., Zashu, S., Eihara, M., 2001. A new metal-rich chondrite grouplet. Meteorit. Planet. Sci. 36, 401–418.
Wendlandt, R.F., Huebner, J.S., 1979. Melting relations of portions of the system Fe-S at high pressure and applications to the composition of the Earth's core. In: Abstr. Lunar Planet. Sci. X. pp. 1329–1331.
Wohlers, A., Wood, B.J., 2015. A Mercury-like component of early Earth yields uranium in the core and high mantle $^{142}Nd$. Nature 520, 337–340.
Wohlers, A., Wood, B.J., 2017. Uranium, thorium and REE partitioning into sulfide liquids: implications for reduced S-rich bodies. Geochim. Cosmochim. Acta 205, 226–244.
Wolf, A.S., Jackson, J.M., Dera, P., Prakapenka, V.B., 2015. The thermal equation of state of $(Mg,Fe)SiO_3$ bridgmanite (perovskite) and implications for lower mantle structures. J. Geophys. Res. 120, 7460–7489.
Wood, J.A., 1979. The Solar System. Prentice-Hall, Eaglewood Cliffs, NJ (196 pp.).
Wood, B.J., 1993. Carbon in the core. Earth Planet. Sci. Lett. 117, 593–607.
Wood, B.J., Kiseeva, E.S., 2015. Trace element partitioning into sulfide: how lithophile elements become chalcophile and vice versa. Am. Mineral. 100, 2371–2379.
Wood, J.A., Dickey Jr., J.S., Marvin, U.B., Powell, B.N., 1970. Lunar anorthosites and a geophysical model of the moon. In: Levinson, A.A. (Ed.), Geochimica et

Cosmochimica Acta Supplement, Volume 1. Proceedings of the Apollo 11 Lunar Science Conference Held 5–8 January, 1970 in Houston, TX. Mineraolgy and Petrology, vol. 1. Pergammon Press, New York, pp. 965.
Wood, B.J., Walter, M.J., Wade, J., 2006. Accretion of the Earth and segregation of its core. Nature 441, 825–833.
Wookey, J., Stackhouse, S., Kendall, J.M., Brodholt, J., Price, D., 2005. Efficacy of the post-perovskite phase as an explanation for the lowermost-mantle seismic properties. Nature 438, 1004–1007.
Wu, S., Umemoto, K., Ji, M., Wang, C.Z., Ho, K.M., Wentzcovitch, R.M., 2011. Identification of post-pyrite phase transitions in $SiO_2$ by a genetic algorithm. Phys. Rev. B 83, 184102.
Yoshino, T., Walter, M.J., Katsura, T., 2003. Core formation in planetesimals triggered by permeable flow. Nature 422, 154–157.
Yuan, K., Romanowicz, B., 2017. Seismic evidence for partial melting at the root of major hot spot plumes. Science 357, 393–397.
Zhang, J.Z., Herzberg, C., 1994. Melting experiments on anhydrous peridotite KLB-1 from 5 to 22.5 GPa. J. Geophys. Res. 99, 17729–17742.
Zolotov, M.Y., Sprague, A.L., Hauck, S.A., Nittler, L.R., Solomon, S.C., Weider, S.Z., 2013. The redox state, FeO content, and origin of sulfur-rich magmas on Mercury. J. Geophys. Res. Planets 118, 138–146.

# Supplementary information

Figures S1-S4.

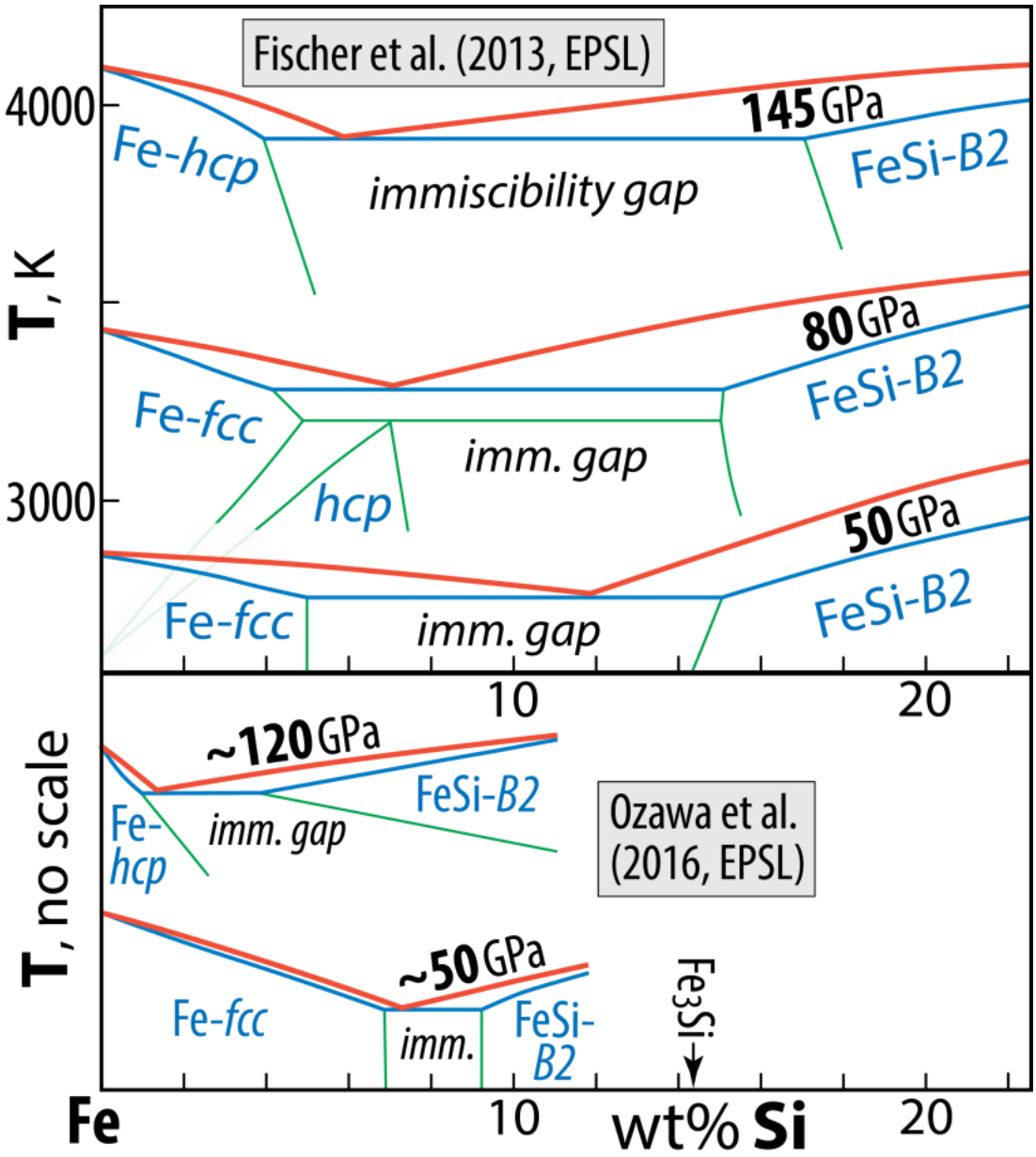


**Fig. S1**. Liquidus phase relations in the Fe-rich part of the system Fe-Si, 50-145 GPa (Fischer et al. 2013; Ozawa et al. 2016). Abbreviations: fcc, face-centred cubic structure; hcp, hexagonal close-packed strucrure; B2, CsCl-structure. This binary system is part of the ternary systems Fe-Si-S and Fe-Si-O, which are discussed based on Figs. 3, 19, 20 and 21.

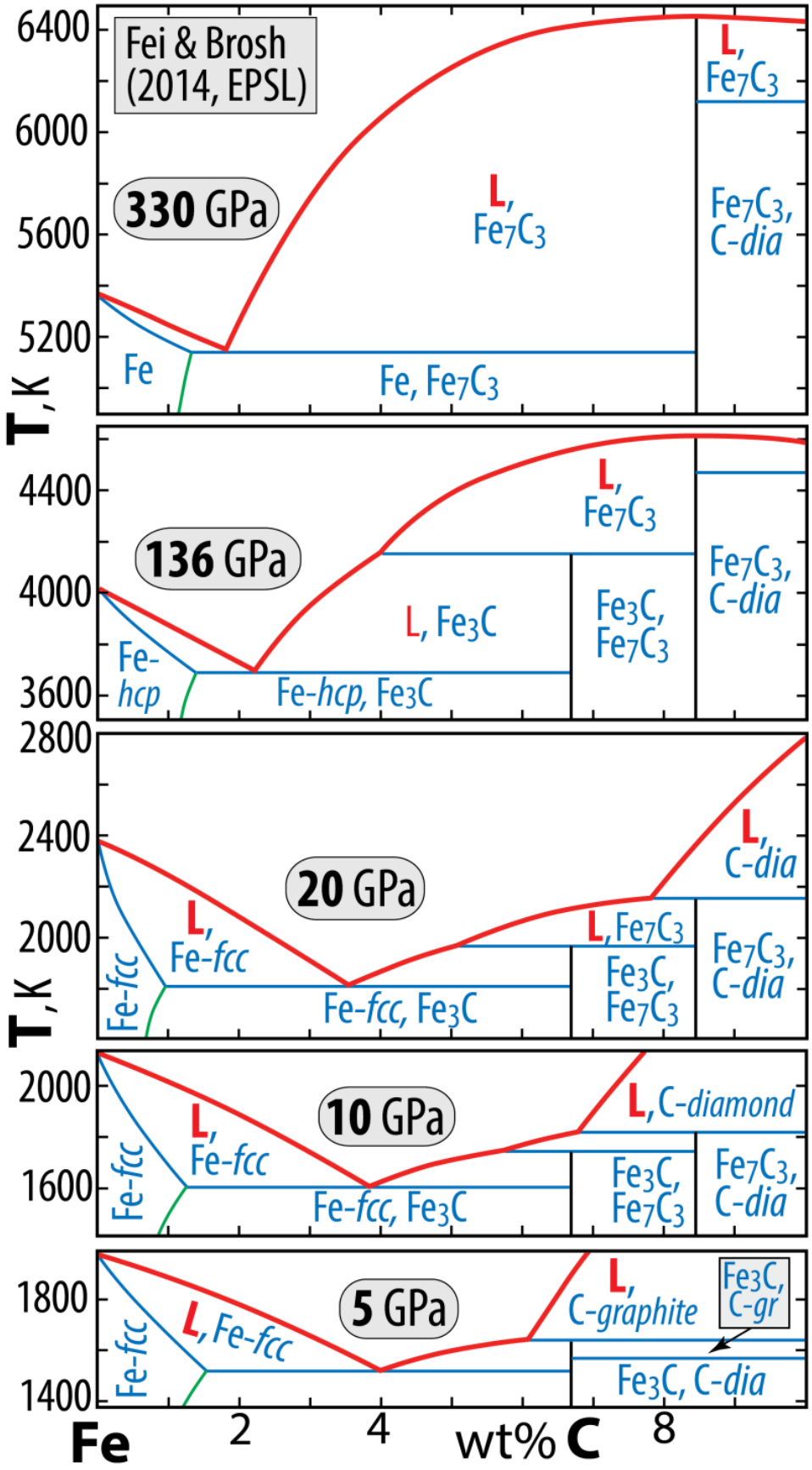


**Fig. S2**. Liquidus phase relations in the Fe-rich part of the system Fe-C, 5-330 GPa (Fei and Brosh, 2013). Abbreviations: fcc, face-centred cubic structure; hcp, hexagonal close-packed strucrure; gr, graphite; dia, diamond. The eutectics close to Fe at 136 GPa, 3690 K and 330 GPa, 5140 K indicate that the outer liquid core, as well as a potential Fe-C melt fraction of the ULVZs (Liu et al. 2016) might hold up to 2 wt% C. Solid $Fe_7C_3$ and $Fe_3C$ might conceivably be phases present in the inner core and the ULVZs, respectively.

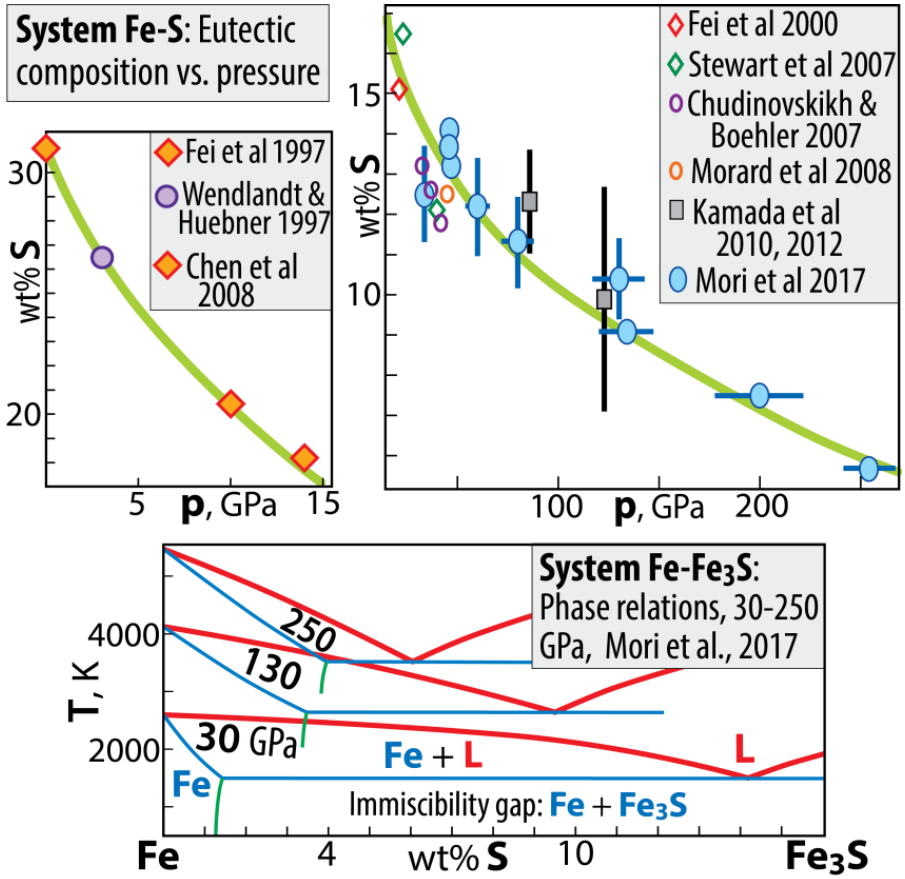


**Fig. S3**. Liquidus phase relations in the Fe-rich part of the system Fe-S, 1 bar to 250 GPa (based mostly on Mori et al., 2017, other references in legends). The two upper panels show the compositional shift of the Fe-rich eutectic as a function of pressure at 0-15 GPa (left) and 15-250 GPa. This binary system is part of the ternary system Fe-Si-S, which is discussed based on Fig. 3.

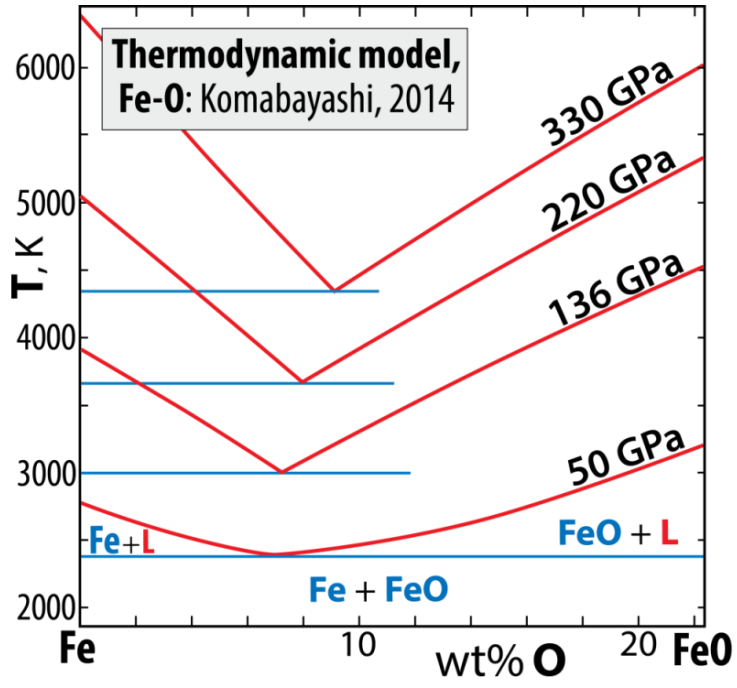


**Fig. S4**. Liquidus phase relations in the Fe-rich part of the system Fe-O, 50-330 GPa (Komabayashi, 2014). This binary system is part of the ternary system Fe-Si-O, which is discussed based on Figs. 19, 20 and 21.

# References for supplementary figures


Chen B, Li J, Hauck SA (2008) Non-ideal liquidus curve in the Fe-S system and Mercury's snowing core. Geophys Res Lett 35(7), 10.1029/2008GL033311

Chudinovskikh L, Boehler R (2007) Eutectic melting in the system Fe–S to 44 GPa. Earth Planet Sci Lett 257(1-2), 97-103.

Fei, Y., Brosh, E., 2014. Experimental study and thermodynamic calculations of phase relations in the Fe–C system at high pressure. Earth Planet. Sci. Lett. 408, 155-162.

Fei, Y., Bertka, C.M., Finger, L.W., 1997. High pressure iron sulfur compound, $Fe_3S_2$, and melting relations in the Fe–FeS system. Science 275, 1621–1623.

Fei Y, Li J, Bertka CM, Prewitt CT (2000) Structure type and bulk modulus of $Fe_3S$, a new iron-sulfur compound. Am. Mineral. 85(11-12), 1830-1833.

Fischer RA, Campbell AJ, Reaman DM, Miller NA, Heinz DL, Dera P, Prakapenka VB (2013) Phase relations in the Fe–FeSi system at high pressures and temperatures. Earth Planet. Sci. Lett. 373, 54-64.

Kamada S, Terasaki H, Ohtani E, Sakai T, Kikegawa T, Ohishi Y, Hirao N, Sata N, Kondo T (2010) Phase relationships of the Fe–FeS system in conditions up to the Earth's outer core. Earth Planet. Sci. Lett. 294(1–2), 94-100.

Kamada S, Ohtani E, Terasaki H, Sakai T, Miyahara M, Ohishi Y, Hirao N (2012) Melting relationships in the Fe–Fe3S system up to the outer core conditions. Earth Planet. Sci. Lett. 359-360, 26-33.

Komabayashi T (2014) Thermodynamics of melting relations in the system Fe-FeO at high pressure: Implications for oxygen in the Earth's core. J. Geophys. Res. Solid Earth 119(5), 10.1002/2014JB010980.

Liu, J., Li, J., Hrubiak, R., Smith, J.S., 2016. Origins of ultralow velocity zones through slab-derived metallic melt. Proc. Nat Acad. Sci. 113, 5547-5551.

Morard G, Andrault D, Guignot N, Sanloup C, Mezouar M, Petitgirard S, Fiquet G (2008) In situ determination of Fe–$Fe_3S$ phase diagram and liquid structural properties up to 65 GPa. Earth Planet. Sci. Lett. 272, 620–626.

Mori Y, Ozawa H, Hirose K, Sinmyo R, Tateno S, Morard G, Ohishi Y (2017) Melting experiments on Fe–Fe3S system to 254 GPa. Earth Planet. Sci. Lett., 464, 135-141.

Ozawa, H., Hirose, K., Yonemitsu, K., Ohishi, Y., 2016. High-pressure melting experiments on Fe–Si alloys and implications for silicon as a light element in the core. Earth Planet. Sci. Lett. 456, 47-54.

Stewart AJ, Schmidt MW, van Westrenen W, Liebske C (2007) Mars: A New Core-Crystallization Regime. Science 316, 1323-1325.

Wendlandt RF, Huebner JS (1979) Melting Relations of Portions of the System Fe-S at High Pressure and Applications to the Composition of the Earth's Core. Abstr. Lunar Planet. Sci. X, 1329-1331.